UNIVERSITÀ DEGLI STUDI DI BARI
ALDO MORO

DIPARTIMENTO INTERATENEO DI FISICA "M. MERLIN"

Dottorato di ricerca in FISICA – Ciclo XXX

Settore Scientifico Disciplinare FIS/01

Direct cross section measurement for the $^{18}O(p,\gamma)^{19}F$ reaction at LUNA

Dottorando:
Dott. Francesca Romana Pantaleo

Supervisore:
Ch.mo Dott. Roberto Perrino
Ch.mo Dott. Nicola Colonna

Coordinatore:
Ch.mo Prof. Gaetano Scamarcio

ESAME FINALE 2018

Contents

Abstract

The $^{18}O(p,\gamma)^{19}F$ reaction ($Q \simeq 7.99$ MeV) represents the bridge between the CNO cycle and other cycles involved in the production of heavier nuclei, which are active during shell H burning.
A $^{18}O/^{16}O$ isotopic ratio equal to $2.09^{+0.13}_{-0.12} \cdot 10^{-3}$ is present in matter within our solar system [1]. Investigations of oxygen isotopic ratios through pre-solar grains, gathered over the years from primitive meteorites and interplanetary dust particles, found a value $\leq 1.5 \cdot 10^{-3}$ [2], reflecting a substantial ^{18}O depletion compared to the solar system value.

It has been suggested that the low-mass asymptotic giant branch (AGB) stars are an ^{18}O depletion site [3] due to *cool bottom processing* (CBP) [2], in which the $^{18}O + p$ reaction occurs.
Within the CBP temperature regime (40 MK), the $^{18}O(p,\gamma)^{19}F$ reaction rate may be influenced by an unobserved low-energy resonance at $E_{res} = 95 \pm 3$ keV, that corresponds to the E_X=8084±3 keV [4] level in the ^{19}F nucleus. The 95 keV resonance strength is disputed by some authors [5] and [6]. An experimentally low upper limit of the 95 keV resonance strength [5] would have a negligible impact on the $^{18}O(p,\gamma)^{19}F$ reaction rate over the entire temperature range. On the contrary, a larger resonance strength estimated by [6] could be a dominant contribution to the reaction rate over the AGB stars temperature range.
A direct observation of the disputed resonance would thus be desirable, and measurements of the non-resonant cross section at lower energies can support the extrapolation of the non-resonant contribution towards lower energies of astrophysical interest.

Further measurements regarding the off-resonant and on-resonant higher energy range, were done in order to improve our knowledge of levels in the ^{19}F compound nucleus that are relevant to nuclear astrophysics and to complete available data known in literature [7], [8], [9].
This thesis was performed in the framework of the LUNA (Laboratory Underground for Nuclear Astrophysics) collaboration. The $^{18}O(p,\gamma)^{19}F$ reaction was investigated using the accelerator at the LUNA2 facility [10], which provides very accurate and reproducible ion beams of protons in the energy range of 50 keV $\leq E_p^{lab} \leq$ 400 keV with a maximum current (on-target) approx-

imately equal to 300 μA, and takes advantage of the underground location where the environmental background is suppressed of a factor 10^{-6} with respect to surface. The facility has two beamlines, one dedicated to solid target and the other one to gas target experiment. The solid target beamline has been used for studying the reaction of interest. The Ta_2O_5 targets were prepared by anodic oxidation [11] of thin tantalum disks with an isotopic enrichment 99% in ^{18}O.

The experimental campaign was split in two phases. The first phase is characterized by a high efficiency BGO summing crystal detector. During the second phase a high energy resolution HPGe detector was used, positioned at 55° with respect to the beam direction. Both approaches covered the common range of data taking (140-400 keV). The first phase extended the range of measurements to energies down to 89 keV, to probe the existence of the hypothetical low energy resonance using the high efficiency BGO summing crystal detector.
Five resonances were measured within 89-400 keV. For the first time a measurement was done in order to estimate the resonance strength for the low-energy resonance at $E_{res} = 95 \pm 3$ keV , and in addition measurements were done to increase the accuracy of knowledge on the 151 keV, 216 keV, 274 keV and 334 keV resonance strengths and to estimate the γ-ray branching ratios.

Both phases of the experiment are covered by this Ph.D. thesis.

In Chapter 1 the scientific background and interest of the present investigation will be presented. The astrophysical motivation for the study of the $^{18}O(p,\gamma)^{19}F$ reaction will be discussed with a look at the state of the art. Finally, the experimental campaign will be illustrated.

In Chapter 2 the LUNA2 facility, in particular the solid target beamline will be described. A detailed description of the experimental setup, including Ta_2O_5 solid target production, and the detecting system of BGO and HPGe setups will be described and discussed.

Chapter 3 will report about the experimental method, describing the energy and efficiency calibrations and the measurements.

Chapter 4 will present the data analysis and results. Here the resonance strengths estimation of both BGO and HPGe data is almost finalized. The determination of γ-ray branchings for on-resonance energy component is concluded for known (151 keV, 274 keV, 334 keV) and newly studied (216 keV) resonances. The results will be presented and discussed.

Conclusions are finally summarized.

Chapter 1

The ^{18}O(p, γ)^{19}F experiment: scientific background and motivation

1.1 Stellar evolution and nucleosynthesis

Stars emit nuclear energy since their origin. According to the current knowledge, the stellar evolution is based on the nuclear-burning processes ignited and moderated by the energy deriving from gravitational contraction. The birth and life of the stars are governed by specific thermonuclear reactions, determined by the temperature and the composition of the stellar interior.

The cold interstellar clouds of gas originating primordial stars predominantly consisted of molecular hydrogen (approximately 70% of the mass) and helium (constituting most of the remaining 30%) and possible trace amounts of heavier elements. This is not too surprising since these elements, along with trace amounts of lithium are believed to be formed during the creation of the universe itself [12].

The wide variety of elements present in the early universe is illustrated by the mass spectrum of Fig. 1.1. Gravitational potential energy of collapsing primordial cloud is transformed into thermal energy and into radiation. When the density increases, the opacity increases and the emitted radiation is retained in the cloud. Consequently, there is an increase of the temperature and the pressure that causes first a dissociation of hydrogen molecules into atoms, and then an ionization of hydrogen and helium atoms. The gas is completely ionized at a temperature of $10^5 K$. The electrons trap radiation efficiently [14] and, as a result, the temperature and the pressure continue to increase and the collapse of the central part of the cloud is stopped. A state of hydrostatic equilibrium characterizes the premain-sequence star, while still accreting matter from the outer parts of the cloud [14]. When temperatures

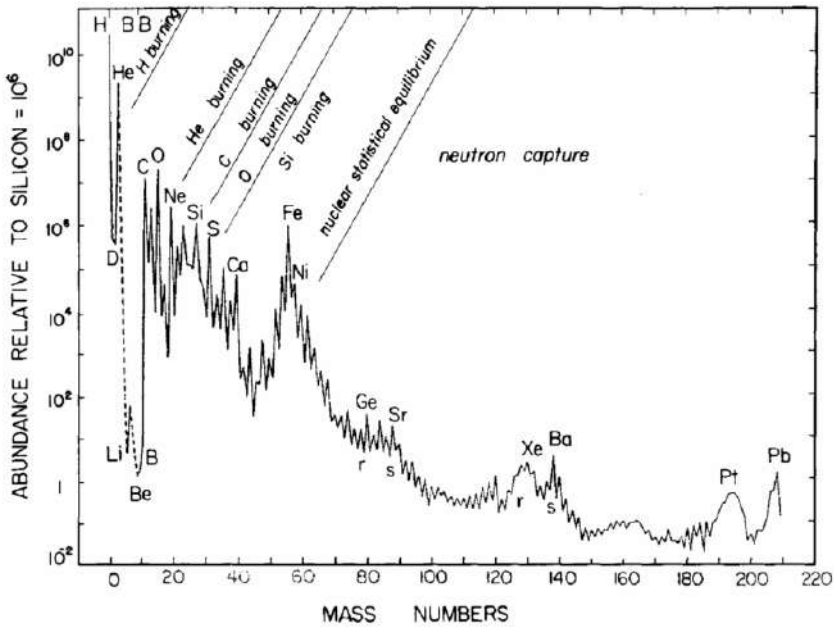

Figure 1.1: Relative abundances nuclides as a function of the mass number in the solar system [13].

of few millions Kelvin are reached, the source of energy is not only gravitational but the first nuclear reactions begin to occur. Subsequently the fusion of hydrogen to helium starts to occur at several millions Kelvin. The initial time for the occurrence of the nuclear reactions depends on the initial mass of the stars [14].

The radiation emitted per unit time or the *luminosity* during the stellar evolution, varies strongly from star to star. The same holds for the effective stellar surface temperature. The result of the correlation between these two quantities is a plot, called Hertzsprung-Russel (H-R) diagram in which the stars are located in several distinct groups (Fig. 1.2). The effective temperature and the luminosity can be expressed in terms of color and of absolute magnitude of the star, respectively, so the H-R diagram can be indistinctly called color-magnitude diagram.

The nuclear burning time fusing hydrogen to helium is greater when the stellar masses have a relative range of $M/M_{\odot} = 0.1 - 50$ and a relative luminosity range of $L/L_{\odot} = 10^{-2} - 10^{-6}$, denoting with $M_{\odot}$, $L_{\odot}$ the solar mass, and the solar luminosity, respectively. Consequently the majority (90%) of the stars populates the main sequence. Once a star leaves the main sequence, the evolution speeds up significantly [14].

The Sun, for example, is a main sequence star having mass equal to approximately $M_{\odot} = 1.99 \times 10^{30}$ kg, and a core temperature of 15 MK. In its

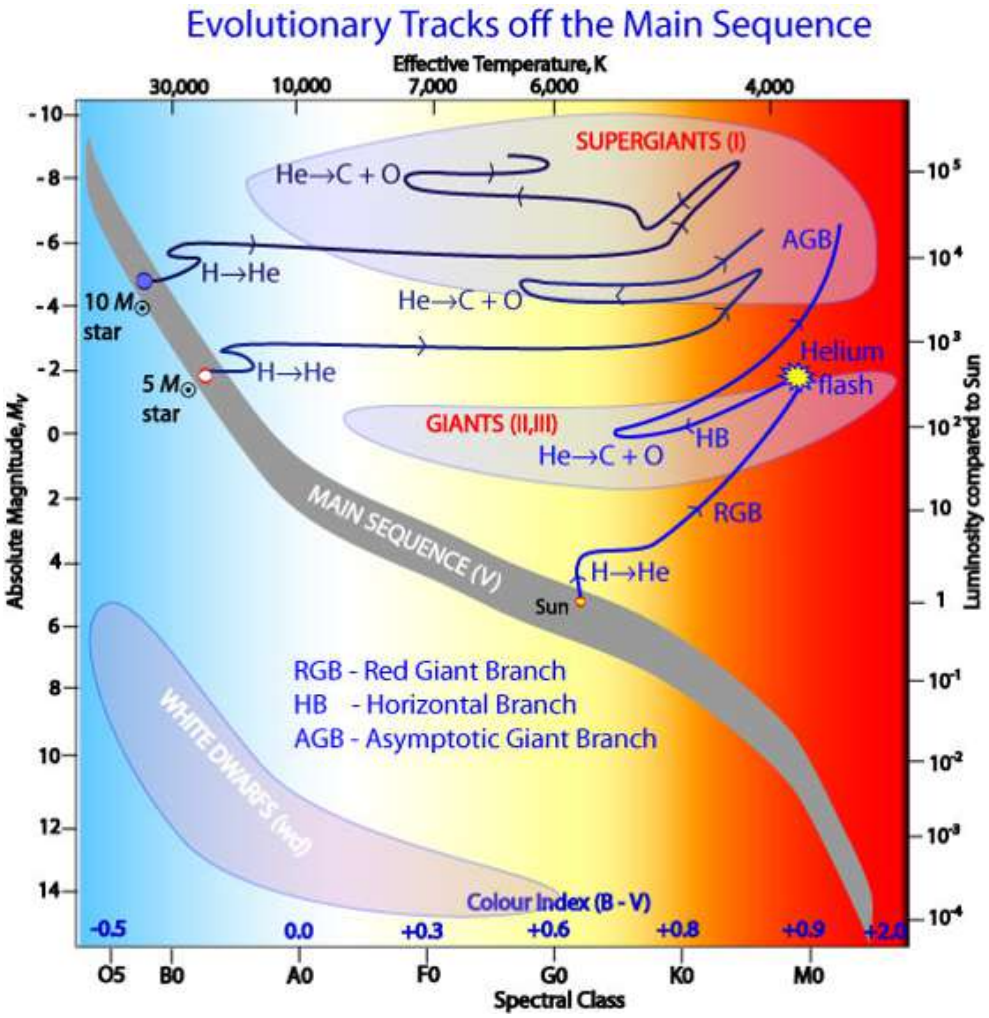

Figure 1.2: Observational Hertzsprung Russell diagram, showing absolute magnitude or luminosity compared to sun versus color temperature or spectral class [15].

core four protons fuse to helium and release a remarkable amount of energy (along with two positrons and two neutrinos):

$$4H \rightarrow^4 He + 2e^+ + 2\nu + 26.731\ MeV \tag{1.1}$$

It could remain on the main sequence for millions to billions of years.

Red giant and super-giant stars (luminosity classes I through III) occupy the region above the main sequence. They have $M = (0.5-5)M_\odot$, low surface temperatures and high luminosities [16]. These stars enter this evolutionary stage once they have exhausted the hydrogen fuel in their cores and have started to burn helium and other heavier elements. White dwarf stars are the final evolutionary stage of low to intermediate mass stars, and are found

in the bottom left of the H-R diagram. These stars have a theoretical upper limit to the mass M of around 1.4 $M_{\odot}$, that is named the Chandrasekhar Limit [14]. In addition, despite of being very hot they have low luminosities due to their small size.

The Asymptotic Giant Branch (AGB) is a characteristic region in the H-R diagram, that is populated by stars having a late life and masses smaller than 10 $M_{\odot}$. The AGB stars are characterized by an inert core of mostly carbon and oxygen surrounded by shells of helium and hydrogen. Helium and hydrogen burning occurs in these shells, and a complex interplay between the two shells is observed [17]. The intricate processes in AGB stars have an important role in the enrichment of heavier elements in the interstellar medium of this kind of stars.
The two major ways by which hydrogen is converted to helium in hydrostatic hydrogen burning are called the proton-proton chains and the CNO cycles. In both processes, the result is the one of Eq. (1.1). The simultaneous interaction of four protons in stellar environment is a very unlikely event, therefore the p-p chain is characterized by two body reactions and represents the most likely process of He production.

1.1.1 Proton-proton chain

The typical range of temperatures in which the core hydrogen burning occurs is $T = 8-55$ MK. The primary generation stars, having masses below $1.5 M_{\odot}$, are characterized by the fact that the hydrogen fusion proceeds via the p-p chain. The p-p chain consists of a series of proton captures on the lightest elements. This process happens through various reactions [14], Table 1.1. The Q_{eff} is the energy star available equal to the difference between the Q-value of the reaction and the average energy (0.52 MeV) taken away by neutrinos [18]. The Q-value is the amount of energy released by a nuclear reaction, for details see section 1.2.

1.1.2 CN cycle, bi-cycle CNO and tri-cycle CNO

After the p-p chain elements, the next ones which are light and abundant enough to provide fuel for a star are carbon, nitrogen, and oxygen, through well identified reaction cycles.
The CN cycle is a thermonuclear reaction chain able to convert hydrogen into helium contributing significantly to the stellar luminosity. It represents an important solar source for the massive stars of second and third generation during the main sequence as well as for the red giants. The second and third generation stars are a compound of hydrogen, helium and heavy elements, synthesized by the first generation stars. They have a chemical composition

Table 1.1: Three different p-p chains. The result is the conversion of 4 protons into an alpha particle plus some energy.

Chain I	Chain II	Chain III
$p(p, e^+\nu)$	$p(p, e^+\nu)d$	$p(p, e^+\nu)d$
$\downarrow$	$\downarrow$	$\downarrow$
$d(p, \gamma)^3He$	$d(p, \gamma)^3He$	$d(p, \gamma)^3He$
$\downarrow$	$\downarrow$	$\downarrow$
$^3He(^3He,^2 p)^4He$	$^3He(^4He, \gamma)^7Be$	$^3He(^4He, \gamma)^7Be$
	$\downarrow$	$\downarrow$
	$^7Be(e^-\nu)^7Li$	$^7Be(p, \gamma)^8B$
	$\downarrow$	$\downarrow$
	$^7Li(p, \alpha)^4He$	$^8B(e^+\nu)^8Be$
		$\downarrow$
		$^8Be^*(\alpha)^4He$
Q_{eff}= 26.20 MeV	25.66 MeV	19.17 MeV

richer than the first generation stars, including appreciable quantities of carbon and oxygen [14], [19].
The CN cycle consists of the following reactions chain:

$$^{12}C(p, \gamma)^{13}N(e^+, \nu)^{13}C(p, \gamma)^{14}N(p, \gamma)^{15}O(e^+, \nu)^{15}N(p, \alpha)^{12}C \tag{1.2}$$

Fig. 1.3 shows the sequence of reactions (1.2). The rate of the released energy is set by the slower reaction $^{14}N(p, \gamma)^{15}O$. During the CN cycle there is no combustion of N and C, which act simply as catalysts.
The reaction $^{15}N(p, \gamma)^{16}O$ could be in competition with $^{15}N(p, \alpha)^{12}C$, causing a lack of catalysts isotopes, and generating the chain of reactions:

$$^{16}O(p, \gamma)^{17}F(e^+, \nu)^{17}O(p, \alpha)^{14}N \tag{1.3}$$

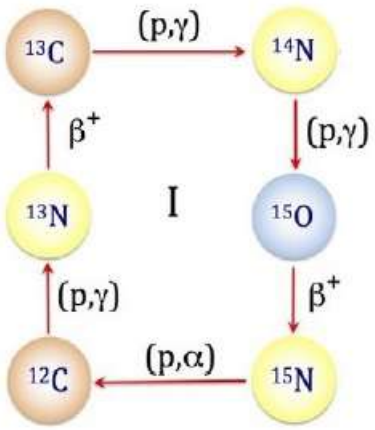

Figure 1.3: CN cycle reactions, characterized by proton captures, β^+ decays, catalyzed by ^{12}C,^{13}N,^{13}C,^{14}N,^{15}O,^{15}N [20].

which couples to the CN cycle and gives rise to the bicycle CNO (Fig. 1.4). Because of the higher repulsive force generated by the charge of the CNO

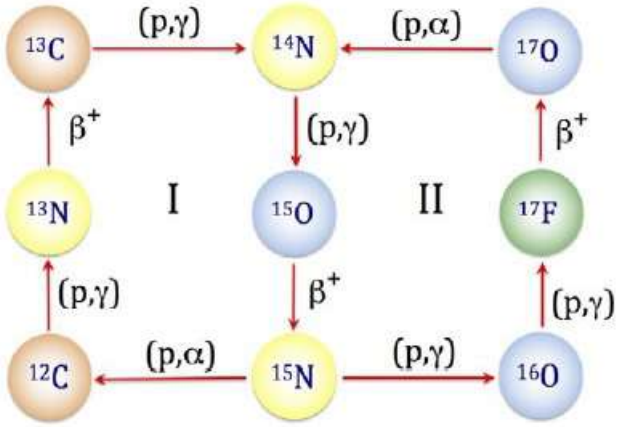

Figure 1.4: Bi-cycle CNO reactions.

elements, higher temperatures must be present in the stellar interior to allow CNO hydrogen burning. These higher temperatures correspond [14] to more massive stars, with $M > 1.5M_{\odot}$. The CNO cycle overtakes the p-p chains at a core temperature of approximately 20 MK (Fig. 1.5).

A more complete CNO reaction chain involves the ^{17}O nuclei branching out through the following reactions:

$$^{17}O(p,\gamma)^{18}F(e^+,\nu)^{18}O(p,\alpha)^{15}N. \tag{1.4}$$

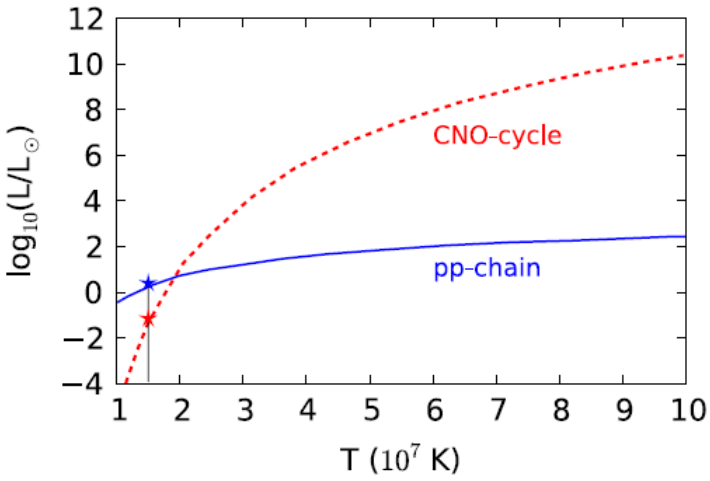

Figure 1.5: Temperature dependence of the energy production by the pp-chain and CNO cycles, assuming a CNO composition as that of the Sun. The passage by the Sun's core temperature is marked by "star" symbols [20].

thus opening up the formation of heavier elements (Fig. 1.6). In fact, another thermonuclear reaction $^{18}O(p,\gamma)^{19}F$ can compete with $^{18}O(p,\alpha)^{15}N$, successively feeding back the tri-cycle CNO or ending up with the synthesis of ^{20}Ne. This interplay has been the subject of a detailed study [7] [5] [9] of the stellar temperature (Fig. 1.7). For values between $2 \cdot 10^7$ K and $7 \cdot 10^8$ K a considerable number of ^{18}O atoms are subtracted from the third branch of the CNO tricycle by the $^{18}O(p,\gamma)^{19}F$ reaction. The reason is mainly due to the fact that the cross section of the $^{18}O(p,\gamma)^{19}F$ reaction has a narrow and isolated strong resonance at $E = 151$ keV.

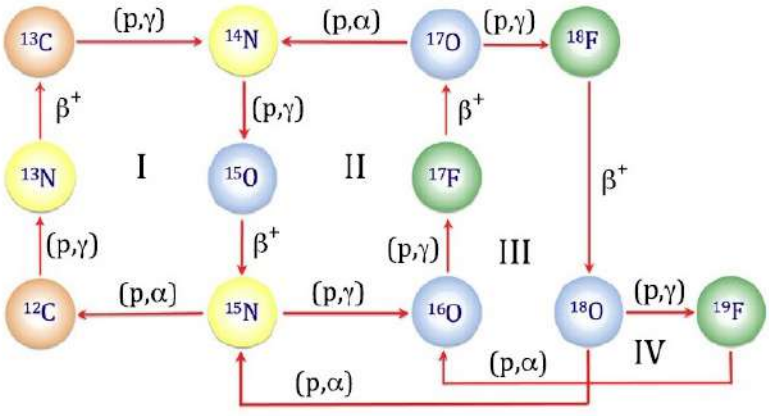

Figure 1.6: Complete scheme of the CNO cycle [20].

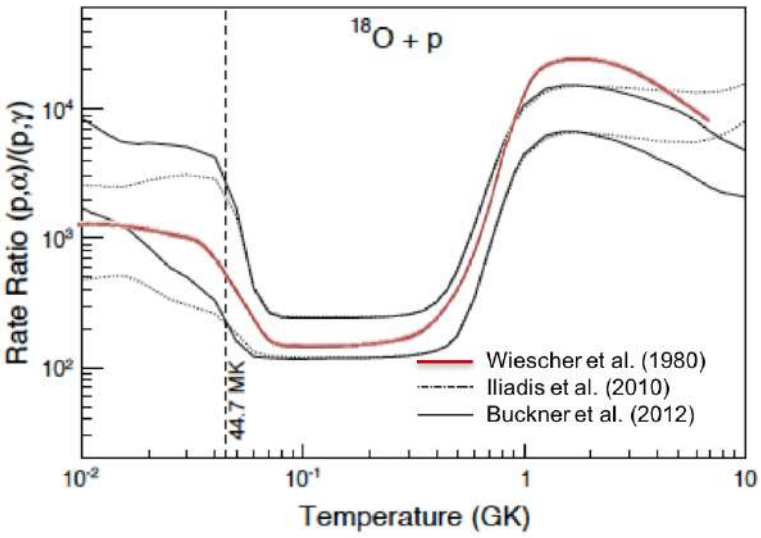

Figure 1.7: Ratio between the rates of the reactions $^{18}O(p,\alpha)^{15}N$ and $^{18}O(p,\gamma)^{19}F$ as a function of the stellar temperature T.

1.2 Cross sections and reaction rates

Two-body reactions occur in systems of a projectile X impinging on a target A. These represent the entrance channel, while the ejectiles Y and B emerging from the reactions are referred to as the exit channel.
The Q-value represents the energy released in a particular nuclear exoergic reaction. The total nuclear energy liberated in a stellar plasma per unit volume depends essentially on the Q-value of the involved reactions, on the nuclear cross section and the velocity distribution of the particles in the plasma. The nuclear cross section is a measure for the probability that a nuclear reaction will occur.
If we consider energy conservation, the Q-value is accounted as

$$Q = (M_X + M_A - M_B - M_Y)c^2 \tag{1.5}$$

where M_i is the mass of the i-th particle [14].
The reaction rate i.e. the number of reactions occurring per unit time and per unit volume of stellar gas consisting of N_X and N_A number densities of the interacting particles (in units of particles per volume) is:

$$r_{XA} = N_A N_x v\sigma(v) \tag{1.6}$$

where $\sigma(v)$ is the cross section in terms of v, that is the relative velocity of the two particles in the entrance channel. If velocity is distributed accord-

ing to a probability function $P(v)$, the reaction rate weighted over the $P(v)$ distribution is:

$$r_{XA} = N_X N_A \int_a^\infty vP(v)\sigma(v)dv \equiv N_X N_A < \sigma v >_{XA} \tag{1.7}$$

where $< \sigma v >_{XA}$ is defined as *the reaction rate per particle pair.*

Assuming the stellar plasma is approximately an ideal gas, the $P(v)$ can be described by a Maxwell-Boltzmann distribution:

$$P(v) = 4\pi v^2 (\frac{\mu}{2\pi kT})^{\frac{3}{2}} exp(-\frac{\mu v^2}{2kT}) \tag{1.8}$$

where T denotes the absolute temperature, k is the Boltzmann constant and μ is the reduced mass of the two-particle system.
Translating the $P(v)$ into the energy domain, the reaction rate per particle pair finally expressed in terms of kinetic energy, E, becomes:

$$< \sigma v >_{AX} = (\frac{8}{\pi\mu})^{\frac{1}{2}} (\frac{1}{KT})^{\frac{3}{2}} \int_0^\infty \sigma(E) exp(-\frac{E}{kT}) dE \tag{1.9}$$

The reaction cross section, $\sigma(E)$, in Eq. (1.9) depends on the mechanism by which the reaction proceeds at a given energy. All nuclear processes contributing to the total reaction cross section can be classified as either resonant or non-resonant [19].

In a non-resonant reaction or direct capture reaction (DC) the entrance channel X+A goes directly in the final compound nucleus trough a γ emission (Fig. 1.8). Instead in a resonant reaction a capture process exists in which an exited state of the compound nucleus is created in the entrance channel, it then decays (Fig. 1.9) by emitting a γ cascade.

At the low energies here involved the DC cross section $\sigma(E)$ is customarily expressed in terms of the astrophysical factor

$$S(E) \equiv E\sigma(E)e^{(2\pi\eta)} \tag{1.10}$$

where $\eta = \sqrt{\frac{\mu}{2E}} Z_p Z_t \frac{e^2}{\hbar}$ is the Sommerfeld parameter and Z_p e Z_t are the charge of the projectile and of the target, respectively.
Accounting for an energy dependence $\frac{1}{E}$ [14], and the Gamow factor $e^{(-2\pi\eta)}$, that describes the transmission though the Coulomb barrier at low energies of bombardment [19]. S(E) is a smoothly varying function of the energy and much more suitable for extrapolation than $\sigma(E)$ (Fig. 1.10) into the region of astrophysical importance (dotted line).

The reaction rate in terms of the S-factor:

$$< \sigma v >_{XA} = (\frac{8}{\pi\mu})^{\frac{1}{2}} (\frac{1}{KT})^{\frac{3}{2}} \int_0^\infty e^{(-2\pi\eta)} S(E) e^{(-\frac{E}{kT})} dE \tag{1.11}$$

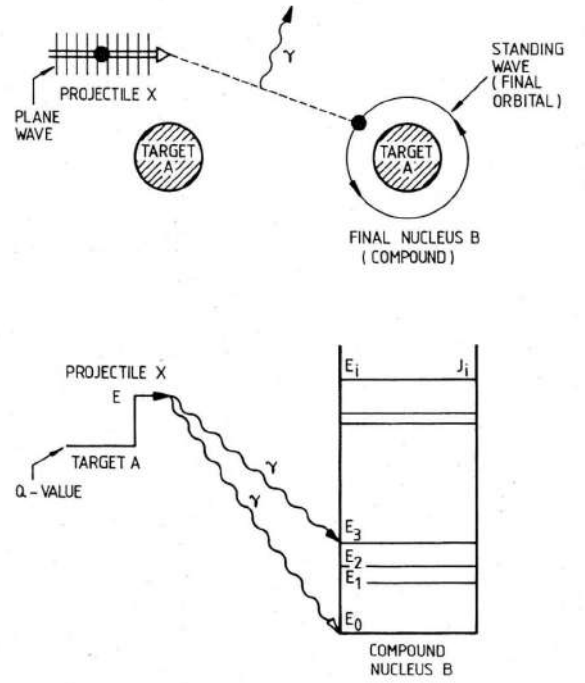

Figure 1.8: Illustration of non resonance mechanism, called direct capture [19].

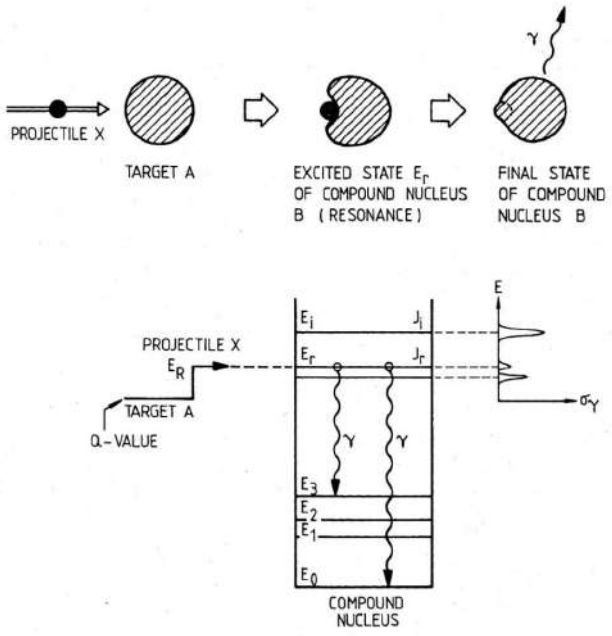

Figure 1.9: Illustration of a resonance mechanism [19].

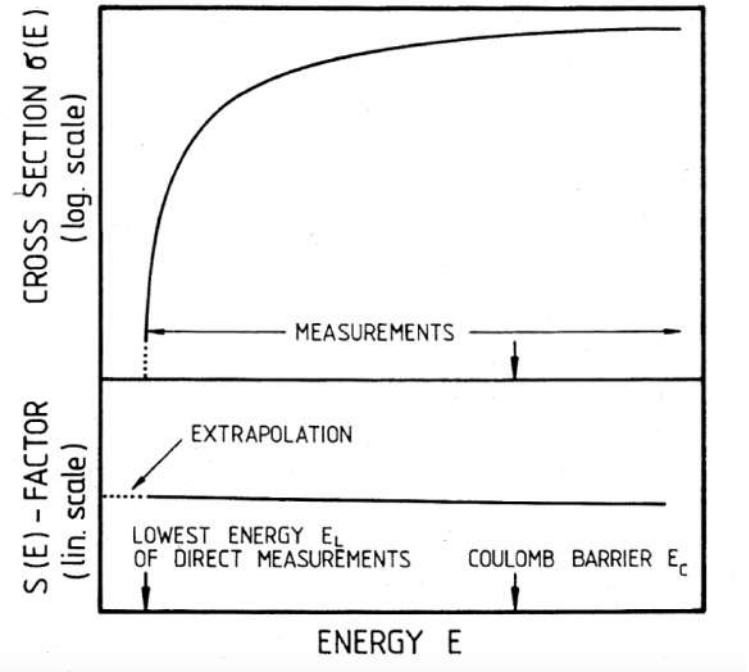

Figure 1.10: The cross section (upper plot) and the corresponding astrophysical S-factor (lower plot) for a typical non-resonant reaction. The dotted line represents the region of astrophysical importance where data extrapolation is required. The S-factor is more accurately extrapolated down to these low energies than the cross section [19].

remarks the rise of a narrow energy band (Gamow peak Fig. 1.11) with maximum energy value $E_0 \gg KT$ and width ΔE_0.

Commonly the astrophysical factor can be considered constant in this energy window $S(E) = S(E_0) = constant$, thus simplifying in the Eq. (1.11)

$$< \sigma v >_{XA} = (\frac{8}{\pi\mu})^{\frac{1}{2}} (\frac{1}{KT})^{\frac{3}{2}} S(E_0) \int_0^\infty e^{(-\frac{E}{kT} - \frac{b}{E^{\frac{1}{2}}})} dE \qquad (1.12)$$

where $b = (2\mu)^{\frac{1}{2}} \frac{\pi e^2}{\hbar} Z_1 Z_2$, the E_0 value that is obtained, represents the maximum value of the integrand $E_0 = (\frac{bkT}{2})^{\frac{2}{3}}$. The energy E_0 represents the most effective energy for a thermonuclear fusion reaction at a temperature T [19].

The resonant mechanism is usually very strong compared to DC and in some cases dominates the rates completely. If a single resonance is considered, the cross section is described by the Breit-Wigner formula:

$$\sigma_{BW}(E) = \frac{\lambda^2}{4\pi} \frac{(2J+1)(1+\delta_{XA})}{(2j_X+1)(2j_A+1)} \frac{\Gamma_{entrance}\Gamma_{exit}}{(E_{res}-E)^2 + \frac{\Gamma_{tot}^2}{4}} \qquad (1.13)$$

where E_{res} is the resonance energy, λ is the de Broglie wavelength, J is the

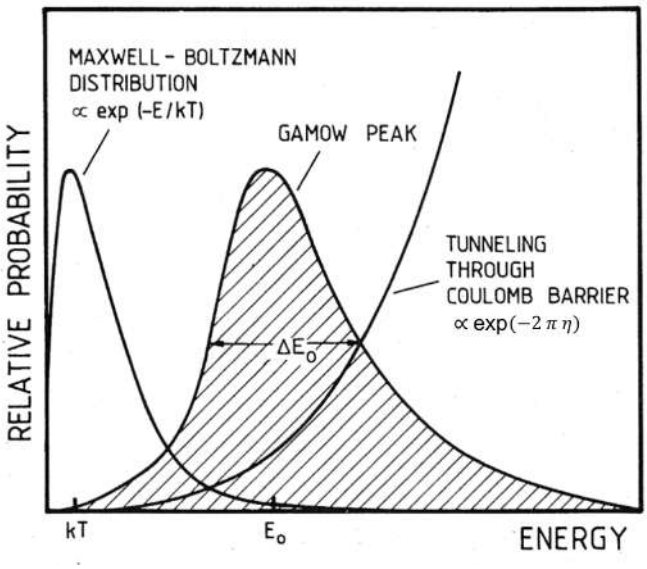

Figure 1.11: The "Gamow peak" is shown as a product of Maxwell-Boltzmann energy distribution and cross section(tunneling probability) [19].

spin of the resonance, j_X and j_A are the spins of the two particles and δ_{XA} is the Kronecker symbol. $\Gamma_{entrance}$ and Γ_{exit} are the partial width of the channels, and Γ_{tot} is the total width of the resonance.

Considering Eq. (1.9), Eq. (1.13) and the relation $\lambda^2=\frac{2\pi\hbar}{2\mu E}$, the contribution to the reaction rate due to a narrow resonance is:

$$< \sigma v >_{XA}= (\frac{2\pi}{\mu kT})^{\frac{2}{3}}\hbar^2\omega\gamma e^{(\frac{E_{res}}{kT})} \tag{1.14}$$

where $\gamma = \frac{\Gamma_A\Gamma_X}{\Gamma}$. The product $\omega\gamma$ is called *resonance strength*.

Narrow and isolated resonances contribute to the reaction rate simply as the sum of the single contributions:

$$< \sigma v >_{XA\,narrowres}= (\frac{2\pi}{\mu kT})^{\frac{2}{3}}\hbar^2 \sum_i (\omega\gamma)_i e^{(\frac{E_{res}}{kT})} \tag{1.15}$$

The contribution of a resonance is fundamental to the total reaction rate, and in the majority of the cases is predominant, reason for that its important to have the list of the possible resonances with the respective resonance strengths in the range of interest. If the total width of the resonance is large (i. e. the resonance is broad), also the energy-dependence of the partial widths has to be taken into account. The cross section formula becomes:

$$\sigma_{BW}(E) = \frac{\pi\hbar^2\omega}{2\mu E}\frac{\Gamma_X(E)\Gamma_A(E+Q-E_f)}{(E_{res}-E)^2+\frac{\Gamma^2}{4}} \tag{1.16}$$

Integrating the cross section 1.16, the reaction rate for a broad resonance is:

$$< \sigma v >_{XA\,broadres} = \frac{\sqrt{2\pi}\hbar^2}{(\mu kT)^{\frac{3}{2}}} \int_0^\infty \frac{\Gamma_X(E)\Gamma_A(E+Q-E_f)}{(E_{res}-E)^2+\frac{\Gamma^2}{4}} dE \qquad (1.17)$$

Once the cross section is integrated numerically, the reaction rate is obtained for a broad resonance dependent strongly by the energy.

The cross section and the S-factor curves including non-resonant and resonant contributions are shown in Fig. 1.12. The total cross section and the S-factor present peaks in correspondence of both resonant and non-resonant contributions.

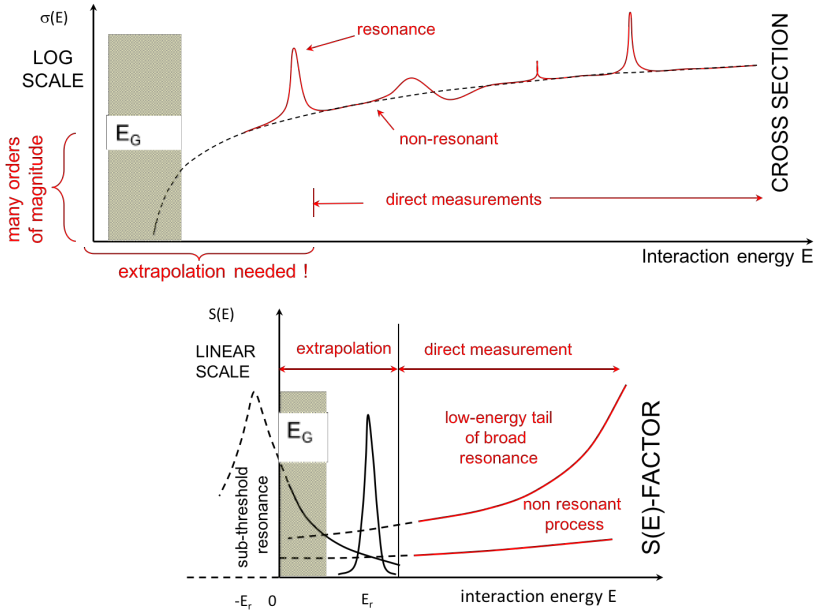

Figure 1.12: The cross section (upper plot) and the S-factor (lower plot) in which both resonant and non-resonant contributions are plotted.

1.3 Experimental requirements for cross section measurements

The direct measurement of nuclear reactions at low energies is a challenge due to the extremely low cross section involved and also because many parameters like stopping power and electron screening are not accurately known at low energies. An experiment well designed and theoretical efforts could reduce the uncertainties [19].

Several requirements are necessary to reach the optimal conditions in order to reproduce thermonuclear reactions in a laboratory, to measure the

cross section and to derive the reaction rates, to be used as input to stellar dynamics studies.

The experimental signal rate is too low to detect a significant number of reactions during the runs of an experiment in the Gamow energy window. An important limitation is therefore the high background rate, due to the environment and to the beam induced contamination.

Various methods of background reduction can be applied to reduce unwanted contributions, but no one has proven to be as effective as installing the experiment into deep underground, where several hundreds of meters of rock act as a massive passive shielding. The Laboratory for Underground Nuclear Astrophysics (LUNA) is located in the Gran Sasso National Laboratory, where an overburden of 1400 m of rock provides a shielding equivalent to about 3400 m of water, and greatly reduces the flux of cosmic radiation. The present work has used the LUNA facility to take data.

LUNA is the only facility operating at low background in the last few decades. Only very recently two similar underground experiments are starting a competition with LUNA: the Compact Accelerator System for Performing Astrophysical Research (CASPAR), located in Lead, South Dakota, at the former site of the Homestake Gold Mine, and The Joint Institute of Nuclear Astrophysics (JINA), located in the Jinping mountain of Sichuan, China, that is the deepest underground laboratory with horizontal access in the world, where the rock overburden in the laboratory is more than 2400 m.
The cosmic muon flux at LUNA is reduced [21] by six orders of magnitude compared to the flux on the surface. Also the neutron background is several orders of magnitude lower. In addition to the location of the experiment, the environmental and cosmic background contributions are further reduced on setups with multiple detectors and coincidence techniques in order to filter out background events from signals. One such experiment based on coincidence techniques is the Laboratory for Experimental Nuclear Astrophysics (LENA) in which for example the $^{18}O(p,\gamma)^{19}F$ reaction was reproduced and studied in the past, [5]. During the experiments a lot of precautions have been taken, since a very high beam current (100 μA) is needed to make much low cross sections measurable. This sets constraints on the maximum power dissipation of the cooling target system, in order to increase the targets lifetime.
Particular precautions have to be taken in order to prepare pure targets.
Finally, a reasonable choice of the detectors is important, in order to increase the detection efficiency or the energy resolution according to the aims of measurements.

1.4 Experimental Yield

Direct measurements of cross section are based on the production of particle beam to bombard a target, in order to detect the reaction products.

The physical quantity that allow to measure cross section directly from the experiment is the Yield, defined as the number of reactions per projectile. In the present section with the $^{18}O(p,\gamma)^{19}F$ as object of study, protons will be considered as projectiles, but the considerations are applied to ion beams in general [14].

The experimental Yield direct measurement needs long data acquisition, because the statistics accumulated from the counts of the detecting ejectiles is not very high in the Gamow window.
If a projectile of energy E_0 bombards a target of finite thickness, it loses an energy, when passes in the target.
The experimental Yield is thus defined accounting for the energy loss of the proton in the target, determined by the target stopping power $\epsilon = -\frac{1}{N}\frac{dE}{dx}$ and by the energy varying cross section $\sigma(E)$, integrated over the target thickness:

$$Y(E_0) = \int_{E_0-\Delta}^{E_0} \frac{\sigma(E)}{\epsilon(E)} dE \tag{1.18}$$

In case of thin targets, characterized by thickness $\Delta \ll E_0$, the stopping power $\epsilon(E)$ and the cross section are approximately constant over the integral, so the yield can be simplified as

$$Y(E_0) = \sigma(E_{eff}) \frac{\Delta}{\epsilon(E_0)} \tag{1.19}$$

where the quantity E_{eff} is the effective beam energy between $E_0 - \Delta E$ and E_0 at which 50% of the total yield is obtained. In general it could be calculated numerically or analytical expression [22], [19].
In the special case of a single narrow resonance at $E = E_{res}$, the experimental yield from the resonance rapidly vanishes for projectile energies below E_{res}. In the limit of an infinitely thick target $\Delta \to \infty$, above E_{res} it has the value [14]:

$$Y_{max,\Delta\to\infty} = \frac{\lambda_{res}^2}{2} \frac{\omega\gamma}{\epsilon(E_{res})} \tag{1.20}$$

The experimental yield determination is affected by the target composition in particular the substrate due to the energy loss. The effective stopping power must take in account the effects due to the inactive components too:

$$\epsilon_{eff} = \epsilon_{active} + \sum_i \frac{N_i}{N_{active}} \cdot \epsilon_i \tag{1.21}$$

the index i $\in$ inactive nuclides. A description of the procedure to prepare ^{18}O targets, for the present work is detailed in section 2.2.

1.5 ^{18}O(p, γ)^{19}F: Astrophysical motivation and previous state of the art

The majority of the matter of our solar system is characterized by a unique $^{18}O/^{16}O$ isotopic ratio equals to $2.09^{+0.13}_{-0.12} \cdot 10^{-3}$ [1]. The analysis coming from the study of presolar grains, gathered over the years from primitive meteorites and interplanetary dust particles gives us information about the isotopic ratio. Presolar grains are dust particles that condensed in the ejecta of evolved stars, supernovae, or, in some cases, classical novae [3]. Grains can provide insight into Galactic chemical evolution, stellar nucleosynthesis and evolution, and circumstellar and interstellar dust formation [3], [23].

The ^{18}O study presented in this thesis is motivated by observations of presolar grains that nucleated in the atmospheres of distant, evolved stars before the formation of the Sun. These grains conserve the isotopic ratios of the stellar surface they originated from. During the birth of the Sun, a lot of presolar grains were annihilated as gas and dust, collapsed to form a new star. Once the Sun is located on the main sequence, the survivors presolar grains were included into primitive meteorites. The $^{18}O(p,\gamma)^{19}F$ study focuses the attention on the abnormal isotopic ratios that provides crucial constraints for astrophysical models. The *Group2* that represents the 15% of all presolar oxides grains [3], is characterized by an $^{18}O/^{16}O$ signature $\leq 1.5 \cdot 10^{-3}$ [2], reflecting substantial ^{18}O depletion with respect to the Solar value [24].

The hypothesis is that the low-mass asymptotic giant branch (AGB) stars are an ^{18}O depletion site due to *cool bottom processing* (CBP) [2], having a mass range of a $(1.5-1.7)M_{\odot}$, in which $^{18}O + p$ reactions occurs. This *extra missing* process was proposed by Wasserburg et al. [25] to account for isotopic anomalies, including ^{18}O depletion, in presolar grains. During CBP, material circulates between the convective envelope and the radiative zone that separates the envelope from the hydrogen shell. The base of the convective envelope is cool. When the matter circulates around the hydrogen shell and the temperatures are high enough, the ^{18}O is destroyed via hydrogen burning. The processed material is then recirculated into the convective envelope and transported to the stellar surface. The process on which the CBP is based is not clear, and different explanations have been proposed, including magnetic buoyancy [26], gravity waves [27], shear instability [28] [29], meridional circulation [30] and convective overshoot [31]. The typical temperatures of the CBP for the AGB stars are approximately equal to 40 MK.

The depletion of ^{18}O in a stellar plasma at low temperatures is driven by $^{18}O(p,\alpha)^{15}N$ and, to a lesser extent, $^{18}O(p,\gamma)^{19}F$. The former reaction was recently studied by La Cognata et al. [32].

In the present work the cross section was measured for the $^{18}O(p,\gamma)^{19}F$ reaction. The reaction $^{18}O(p,\gamma)^{19}F$ has a Q value of 7994 keV. In stellar

scenarios there is a competition between $^{18}O(p,\alpha)^{15}N$ and $^{18}O(p,\gamma)^{19}F$, as discussed in subsection 1.1.2. While the reaction $^{18}O(p,\alpha)^{15}N$ closes the third

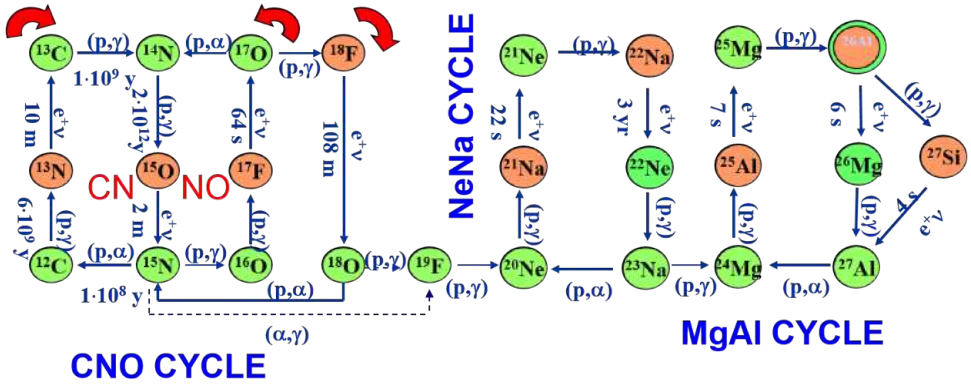

Figure 1.13: Reaction network with $^{18}O(p,\gamma)^{19}F$; exit point of the CNO cycle and starting point for the NeNa and MgAl. Stable nuclides in green.

branch for the CNO cycle, the $^{18}O(p,\gamma)^{19}F$ represents the closure for the CNO cycle and the starting point for the production of the heavier nuclei trough the NeNa and MgAl cycles, as shown in Figure 1.13. At typical temperatures of quiet hydrogen burning ($T \leq$1 GK) the $^{18}O(p,\gamma)^{19}F$ reaction is dominated by several resonances. Most of them have been directly measured in the past with large uncertainties on the resonance strengths.

Only a few of these resonances are of relevance for the astrophysical reaction rate. In stellar scenarios up to temperature of 0.1 GK, the reaction rate is mostly determined by non-resonant cross section and two resonances: a hypothetical low-energy resonance at $E_{Rlab} = 95 \pm 3$ keV, and the strongest resonance at $E_{Rlab} = 151$ keV. Fractional contributions suggested by Fortune et al. [6] at low AGB range temperatures are illustrated in Figure 1.14. The low energy resonance at $E_{Rlab} = 95 \pm 3$keV was never observed and its expected strength is disputed by [5] and [6].

In particular, the resonance at $E_{Rlab} = 95 \pm 3$ keV has been directly observed only in the (p,α) channel while no direct evidence has been found in the (p,γ) channel and only upper limits for the resonance strength have been given.
There are other weak resonances at a $E_{Rlab} = 216$ keV, 274 keV and 334 keV, that have a negligible influence ($< 1\%$) on the total reaction rate, [7], therefore they are not astrophysically relevant.

The resonance strengths estimates present in the literature are reported in Table 1.2:

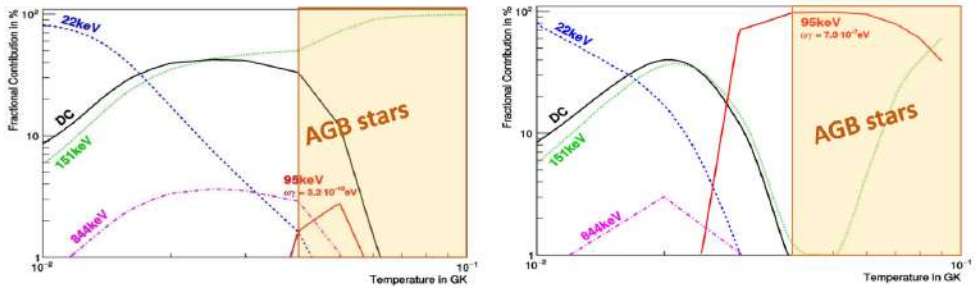

Figure 1.14: Reaction rates contributions in the AGB range of stars, on the left follows as [5] and on the right follows as [6]

Table 1.2: Strengths comparison

$E_{plab}(keV)$	$\omega\gamma$(meV) Buckner *et al.*[5]	$\omega\gamma$(meV) Fortune *et al.*[6]	$\omega\gamma$ (meV) Wiescher *et al.* [7]	$\omega\gamma$(meV) Vogelaar *et al.*[8]	$\omega\gamma$(meV) Iliadis *et al.*[33]
95	$\leq 7.8 \cdot 10^{6}$	$0.0007^{+0.0056}_{-0.0038}$		$\leq 4.0 \cdot 10^{-5}$	
151			1.0±0.1	0.92±0.06	
216			>0.008	0.005±0.001	0.005±0.001
278			0.037±0.005		0.0024±0.005
334			0.95±0.08		

1.6 ^{18}O(p, γ)^{19}F at LUNA: experimental campaign

The goals of the proposal for the direct measurement of the $^{18}O(p,\gamma)^{19}F$ low energy cross section in low background conditions are get some evidence of an hypothetical low energy resonance at $E_{Rlab} = 95 \pm 3keV$ and to improve our knowledge of levels in the ^{19}F compound nucleus that are relevant to nuclear astrophysics. This implies the measurement of off-resonance branching ratios, on-resonance branching ratios and the direct cross section.

Five resonances were measured at LUNA2 facility, all possible resonances within (Fig. 1.15) the LUNA range 89-400 keV. An exploratory measurement was done in order to estimate the resonance strength for the low energy resonance at $E_{Rlab} = 95 \pm 3$ keV, and in addition measurements, to reduce the error on the $E_{Rlab} = 151$ keV, $E_{Rlab} = 216$ keV, $E_{Rlab} = 274$ keV and $E_{Rlab} = 334$ keV resonance strengths.

The data taking campaign for the present experiment was split into two phases. The first phase was performed with a high efficiency BGO summing crystal detector. On the contrary, the second phase was more based on high energy resolution provided by a high purity Germanium detector. Both approaches used a solid target set-up and covered the common range of data taking 140-400 keV. The first phase extended the range of measurements to energies down to $E_{Rlab} = 89$ keV, because thanks to the high efficiency of the

BGO summing crystal detector, it was planned to get information or evidence about the low energy resonant cross section.

Several measurements of environmental backgrounds were performed during the two phases, and beam induced background measurement was taken during the first phase in order to understand the influence of the different contaminants.

In the following Chapter 2 the experimental apparatus and methods will be detailed.

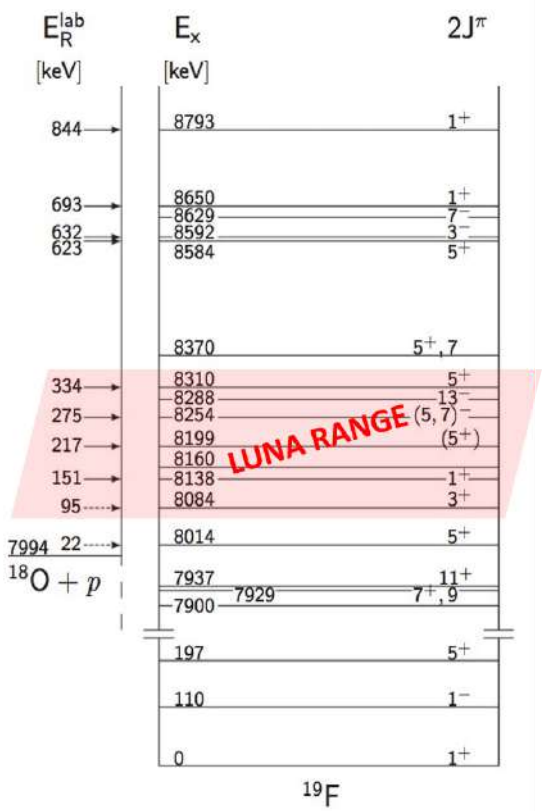

Figure 1.15: Level scheme of the compound nucleus ^{19}F. The resonances in the $^{18}O(p,\gamma)^{19}F$ reaction measured in the LUNA range are highlighted in red [7].

Chapter 2

The ^{18}O(p, γ)^{19}F experiment: materials and methods

2.1 The Laboratory for Underground Nuclear Astrophysics (LUNA)

The Laboratory for Underground Nuclear Astrophysics (LUNA) is located at the INFN Gran Sasso National Laboratory (LNGS), Italy. Initially a compact 50 kV "homemade" LUNA I accelerator [34] was installed for pilot experiments [35], [36], [37]. In the year 2000 a high current 400 kV electrostatic accelerator (LUNA II) with a radiofrequency ion source (Fig. 2.1) was installed, based on the Cockcroft-Walton design [10].

The source provides very accurate and reproducible ion beams of proton and alpha particles in the range 50-400 keV with a maximum current on-target up to 300 μA and an energy spread of 0.1 keV.

The facility has two beamlines (Fig. 2.2 and 2.3): one of them is dedicated to solid target, the other one to gas target measurements.
The solid target beamline has been used for studying the reaction of interest in the present work and it is composed of different parts, that will be briefly described below. The accelerator is enclosed inside a tank containing an insulating mixture of N_2 and CO_2 at a pressure of 20 bar, in order to avoid sparks between the various high voltage parts.

The proton source stems from a hydrogen plasma confined by an axial magnetic field (radiofrequency-ion source). The protons are extracted by an electric field between the extraction canal and the metallic electrode at the top of the source. The extraction voltage ranges to 3-10 kV [19]. As illustrated in Fig. 2.4, once extracted from the source, the proton beam is accelerated, guided and focused to the target station by means of 0° dipole analysing magnet, a horizontal steerer for correcting the beam bending , a Q-pole for focusing the beam, a first Faraday cup for monitoring the beam

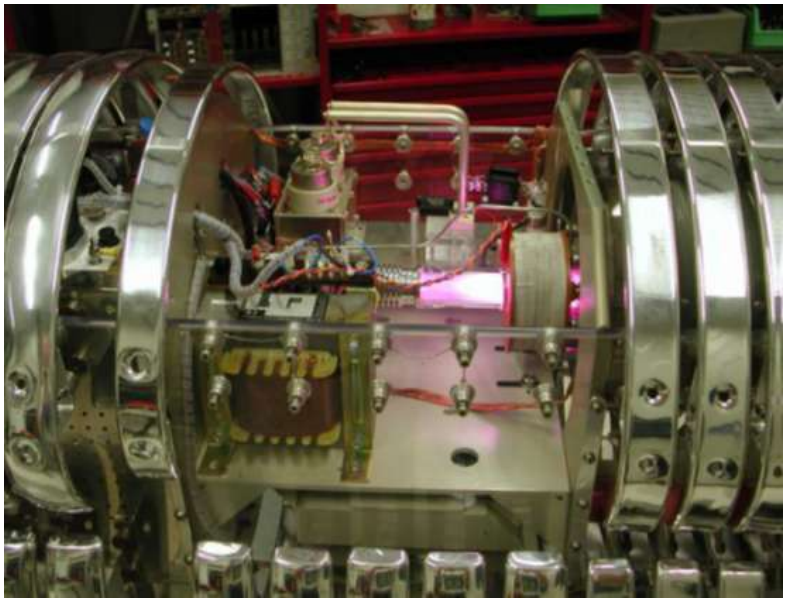

Figure 2.1: LUNA II proton source.

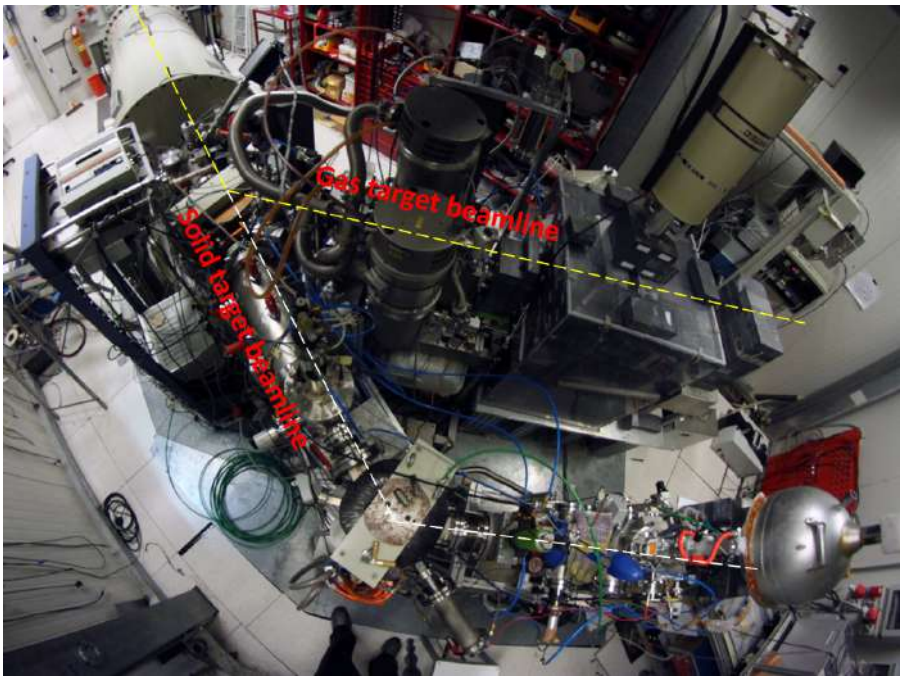

Figure 2.2: The solid target beamline on the left and the gas target beamline on the right.

current, a 45° dipole analysing magnet that deviates the beam, a vertical steerer, a first aperture, a second Faraday cup, a second aperture ensuring the determination of the beam line in alignment with the first in such a way,

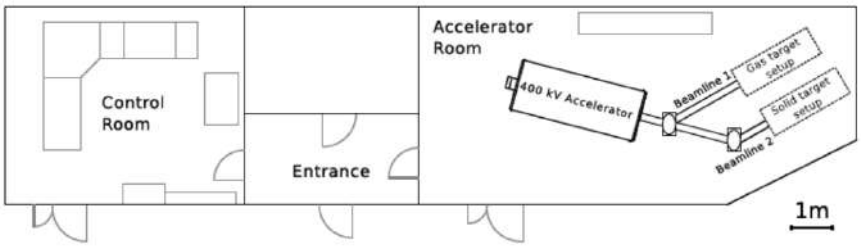

Figure 2.3: Sketch of the floor plan of the LUNA facility underground at LNGS [38].

that only the target surface is hit by the beam, a cold trap filled with liquid nitrogen (LN_2) for reducing the beam-line contaminants and preventing the build-up of carbon on the target surface and the target chamber. The target chamber, finally isolated from all other beam-line components acts as a Faraday cup for measuring the accumulated charge. A bias voltage of -300 V is typically applied to the cold trap in order to suppress secondary electrons emitted when protons strike.
The target cooling is ensured by a de-ionised water circulation system. A turbo pump installed below the cold trap maintains a pressure of approximately $5 * 10^{-7}$ mbar inside the target chamber.

Two detectors were located close to the target chamber during the two phases of the experimental campaign, a Bismuth Germanium Oxide (BGO) detector for the first phase and a high purity Germanium (HPGe) for the second one, at 0° and 55° with respect to the beamline, respectively. Both detectors were properly shielded, in order to reduce the environmental background. A detailed description of the target and of the two detector setups will be delivered in the following sections of this chapter.

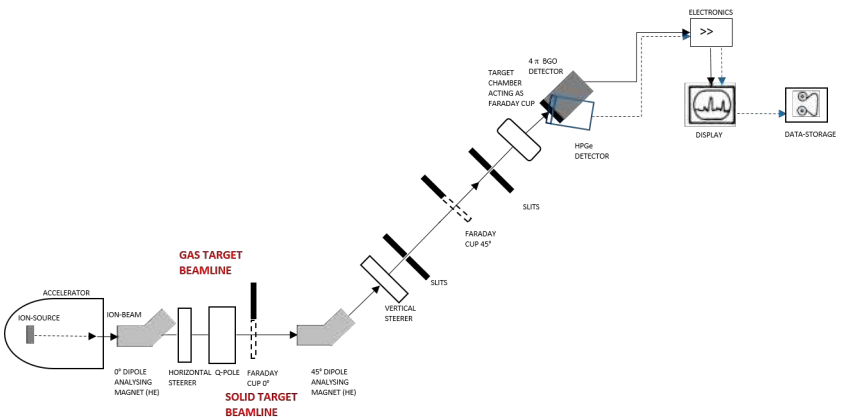

Figure 2.4: Schematic diagram of the solid target beamline.

2.2 Solid target setup

In the experimental investigation of reaction cross-sections at the sub-Coulomb energies of astrophysical interest, solid targets have to meet a number of specific requirements. Suitable and stable thickness, so as to sustain high beam currents over extended times. Known and constant stoichiometry, so as to allow for accurate beam energy loss calculations. Known and possibly enriched isotopic composition, so as to allow for measurable yields. Each of these features should be measured to a high degree of accuracy to allow for the correct interpretation of reaction yields and thus of cross-section data.
Finally, the target properties should be carefully monitored since changes in thickness, stoichiometry and/or composition under beam irradiation directly affect the measured absolute cross sections and may lead to significant systematic errors.

2.2.1 ^{18}O targets preparation

The procedure used to prepare solid Ta_2O_5 targets with an isotopic enrichment in ^{18}O of 99% is described here.
The Ta_2O_5 targets have been prepared for the study of the $^{18}O(p,\gamma)^{19}F$ reaction by anodic oxidation of thin tantalum disks (0.3 mm x 40 mm diameter). This technique allows the targets to be produced with highly uniform stoichiometry and homogeneous thickness. It consists of a dissociation process of the water and in the consequent recombination of ions O^{2-} with the ions of metal.

The basic chemical reaction of the process is:

$$2Ta + 5H_2O = Ta_2O_5 + 5H_2 \tag{2.1}$$

Initially a cleaning process has been carried out, so the tantalum disks were bathed in a citric acid solution for approximately 1 hour at a temperature of 90°C. This etching phase was intended to remove surface impurities and prepare the tantalum for the anodization process. Citric acid was specifically chosen to avoid fluorine, which gives rise to an intense gamma-ray background which hampers the analysis of our spectra at certain measured energies.

The anodizing apparatus (Fig. 2.5, 2.6) is composed by a cylindrical annulus of Teflon (100 mm and 25 mm outer and inner diameter, respectively, 25 mm height) fixed on a cylindrical base of stainless steel.
The choice of Teflon ensures a good electrical insulation and thermal stability. The electrolytic solution is placed in the cavity of Teflon which defines the effective volume of the anodizing cell.

The anode of anodizing cell is a tantalum disk placed at the bottom of the Teflon cylinder and maintained at ground potential through contact with a metallic spring (positive pole).

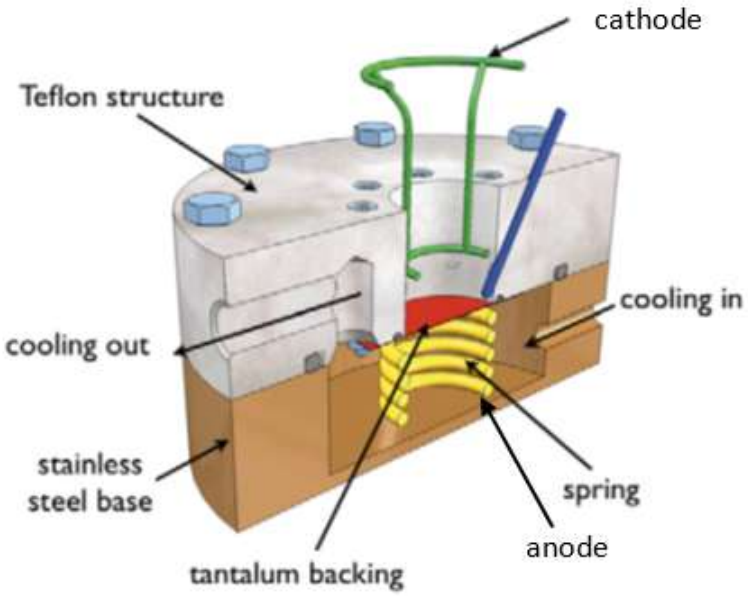

Figure 2.5: Sketch of the anodisation device, consisting of a Teflon annulus mounted on a stainless-steel base. A tantalum disk placed at the interface between the Teflon and the stainless-steel base acted as the anode while a gold-nickel basket inserted in the hole acted as the cathode. The cavity in the Teflon defines the volume where the electrolytic solution was placed. A refrigerating fluid kept at constant temperature was circulated inside the device to avoid evaporation of the solution during the anodisation process [11].

The electrolytic solution consisted of a mixture of 20μl of KI and 2 ml of 99.9% ^{18}O enriched water. The KI electrolyte was chosen because the anion contains no oxygen that could affect the final stoichiometric ratio of the anodized Ta target and its salt crystallizes without water hydration. The cathode (negative pole) that is a basket, consisted of 90% gold and 10% nickel alloy and has a diameter of 2 cm. It was brought into contact with the surface of the electrolyte solution at a distance from anode of 1.90 mm placed and adjusted in co-axial symmetry. This configuration is useful to minimize bubbles production inside the electrolyte and to have a homogeneous deposition growth.

A stabilized DC power supply was connected to the anode, the voltage up to a maximum value of 25 V. The applied voltage provides the energy to

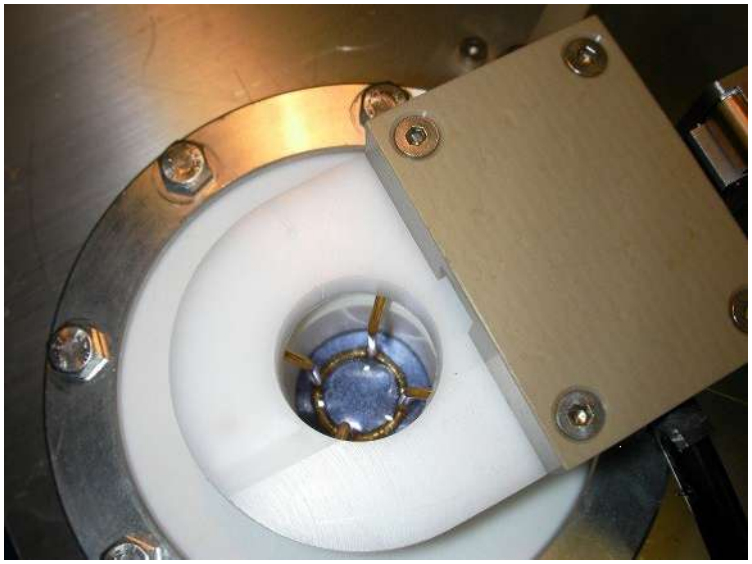

Figure 2.6: Picture of anodizing apparatus.

favour the reaction (2.1) making Ta_2O_5. This process was monitored through a PC running LabView software controlling the ramp up and down of the DC power supply until the current inside the electrolyte solution gets to a constant value of 2 mA [11].

The formation of thin films at low temperatures follows a logarithmic rate law. The growth of the oxide is determined by the rate at which ions jump from the metal or from the absorbed oxygen layer into the oxide under the influence of the electric field. The formation of Ta_2O_5 as a result of anodic oxidation has been found to obey the empirical relationship (2.2), where I is the current flowing through the electrolyte, t the time of growth, and a e b temperature-dependent parameters, d the thickness [39].

$$\frac{I}{d} = a - b \ln t \tag{2.2}$$

Depositions with best oxide film growth rates and homogeneity were obtained at 25°C, which was maintained using circulating water, in this case both current and voltage do not present spikes, so they remain stable. Anodic films exhibit brilliant interference colors which practically may be used as a measure of thickness, in fact for each of these colors corresponds a nominal thickness. The colors changes are sufficiently clear that thickness variations of less than 10% are readily observable [39]. The process of growth is rapid, about 2 minutes, and the aspect of one of the Ta_2O_5 targets produced before beam exposure is shown in Fig. 2.7.

In these conditions I/d is approximately constant, so the thickness of the oxide film is proportional to the applied voltage and thus to the current

Figure 2.7: Photograph of one of the Ta_2O_5 targets produced before beam exposure.

flowing through the electrolyte. The thickness of the film can be calculated in nm through [39] Vermilyea's relation:

$$d = 1.9225(V + 1.4)nm \tag{2.3}$$

Targets of two different thicknesses were produced setting two applied voltages at 25 V, and 12 V, so the estimated thicknesses using Eq. (2.3) are d=50.76 nm and d= 25.76 nm, respectively.

2.3 4π Bismuth Germanium Oxide (BGO) detector

2.3.1 Scintillator and photo detectors

$Bi_4Ge_3O_{12}$ (BGO) is a scintillation material, commercially available as crystals of reasonable size. A major advantage for the detection of γ rays is its high density (7.13 g/cm^3) and the large atomic number (83) of the bismuth component. These properties result in the largest probability per unit volume of any commonly available scintillation material for the photoelectric absorption of gamma rays [40].
The BGO detector has a high detection efficiency, and the combination of the six crystals in a 4π geometry has the aim to maximize this important property, useful to detect gamma rays in a total cross section measurement configuration. This is up to the strong summing effects. The use of this kind of detector allows to focus the measurement around the Q-value of the (*,γ) reactions of interest in the gamma-rays spectra in which there are negligible environmental background effects.
The six crystals were optically isolated and connected to photomultiplier

tubes placed at one side of the bars, the other side is covered by a plastic light reflector. This segmentation of the detector allowed for the possibility of recovering some information about the individual gamma rays in the cascades, while summing the single crystal signals of one coincident event maximizes the summing efficiency, similar to have a detector with one large crystal.

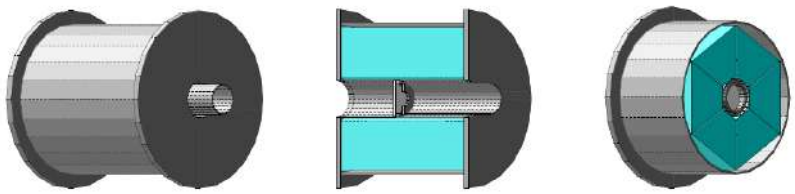

Figure 2.8: Sketches of the BGO detector including the target chamber in the middle of the detector [41].

The geometry of the detector is composed of six prismatic segments (approximately $52cm^2 * 28cm$) located in a 4π geometry around the target. The BGO detector has been used during other experimental campains at LUNA [36][42][43], a detailed description is in [44].

2.3.2 Electronics and data acquisition

The electronic chain including the Data Acquisition (DAQ) is schematized in Figure 2.9. The voltage for each PMT (Hamamatsu R1847-07) could be set individually by a programmable VME high voltage supply (CAEN V6533). The anode outputs of the six PMTs were connected the six preamplifiers ORTEC 113. The output of a pulse generator (Ortec 419) was also connected to the test inputs of the six PMTs and to the test input of a seventh preamplifier (ORTEC 113).
The DAQ was based on a digitizer (CAEN V1724), with 8 channels, a resolution of 14 bit and a sampling rate of 100 MS/s. The digitizer firmware supported pulse height analysis [45], [46] of the digitized signal on the internal FPGA. The software "MC2 Analyzer" by CAEN was used for the acquisition of list mode data, acquiring and saving information event by event. Each saved event consisted of a trigger timestamp, energy and some additional information to indicate special events and conditions (such as an ADC overflow). Channel 1-7 of digitizer were connected to the preamplifiers of PMTs and of the pulser signal, while channel 0 was connected to the pulse generator (BNC PB-5) that is triggered by the current integrator to record the current on target.
In this configuration, the accumulated charge registered in the current integrator is directly proportional to the number of pulses. Thanks to the list

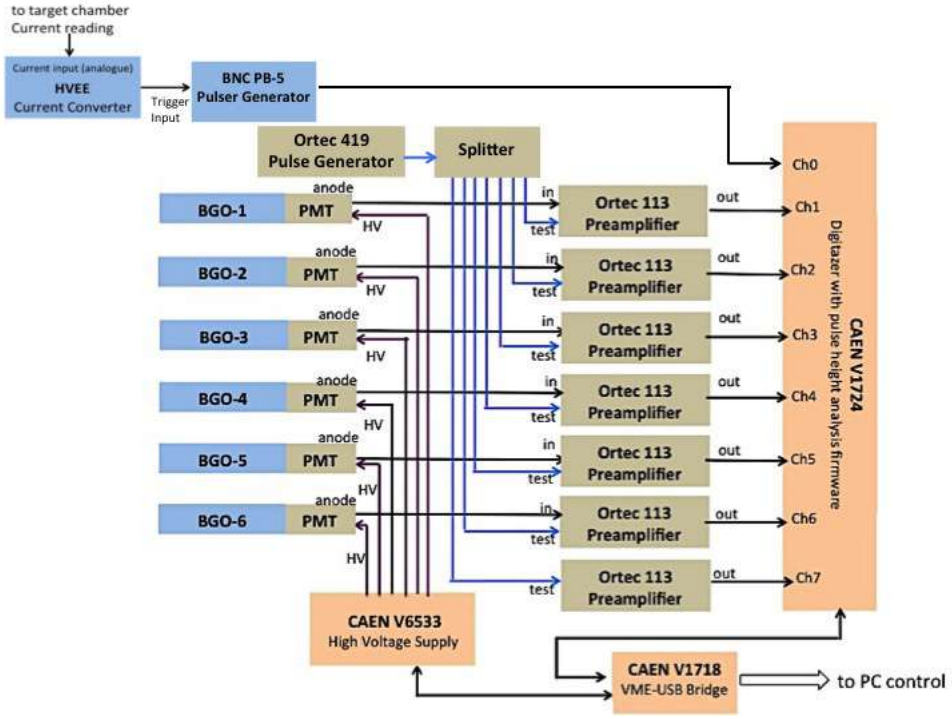

Figure 2.9: Block diagram of the BGO electronic chain.

mode capability, the development of the acquired spectra and the current on target during the measurement (i.e. in time or with accumulated charge) can be recorded.

2.3.3 Data processing

A specific software tool [47] made available from the LUNA Collaboration was used to process acquired data. This tool allowed creating the sum spectrum obtained event by event merging independent data coming from the six BGO segments. The coincidence window was optimized at a value of $3.5\mu s$, in order to reduce the pile-up effects. In this way it was possible to exploit the benefit of the capabilities of the 4π BGO detector, in order to increase the measurement efficiency.

The events that are caused by signals provided by the pulse generator and fed to the test input of the seventh preamplifier have been removed from the energy spectrum, as they do not correspond to a physical interaction in the detector. A separate analysis of these events gives information on the dead time of the data acquisition system during the measurement. The seventh preamplifier that had only the test input connected served as the clock for these "pulser events".

The energy calibration was determined from the single crystal spectra ob-

tained in measurements of known radioactive sources as e.g. ^{137}Cs, ^{60}Co or well known (p,γ) reactions as e.g. $^{14}N(p,\gamma)^{15}O$. The information regarding the energy calibration were used to create calibrated histograms. The histograms acquired with the BGO will be named single and sum from now on.

2.3.4 Shielding and environmental background considerations

In order to reduce the environmental background a lead shielding was mounted around the BGO detector [48]. The configuration with the BGO detector is surrounded by 10 cm of lead and the different parts in which the shielding is composed are positioned on the rails to be moved easily in and out the target chamber. A picture of the shielding is shown in Figure 2.10, and a comparison between the environmental backgrounds sum spectra, acquired respectively on surface with 10 cm of shielding [49], underground without shielding, and underground with 10 cm of shielding is shown in Fig. 2.11.

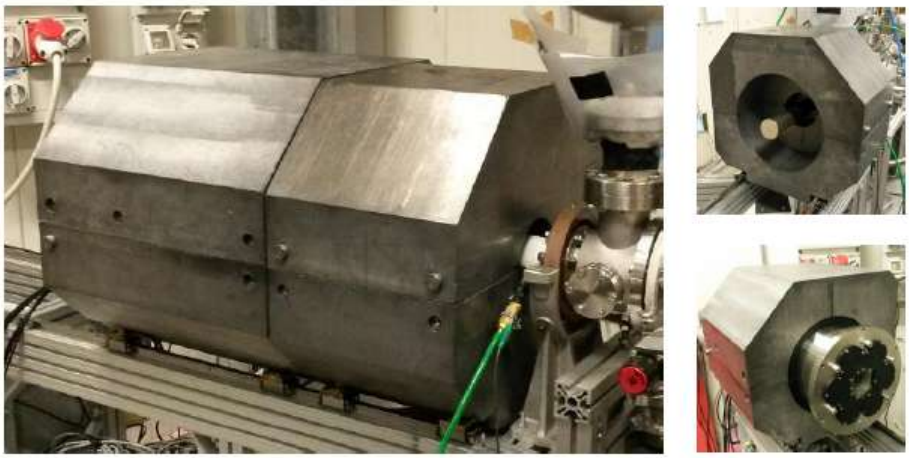

Figure 2.10: Lead shielding in the BGO configuration.

The region of interest for the $^{18}O(p,\gamma)^{19}F$ experiment is around the Q-value, 8 MeV. The BGO background spectrum taken at the earth's surface, up to E_γ =3.7 MeV is dominated by natural radioisotopes, the long plateau extending from 3.7 MeV on upwards is caused by cosmic rays and, to a lesser extent, also by muon induced neutrons [49].
The 10 cm of lead appears to provide sufficient shielding against environmental gamma rays for the underground location, in fact the main environmental lines ^{40}K at 1.46MeV, or ^{208}Tl at 2.61MeV are reduced significantly. Spectra acquired with shielding both on surface and underground location are char-

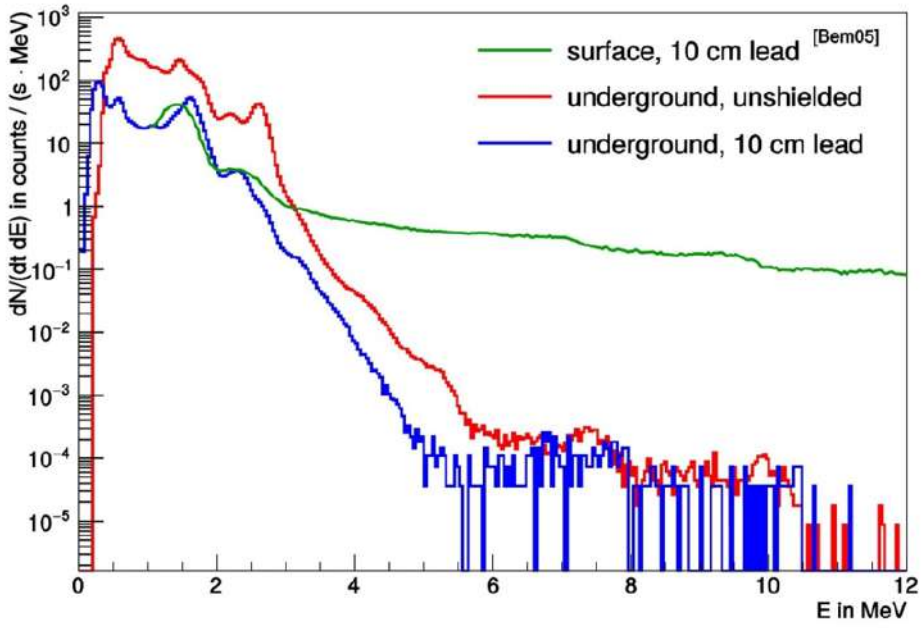

Figure 2.11: Effect of the location and shielding on the BGO detector background.

acterized from 2340 keV and 1633 keV states in ^{207}Pb that are populated by the electron capture of ^{207}Bi, which is known as an intrinsic background to BGO detectors [50] [51] and decays by electron capture with a half-life of 31.55 years. The background in the energy range 6-11 MeV is dominated by events from radiative neutron capture [47]. The [47] thermal neutrons were considered as the main contribution to the background signal. The radiative capture, (n,γ), has large Q values for many of the materials that are used in the detector, and the gamma rays emitted following that reaction can be registered as events with large sum energies.

In the context of $^{18}O(p,\gamma)^{19}F$, the Q value of the reaction lies in the energetic range of background characterized by thermal neutron capture, the reduction of this kind of background is minimum, but it is evident. From the simulation obtained by the model [47], [48] a further kind of shielding (e. g. with borated polyethylene or boron carbide) could be a good solution for the reduction of the background due to the thermal neutrons. It should be taken into account for the next experiments.

2.4 High-purity Germanium (HPGe) detector

2.4.1 Experimental setup

The operation of an HPGe detector is based on the semiconductive features of germanium: an energy deposition comes from ionizing radiation creating free charge carriers (electrons and holes), which can be registered as an electronic signal when a voltage is applied [40]. The quoted relative efficiency of the coaxial p-type germanium detector (ORTEC GEM120225-P-ST) at 1.33 MeV was 121% in 2001 [40] [52]. A more recent measurement by the manufacturer in 2016 determined a value of 104% for the same efficiency [53]. In the setup of the HPGe detector, the target chamber was positioned at an angle of 55° with respect to the proton beam. The detector was located in front of the target chamber. The 55° alignment was chosen in order to mitigate any angular distribution effects [54], in fact the Legendre polynomial P_2 vanishes for $\cos^2\theta = 1/3$. The measurements were done putting the target chamber in a close geometry configuration with the detector, at a distance of 7 mm, corresponding to about 20 mm distance to the beam spot.

2.4.2 Electronic chain and data acquisition (DAQ)

A scheme of the electronic chain including the DAQ is shown in Figure 2.12. A CAEN N1471HET high voltage power supply fed the +4900 V bias voltage for the HPGe detector. The signal coming from the preamplifier integrated into the detector was amplified by an ORTEC Model 671 spectroscopic amplifier, and fed into the input 1 of an ORTEC ASPEC-927 Multi-Channel Analyzer (MCA) converting the pulse height in a range of 16,384 bins.
The pulse generator (BNC PB-5) that is triggered by the current integrator to record the current on target was connected to the input 2 of the MCA, so that an event in the second MCA channel corresponded to a fixed amount of charge on target and thus allowed the charge on target to be recorded together with the gamma ray spectrum.
The software used to acquire the spectra was ORTEC's MAESTRO for Windows. The gamma-rays counts bin spectrum, also information about the real time and the live time are recorded by the Multi-Channel Analyzer for each run.

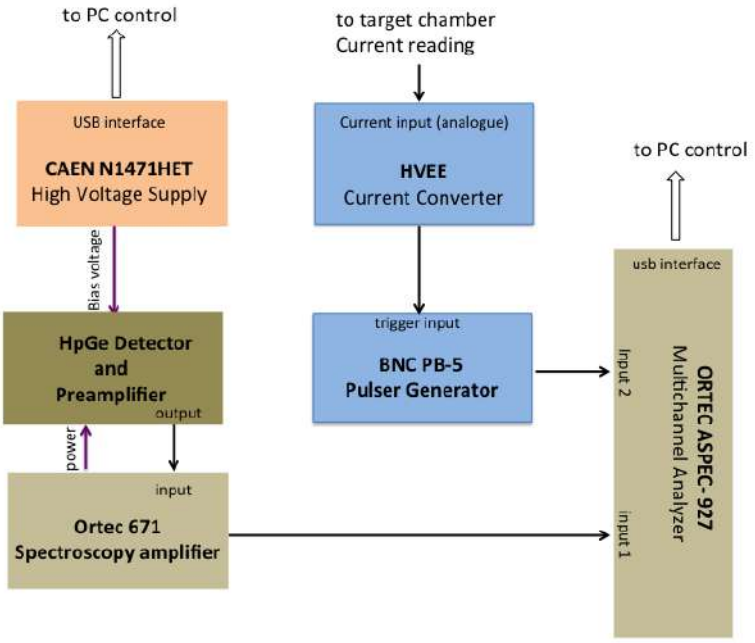

Figure 2.12: Block diagram of the HPGe electronic chain.

2.4.3 Shielding and environmental background considerations

As for the BGO detector, a lead shielding was mounted around the HPGe detector [48]. The setup with the HPGe detector is shielded by 15 cm of lead and the different parts in which the shielding is composed are positioned on the rails, as the BGO case (Fig. 2.13). A comparison between the environmental backgrounds spectra, acquired on surface without shielding, underground without shielding, and underground with 15 cm of shielding respectively is shown in Figure 2.14.

Figure 2.13: Lead shielding in the HPGe configuration.

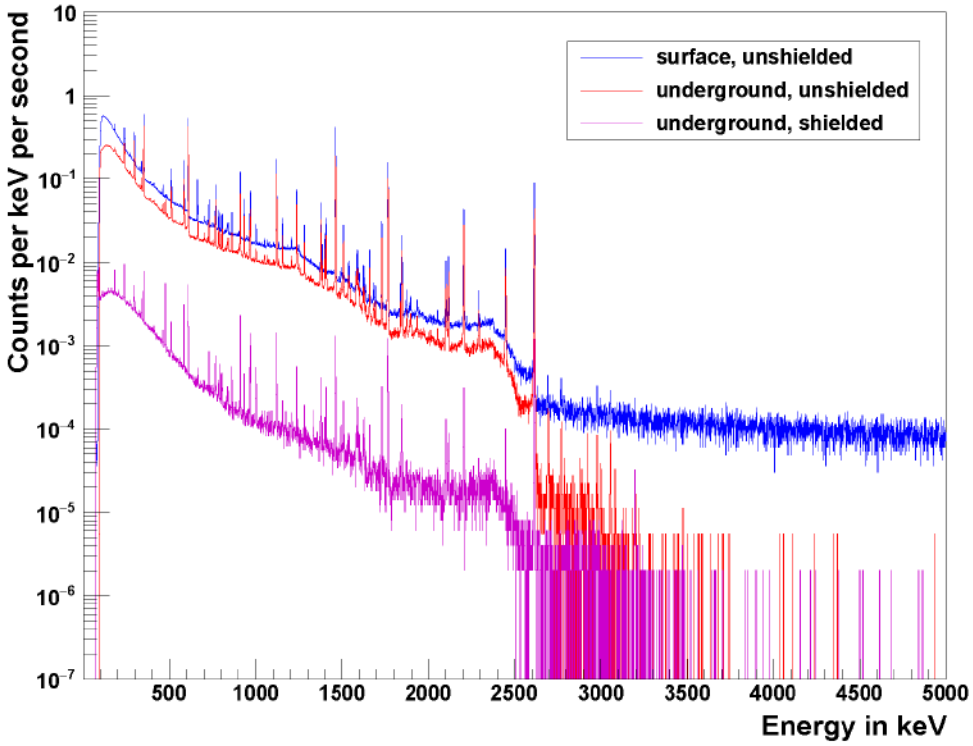

Figure 2.14: Effect of the location and shielding on the HPGe detector background.

The environmental background above 3 MeV is remarkably suppressed with 15cm of shielding. On surface the continuous background induced by cosmic rays is prominent up to 3 MeV, and abundantly suppressed for the detector in the underground location.

2.5 Comparison between BGO and HPGe detector

The two detector setups were used for different purposes.
The BGO detector is characterized by an high efficiency, approximately 40% at 8 MeV. Each of the six segments of the BGO detector has a significant size, so the summing effects due to the gamma ray cascades are consistent, and could be considered a limitation. An important disadvantage of BGO is the poor energy resolution (hundred keV at MeV energies), a factor 30 worse than for the HPGe detector. Due to the poor resolution, there are only few lines that are well-separated and that can be easily identified. The single BGO detector allows to distinguish only the strongest transitions, instead the

summed six crystals 4π BGO configuration shows a strong clear signal at the energy of the excited level, of the compound nucleus ^{19}F.
The HPGe detector has instead a high energy resolution (few keV at MeV energies) thus resolving very well the single transitions of the ^{19}F cascades and of the lines coming from concurrent reactions, due to contaminants.
One can consider for example, the deexcitation of the well known $E_X = 8138$ keV level in the compound nucleus ^{19}F, in order to compare spectra acquired respectively with BGO and HPGe. A comparison between three spectra acquired respectively with BGO coming from the single BGO segment, from the sum of the six segments, and with the HPGe detector, is shown in Fig. 2.15.

The main goal of the BGO measurements is to search a hypothetical low energy resonance at 95 keV, that has never been observed. The high efficiency of the BGO detector setup could make possible to access such detailed such low rate event. The HPGe setup instead allows the detailed study of the transitions regarding the non-resonant and resonant range. Four resonances and the direct capture component were measured using both BGO and HPGe setups. The resonances measured are: the 151 keV resonance that is the strongest and well known in literature, the unknown 216 keV resonance, here measured for the first time in detail the 274 keV, and the 334 keV resonances. The high energy resolution of the HPGe detector allows a determination of the branchings ratio of primary gamma rays in the on and off-resonant range and consequently of the resonance strengths.

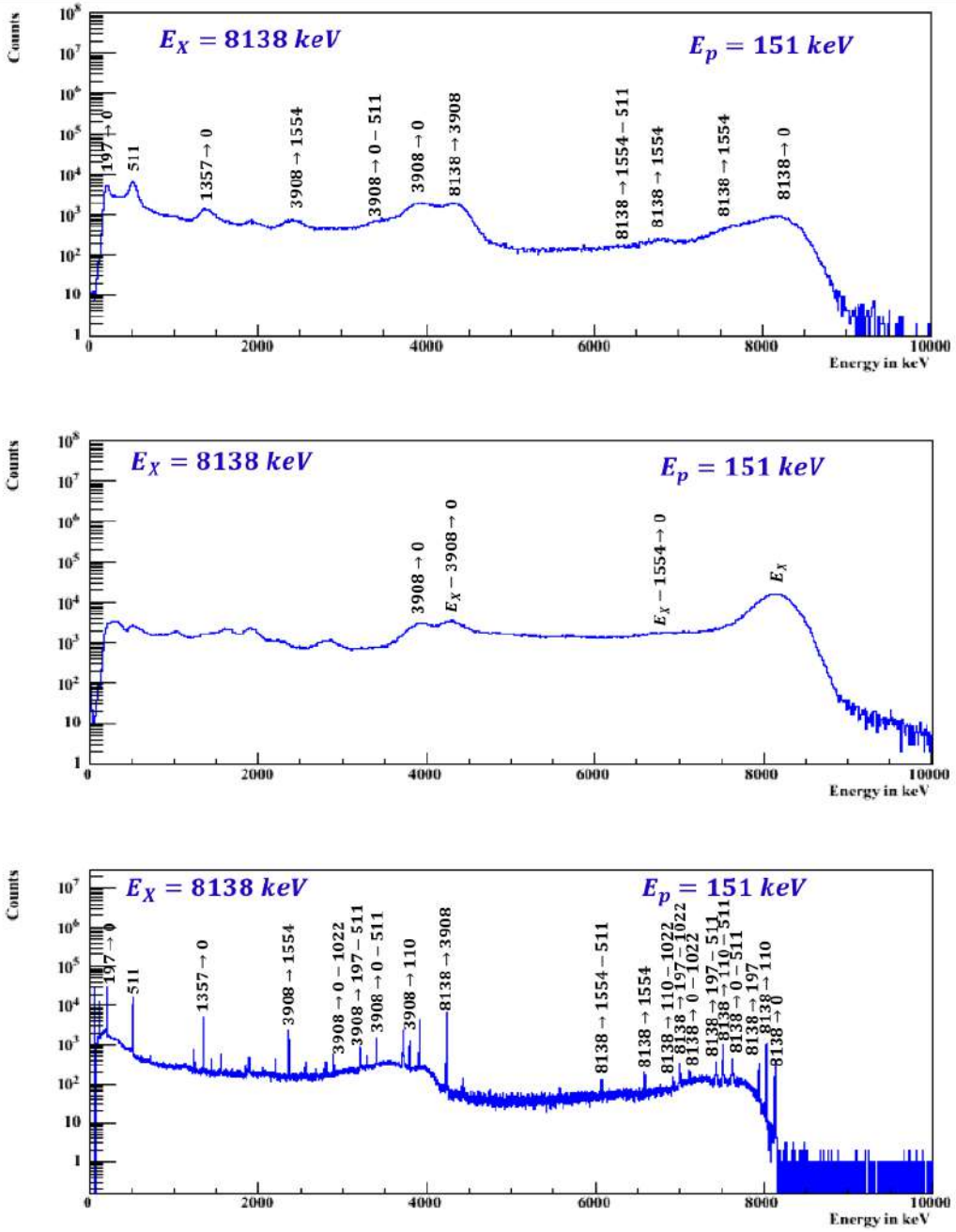

Figure 2.15: Experimental gamma spectra at the resonance energy $E_p = 151keV$ corresponding to the state $E_X = 8138keV$ of the ^{19}F, acquired with the single BGO segment (on the top), with the sum of the six segments (on the center), with the HPGe detector (bottom).

Chapter 3

The ^{18}O(p, γ)^{19}F experiment: calibrations and measurements

In order to retrieve all useful experimental evidence from the BGO and HPGe detectors, calibration runs were performed before the beginning of the data production phase and regularly during the experiment. The fundamental calibrations needed deal with energy and efficiency. In particular, the latter deserves a very careful approach in HPGe due to high energy resolution strong dependence on gamma energy.

3.1 Energy calibration

Several energy calibrations for different periods of measurement during data taking, are obtained by using $\gamma-$rays that have been previously studied, and are thus well known. ^{137}Cs, ^{60}Co calibrated sources, and radiative capture reactions as $^{14}N(p,\gamma)^{15}O$, $^{27}Al(p,\gamma)^{28}Si$, acquired at various laboratory proton resonance energies (278 keV for the first one, 231 keV and 309 keV for the second one) in order to cover the γ energy range of interest 600-12000 keV. A linear relationship between the energy of an incident $\gamma-$ray on the detector, and the pulse amplitudes is set E= a*Ch(E) + b, where Ch(E) is the the position of the peak in the spectrum.
The BGO energy calibration was performed both for the six single spectra, and the sum spectrum.
Regarding the HPGe energy calibration data were collected around the strongest energy resonance of $^{18}O(p,\gamma)^{19}F$ reaction at the laboratory energy of 151 keV in order to extend the range until the lowest $\gamma-$energies (100 keV).
Two calibration curves were obtained (see Fig. 3.1, 3.2), for two periods of measurement.

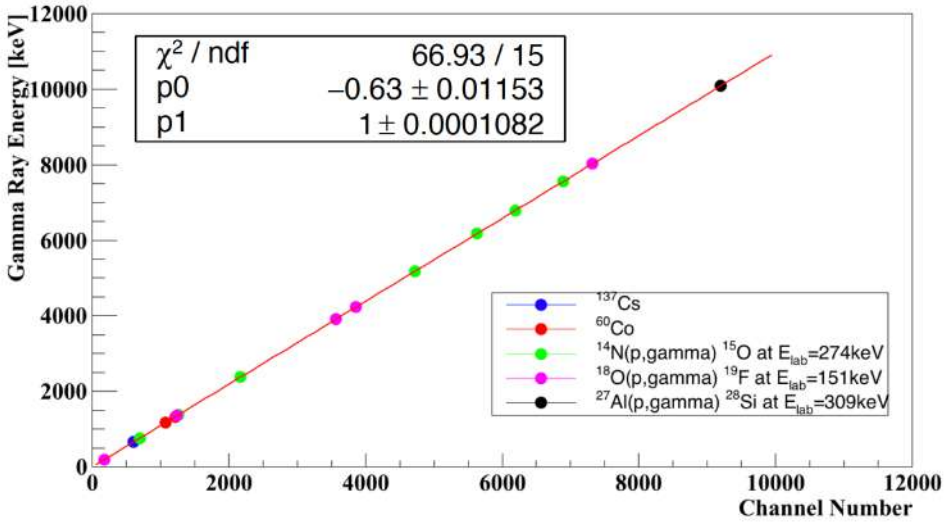

Figure 3.1: Calibration curve for the first data taking period, incorporating the γ-rays from ^{137}Cs, ^{60}Co calibrated sources, $^{14}N(p,\gamma)^{15}O$, $^{27}Al(p,\gamma)^{28}Si$, $^{18}O(p,\gamma)^{19}F$ reactions, acquired at 278 keV, 309 keV and 151 keV proton resonance energies, respectively.

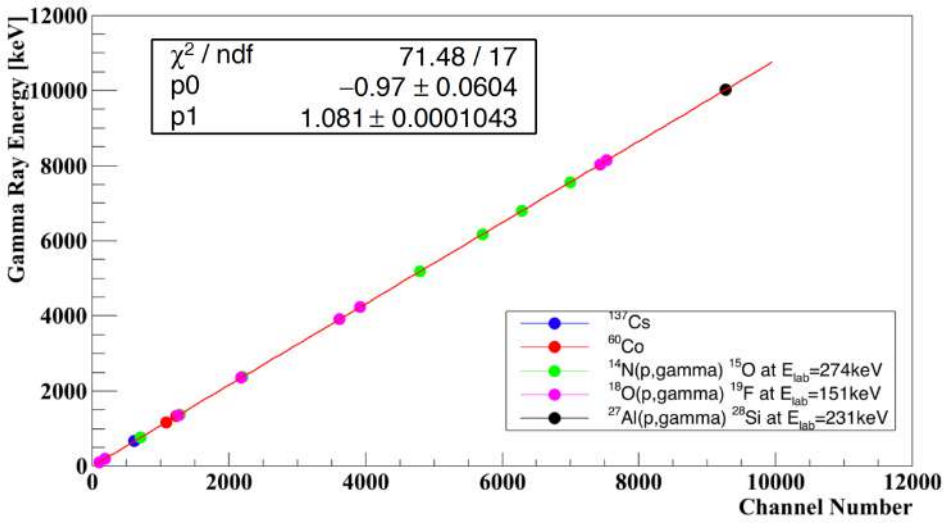

Figure 3.2: Calibration curve for the second data taking period incorporating the γ-rays from ^{137}Cs, ^{60}Co calibrated sources, $^{14}N(p,\gamma)^{15}O$, $^{27}Al(p,\gamma)^{28}Si$, $^{18}O(p,\gamma)^{19}F$ reactions, acquired at 278 keV, 231 keV and 151 keV proton resonance energies, respectively.

3.2 4π BGO detection resolution and efficiency at 8 MeV

The detection efficiency of the 4π BGO detector was estimated at the Q-value of the reaction 8 MeV under investigation, analysing γ-ray sum spectra (Fig. 3.3).
Two gaussian fits were performed, one around 8 MeV, using the spectrum acquired at the well known 151 keV energy resonance of $^{18}O(p,\gamma)^{19}F$ (Fig. 3.3, upper spectrum), and another around 2 MeV (Fig. 3.4), using the spectrum acquired at the known 328 keV resonance of $^{27}Al(p,\gamma)^{28}Si$. The resulting σ values 0.222 ± 0.002 MeV and 0.114 ± 0.004 MeV, where then used to determine a $\sqrt{E}$ dependent energy resolution $\sigma = s_0 + s_1\sqrt{E}$ [54]. The s_0 and s_1 parameters were determined as the solution of a linear system of equations with

$$\begin{cases} \sigma_0 = s_0 + s_1\sqrt{E_0} \\ \sigma_1 = s_0 + s_1\sqrt{E_1} \end{cases} \tag{3.1}$$

which resulted in $s_0 = 0.004$ and $s_1 = 0.077$.

Six "perfect" simulated spectra were obtained from LUNA Monte Carlo simulation written in Geant 4 [55].
Then an energy smearing was applied using the estimated values of s_0 and s_1 as input, summing spectra event by event in order to obtain the simulated sum spectrum at the 151 keV proton energy.
The simulated spectrum was validated at 8 MeV by comparing (Fig. 3.3) with the experimental one.

The detection efficiency was then calculated from simulated sum spectrum dividing the entries contained in the peak, by the total entries in the spectrum [40].
The procedure was repeated in correspondence of other resonances of the $^{18}O(p,\gamma)^{19}F$ reaction and the detection efficiencies result fairly comparable (Table 3.1).

Table 3.1: Detection efficiencies for the $^{18}O(p,\gamma)^{19}F$ resonance energies.

E_p(keV)	Detection efficiencies
151	40%
216	38%
274	37%
334	37%

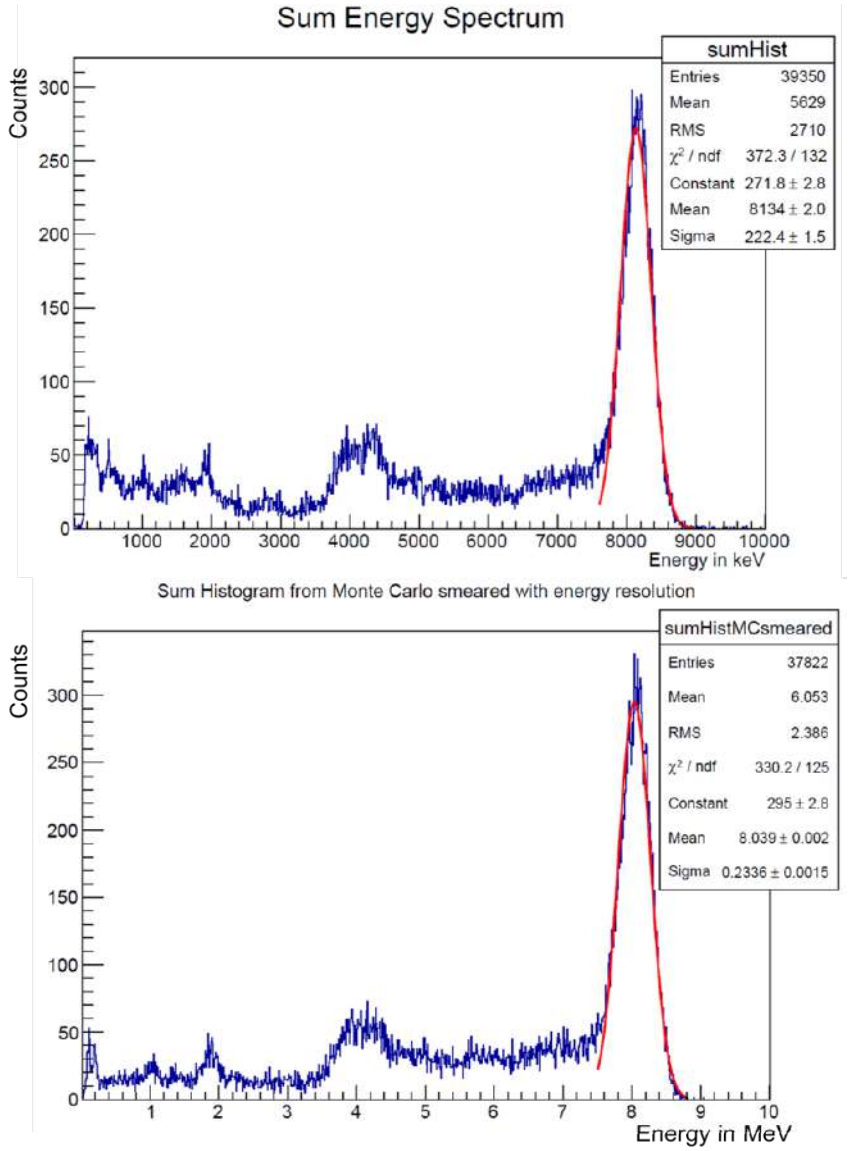

Figure 3.3: Experimental spectrum (on the top), simulated spectrum (at the bottom), both performed 151 keV resonance, including a gaussian fit in order to obtain the σ-value.

3.3 Sources and reactions used for HPGe efficiency calibration

Multiple calibration peaks at various points along the measured energy range are mandatory in order to have an efficiency calibration, since the HPGe efficiency variation with energy is very fast. The features of the calibrated sources and known reactions used here to obtain an accurate efficiency cali-

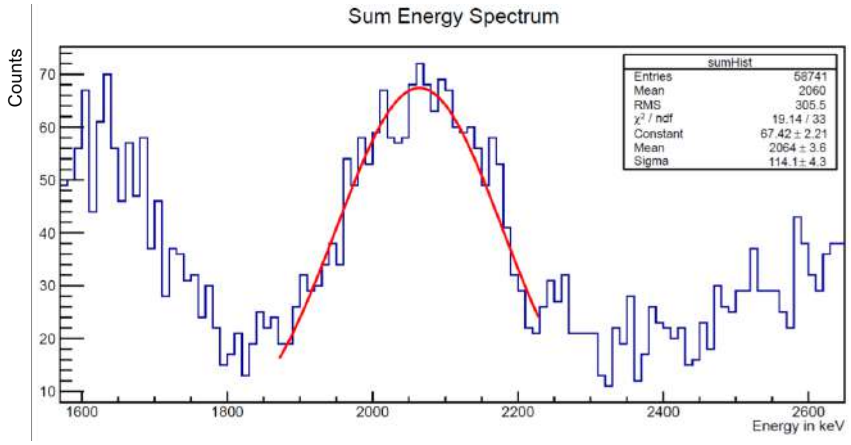

Figure 3.4: A gaussian fit of a peak around 2 MeV coming from the experimental spectrum of $^{27}Al(p,\gamma)^{28}Si$ reaction, acquired at 328 keV energy resonance, is implemented in order to obtain the σ-value.

bration are reported in the present section.

An efficiency calibration for the HPGe detector was obtained by data taking with well known γ-rays including radioactive sources (^{137}Cs and ^{60}Co), and radiative capture reactions as $^{14}N(p,\gamma)^{15}O$, $^{27}Al(p,\gamma)^{28}Si$, performed at 278 keV and 231 keV proton resonance energies, respectively, in order to cover the γ energy range 661-12000 keV, useful for the measurements of the reaction of interest, for which it would be necessary to include two additional efficiency values at 110 keV and 197 keV too. $^{18}O(p,\gamma)^{19}F$ data from the 151 keV resonance spectra were used for this aim. ^{137}Cs is characterized by a single line, as shown in the experimental spectrum (Fig. 3.5). It decays β with the major probability to the 662 keV excited state in ^{56}Ba. This level decays to the ground state, releasing a 662 keV γ-ray, as from the decay scheme in Fig. 3.6.

^{60}Co is characterized by a cascade of two gammas. It decays β with the major probability to the 2.505 MeV excited state in ^{60}Ni. This level quickly decays to the 1.332 MeV level, releasing a 1.173 MeV γ_1-ray, then this intermediate level decays to the ground state releasing a 1.332 MeV γ_2-ray. The level scheme and the experimental spectrum are illustrated in Fig. 3.7, 3.8, respectively.

^{15}O compound nucleus at the energy of 274 keV resonance is characterized by 6 γ-peaks belonging to three cascades, each of two gammas and the peak at 7556 keV, the latter referring to the direct ground state transition or to the summing-in effects contributions (Fig. 3.9, 3.10).

^{28}Si compound nucleus at 231 keV resonance decays γ to the 1779 MeV excited state with a probability of 100%, releasing a 10020 keV γ_1-ray, then this intermediate level decays to the ground state with a probability of 100%,

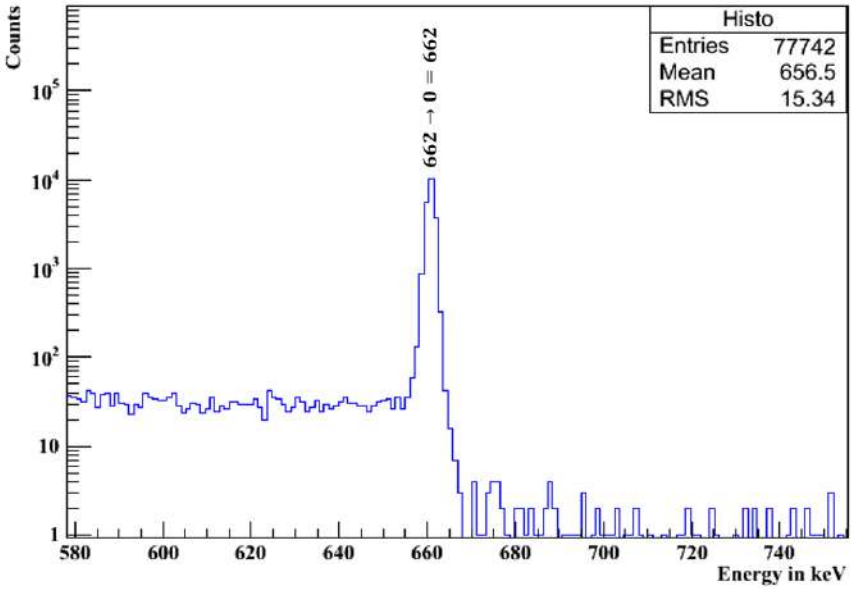

Figure 3.5: Experimental spectrum of ^{137}Cs.

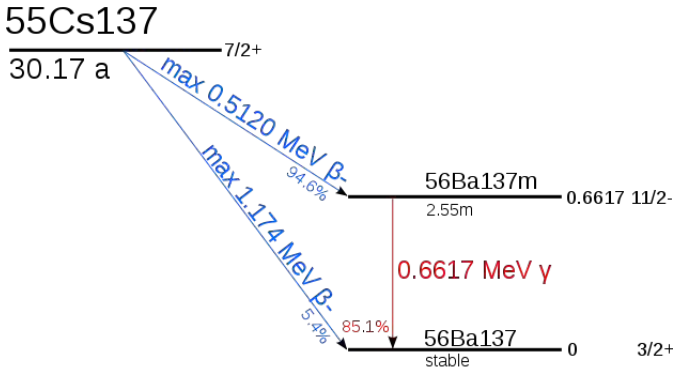

Figure 3.6: Decay scheme of ^{137}Cs.

releasing a 1779 keV γ_2-ray (Fig. 3.11). The experimental spectrum is illustrated in Fig.3.12.

The spectra analysis for calibration is often affected by sources of uncertainty such as close resonances interference. As an example of how these situations have been treated in the present work, let us consider the $^{27}Al(p,\gamma)^{28}Si$ reaction [57] starting from the excitation of level 11799 keV.

The peak at 10020 keV is close to another peak at 9999.9 keV, that has its origin in another resonance of the $^{27}Al(p,\gamma)^{28}Si$ reaction at 210 keV proton energy (Fig.3.13). Following [58], starting from the level (11780.7 keV) of the proton energy resonance at 210 keV, the ^{28}Si decays γ to the 1779 MeV

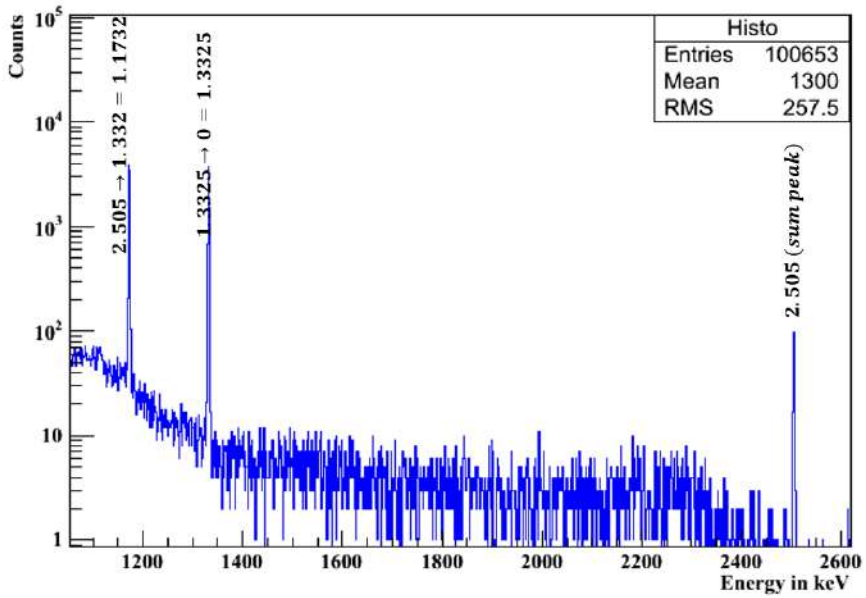

Figure 3.7: Experimental spectrum of ^{60}Co.

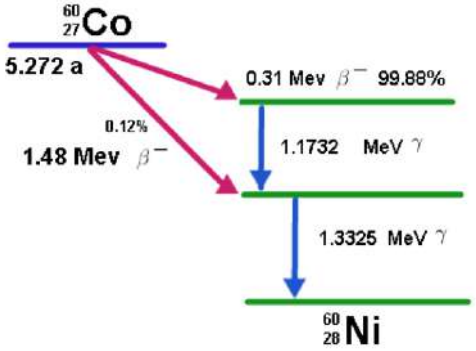

Figure 3.8: Decay scheme of ^{60}Co.

excited state with a probability of 100%, releasing a 9999.9 keV γ_1-ray, then this intermediate level decays to the ground state with a probability of 100%, releasing a 1779 keV γ_2-ray (Fig. 3.14).
The spectral peak at 1779 keV contains then the contributions coming from $\gamma-$rays of the two competing resonances. If a is the ratio of the resonance E= 210 keV to the resonance E=231 keV, the total counts measured under the 1779 keV peak are:

$$\begin{aligned} N_{1779} = N_{231} + N_{210} = N_{231} + a \cdot N_{231} = \\ = (1+a) \cdot N_{231} \rightarrow N_{231} = \frac{N_{1779}}{1+a} \end{aligned} \tag{3.2}$$

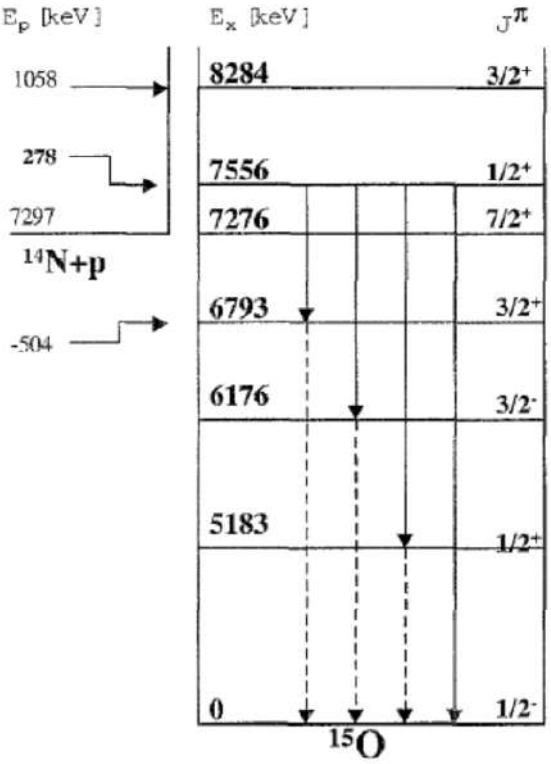

Figure 3.9: Level structure of ^{15}O near the proton threshold [56].

where N_{210} and N_{231} are the counts due to individual contributions.
If the a ratio is calculated from the literature resonance strength values [59] $\omega\gamma = 2\epsilon(E_{res})Y/\lambda^2$ with proper unit substitution [14] of M_0, M_1, projectile and target masses, and E_{res}^{lab} laboratory resonance energy

$$\frac{\lambda^2}{2} = (\frac{M_0 + M_1}{M_1})^2 \cdot \frac{4.125 \cdot 10^{-18}}{M_0 E_{res}^{lab}}(cm^2). \tag{3.3}$$

The *ratio* ratio can be estimated from:

$$\frac{\omega\gamma_{210}}{\omega\gamma_{231}} = \frac{\frac{2N_{210}}{\lambda_{210}^2}}{\frac{2N_{231}}{\lambda_{231}^2}} = \frac{\frac{1}{E_{231}}}{\frac{1}{E_{210}}}\frac{N_{210}}{N_{231}} \rightarrow \frac{N_{210}}{N_{231}} = a \cdot \frac{E_{210}}{E_{231}} \tag{3.4}$$

with the assumption that the $\epsilon(E_{res})$ is the same for both energy resonances. Since the two a ratios estimates are compatible, we consider it a consistent correction to the true N_{231} counts.

3.4 HPGe detection efficiency

In γ spectrometry with HPGe detectors the detection efficiency estimation is very complex due to true summing effects to be taken in account espe-

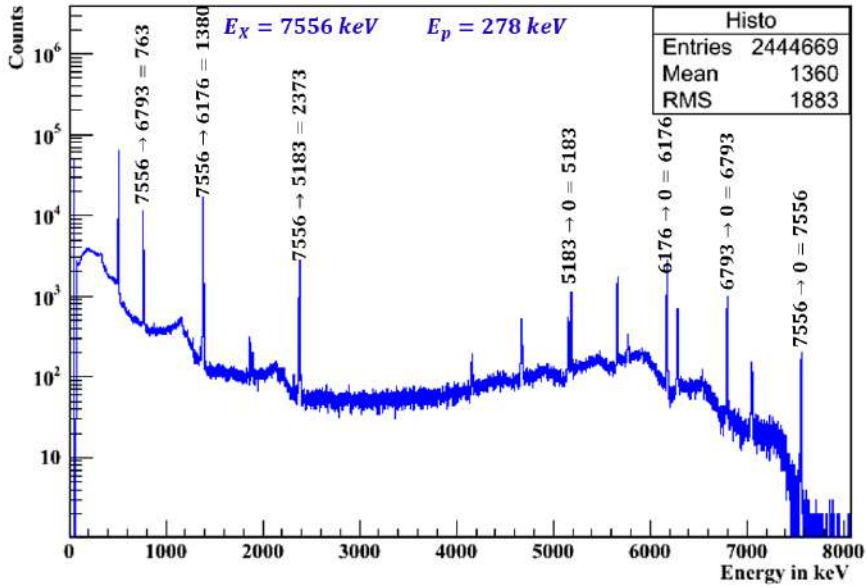

Figure 3.10: Experimental spectrum acquired at 278 keV, the proton energy resonance of $^{14}N(p,\gamma)^{15}O$ reaction. The primaries and the secondary $\gamma-rays$ are identified.

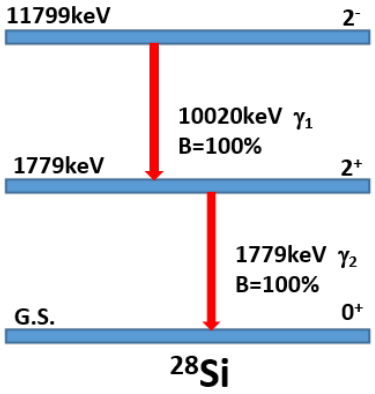

Figure 3.11: Level structure of ^{28}Si starting from the level at 11799 keV.

cially when working in low source-detector distance [60]. The complexity of the necessary coincidence summing corrections increases with the number of levels in the decay scheme of the measured radionuclide [60]. The detection efficiency estimation therefore deserves attention to details.

In the present work, the calibration measurements were performed on different detector distances. The closest distance, which was used for most

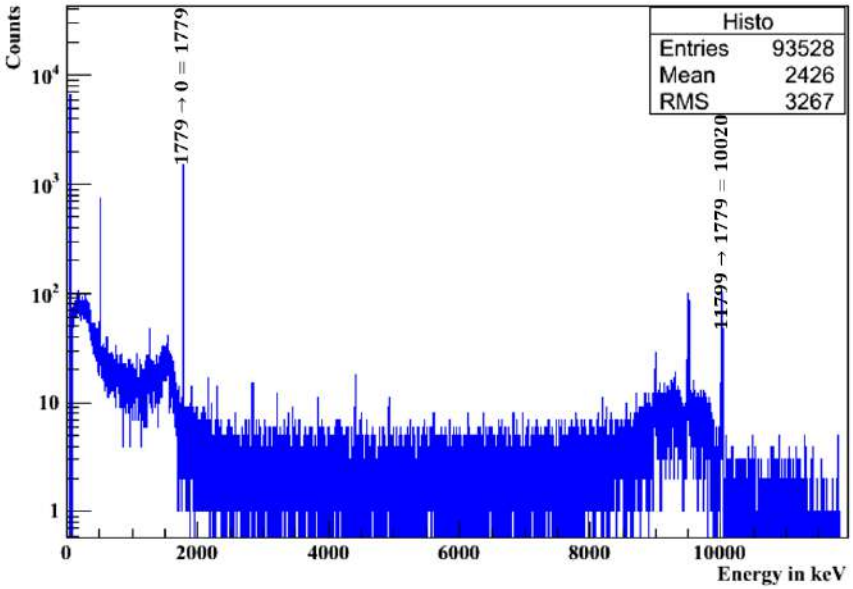

Figure 3.12: Experimental spectrum acquired at 231 keV, the proton energy resonance of $^{27}Al(p,\gamma)^{28}Si$ reaction. The primary and the secondary $\gamma-rays$ are identified.

measurements with ^{18}O target, is referred to as d=0 cm position, the other distances (measured along the rails in the detector setup) were d= 5, 10, 15, 20 cm.

As customary in literature [61] and practice of $\gamma-$ray detection [54], the full energy peak efficiency η_{calc}^{FEP} and the total efficiency η_{calc}^{TOT} are empirically parametrized as a function of energy.
Then the parameters are best fit to the experiment by comparing the expected counts to the measured ones in a series of calibration spectral peaks.
The total efficiency of detecting a γ with energy E_γ is just the probability that the $\gamma-$ray will interact with the detector and deposit some energy. The full energy peak efficiency is instead the probability that the full energy of the incident $\gamma-$ray will be deposited in the detector. The full energy peak efficiency is generally orders of magnitude lower than the total efficiency. Both types of detector efficiency depend on the source-detector geometry, and so there is no general formula for either.

In order to set the scale of the total and full energy peak efficiencies, two measured values: η_{exp}^{TOT} and η_{exp}^{FEP}, respectively of a single line source as ^{137}Cs were used, that are not affected by summing effects.
Instead, two kinds of summing problems in the presence of γ cascades have to be corrected: summing-in and summing-out. Summing-in results when

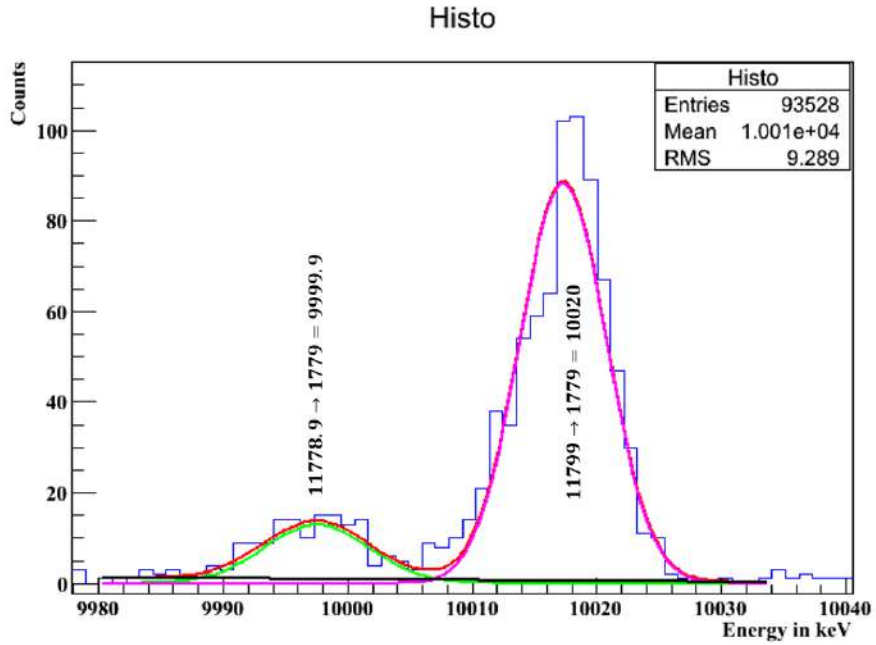

Figure 3.13: 231 keV energy resonance of $^{27}Al(p,\gamma)^{28}Si$ reaction. Gaussian deconvolution including linear background spectrum subtraction between primary peaks at 10020 keV and 9999.9 keV of the 231 keV and the 210 keV resonances, respectively.

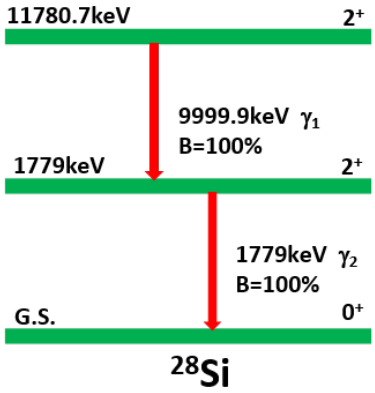

Figure 3.14: Level structure of ^{28}Si starting from the level at 11780.7 keV.

two consecutive-rays (say, 1 and 2) in a cascade produce a response in the detector at $E_0 = E_1 + E_2$. So the peak at E_0 will not represent the true number of gamma rays of energy E_0 detected. The efficiency, consequently, will appear artificially high. A similar situation holds for the summing-out effect, the full energy of one $\gamma-$ray in a cascade plus the partial energy of

another $\gamma-$ray are summed together, producing a count in some other channel which corresponds to neither $\gamma-$ray. Therefore each peak in the spectrum loses a real count. In this case, the efficiency for each of these $\gamma-$rays will appear artificially low.

In reference to the case of ^{137}Cs, the η_{exp}^{TOT} and the η_{exp}^{FEP} are:

$$\eta_{exp}^{TOT}(E_\gamma) = \frac{N_{exp}^{TOT}}{At} \tag{3.5}$$

$$\eta_{exp}^{FEP}(E_\gamma) = \frac{N_{exp}^{FEP}}{AtB} \tag{3.6}$$

where: N_{exp}^{TOT}, N_{exp}^{FEP} are the total and the full energy peak entries in the spectrum, respectively, A is the activity of the calibrated source, B is the branching ratio and t is the live time of the measurement.

Apart from the ^{137}Cs calibrated source case, the ^{60}Co calibrated source and the $^{14}N(p,\gamma)^{15}O$ and $^{27}Al(p,\gamma)^{28}Si$ reactions have more gammas in the experimental spectra, due to cascades.

In the general case in which a point-source activity of a radionuclide or a compound nucleus of a thermonuclear reaction has a complex level scheme allowing $\gamma-$cascades, the probability P_E that one count is detected in the full energy peak at an energy E during one decay event of the parent nucleus may be written [62], [63].

$$P_E = \sum_{Cascades\ C} P_C[\prod_{i=1}^{M_C}(B_k\eta_{calc_k}^{FEP} \prod_{m=M_C+1}^{N_C}(1 - B_m\eta_{calc_m}^{TOT})] \tag{3.7}$$

where: P_C is the probability of a specific cascade C with N_C level transitions, i. e., the product of the level feeding probability of the highest level and the branching ratios of the following level transitions down to the ground level. B_k and B_m are the γ branching ratios. $\eta_{calc_k}^{FEP}$ and $\eta_{calc_m}^{TOT}$ are the full energy and the total efficiencies, respectively. The first product in Eq.(3.7) describes the contribution to the $\gamma-$peak at energy E from coincident transitions k each emitting a $\gamma-$photon such that $E = \sum_{k=1}^{M_C} E_k$: "summing-in" effect. The second product describes counting rate losses caused by those $\gamma-$emissions (number $N_C - M_C$) that do not contribute to the full-energy peak at E: "summing-out" effect.

In case of calibrated sources, Eq. (3.7) was multiplied by the source activity A and the measurement live time and it yields the counts expected for the $\gamma-$peak at energy E.
Similarly, in the case of thermonuclear reactions, the same result is obtained multiplying Eq. (3.7) by the total number of induced reactions.

The total number of induced reactions was calculated, from the experimental Yield:

$$Yield = \frac{N_R}{N_b \frac{t}{t'}} \tag{3.8}$$

where N_R is the total number of reactions, N_b is the total number of incident projectiles, t and t', are the live and the real time of measurement, respectively, to take in account the dead time corrections.
Considering, for example, calibration reaction $^{14}N(p,\gamma)^{15}O$ at 278 keV [61], the Yield was calculated from the resonance strength, and the total number of reactions is:

$$N_R = Yield \cdot N_b \frac{t}{t'} \tag{3.9}$$

Consequently, the reaction rate is:

$$R = Yield \cdot N_b \frac{1}{t'} \tag{3.10}$$

The R value will there play the same role of the activity A when the efficiency determination incorporates both data from calibration source and (p, γ) reactions.
The efficiency was parametrized [61] as:

$$\eta^{FEP}(d, E_\gamma) = f(d, E_\gamma) \cdot \exp\left(a + b\ln(E_\gamma) + c\ln\left(E_\gamma\right)^2\right) \tag{3.11}$$

$$\eta^{TOT}(d, E_\gamma) = \frac{\eta^{FEP}(d, E_\gamma)}{\exp\left(k_1 + k_2\ln(E_\gamma) + k_3\ln\left(E_\gamma\right)^2\right)} \tag{3.12}$$

$$f(d, E_\gamma) = \frac{1 - \exp(\frac{d+d_0}{a_0 + b_0\sqrt{E_\gamma}})}{(d+d_0)^2} \tag{3.13}$$

where a, b, c, k_1, k_2, k_3, d_0, b_0 are used as fitting parameters The function $f(d, E_\gamma)$ models the distance dependence. A number of levels rank equal to three has been considered in the decay schemes of ^{60}Co radionuclide, ^{15}O and ^{28}Si compound nuclei, so the coincidence summing corrections result simplified.

Summing corrections in this simple case of a two gammas cascade are accounted from Eq.(3.14):

$$\begin{aligned} n^{FEP}_{calc}(E_{\gamma_1}) &= AtB_{\gamma_1}B_{\gamma_2}\eta^{FEP}_{calc}(E_{\gamma_1})(1 - B_{\gamma_2}\eta^{TOT}_{calc}(E_{\gamma_2})) \\ n^{FEP}_{calc}(E_{\gamma_2}) &= AtB_{\gamma_1}B_{\gamma_2}\eta^{FEP}_{calc}(E_{\gamma_2})(1 - B_{\gamma_1}\eta^{TOT}_{calc}(E_{\gamma_1})) \\ n_{sum}(E_{\gamma_1} + E_{\gamma_2}) &= AtB_{\gamma_1}B_{\gamma_2}\eta^{FEP}_{calc}(E_{\gamma_1})\eta^{FEP}_{calc}(E_{\gamma_2}) \end{aligned} \tag{3.14}$$

A χ^2 was defined including all data depending on the detector distances, in order to obtain the total and the full energy peak efficiencies covering the whole energy range of interest:

$$\chi^2_{FEP} = \sum_{i=1}^{n} \left(\frac{n^{FEP}_{calc}(E_{\gamma_i}) - n^{FEP}_{exp}(E_{\gamma_i})}{\sigma(n^{FEP}_{exp}(E_{\gamma_i}))}\right)^2 \tag{3.15}$$

The χ^2 minimization procedure resulted in the estimation of η^{FEP} over the range of energy (Fig.3.15). In case of the (p,γ) reactions R is used as fitting parameter. The statistical uncertainties associated to the full energy peak

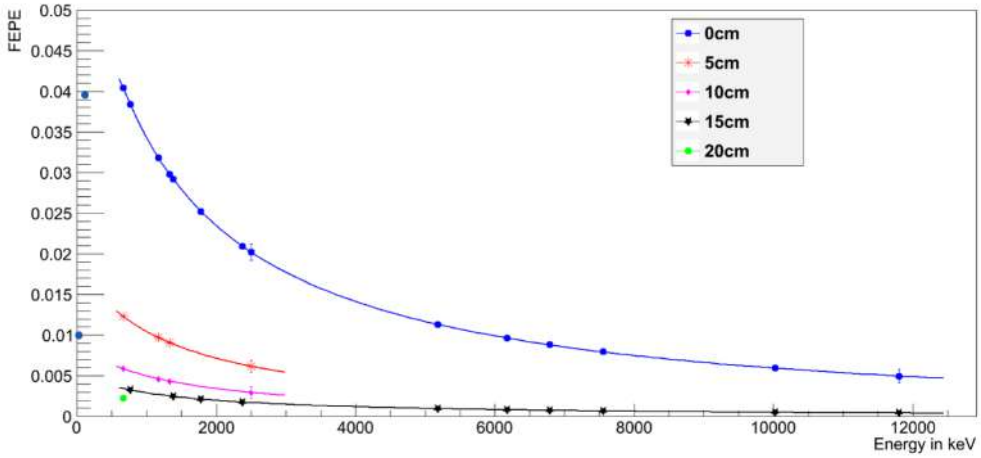

Figure 3.15: Results of the empirical efficiency calibration. Full energy peak efficiency for a single gamma as a function of energy for the different energies, depending on the detector distances.

efficiency were calculated from the properties of the binomial distribution, following [64]:

$$\sigma_{\eta^{FEP}_{calc}} = \sqrt{\frac{\eta^{FEP}_{calc}(1 - \eta^{FEP}_{calc})}{N}} \tag{3.16}$$

where $N = \frac{n^{FEP}_{exp}}{\eta^{FEP}_{calc}}$ is the number of emitted gammas, calculated for each full energy peak.

To obtain the total and full energy peak efficiencies at 110 keV and 197 keV, it was tried to simply extend the parametrized efficiency curves that were previously used to fit the efficiencies (with the parameters a, b, c, k_1, k_2, k_3, d_0, b_0, etc.). However, these two points are in the part of the curve where the efficiency changes very quickly, and to model this in the curve, it was necessary to add many more parameters (to increase the orders of the polynomials), which is not reasonable when there are only two additional

points, and not needed if it is not required to interpolate the efficiency at other energies between 110 keV and 197 keV. Four new parameters were added to the fit, namely the total and full energy efficiencies at the 110 keV and 197 keV, including data from the 151 keV resonance spectra [65].

3.5 Target behaviour under beam bombardment

The high beam currents (up to 300 μA on target) used in present experiment caused some target deterioration due to *sputtering*, which induces a progressive reduction of the effective target thickness and consequently a change in the reaction yield plateau [14]. For this reason the target was replaced several times during the data taking when degradation resulted on it.
The target thickness and homogeneity were monitored by the measured yield profile around the energy of the strong and narrow resonance $E_{Rlab} = 151$ keV of the $^{18}O(p,\gamma)^{19}F$ reaction, performed regularly every few tens of Coulomb of accumulated charge.

As reported in section 1.4, the cross section for resonant reactions is described by the Breit-Wigner formalism.
Combining Eq. (1.13) and (1.18), the measured yield can be expressed [14] in terms of the resonance strength, $\omega\gamma$, target thickness, Δ and beam energy E_0, as:

$$\begin{aligned} Y(E_0) = \int_{E_0-\Delta}^{E_0} \frac{1}{\epsilon(E)}\sigma_{BW}(E) = \\ \frac{\lambda^2}{2\pi}\frac{\omega\gamma}{\epsilon(E)}\frac{\Gamma}{2}[arctan(\frac{E_0 - E_R}{\frac{\Gamma}{2}}) - arctan(\frac{E_0 - E_R - \Delta}{\frac{\Gamma}{2}})] \end{aligned} \tag{3.17}$$

where $\omega = \frac{(2J+1)(1+\delta_{XA})}{(2j_A+1)(2j_x+1)}$ and $\gamma = \frac{\Gamma_{entrance}\Gamma_{exit}}{\Gamma}$. The De Broglie wavelength, λ, the stopping power $\epsilon(E)$, are evaluated at an effective energy, which for a narrow resonance is equivalent to the resonance energy, E_R.

In the specific case of solid Ta_2O_5 targets with an isotopic enrichment in ^{18}O of 99%, the Eq. (1.21) for the stopping power becomes [14], [66]:

$$\epsilon_{eff} = \frac{M_{^{18}O}}{M_p + M_{^{18}O}}(\frac{N_O}{N_{^{18}O}}\epsilon_{^{18}O} + \frac{N_{Ta}}{N_{^{18}O}}\epsilon_{Ta}) \tag{3.18}$$

where $M_{^{18}O}$, M_p are the masses of ^{18}O atom and of the proton respectively, $\epsilon_{^{18}O}$, ϵ_{Ta} are the laboratory stopping powers of protons in units of $eVcm^2/atom$, calculated with the code SRIM 2013 [67], N_i are number densities ($N_O = N_{^{16}O} + N_{^{17}O} + N_{^{18}O}$). The stopping power values were calculated

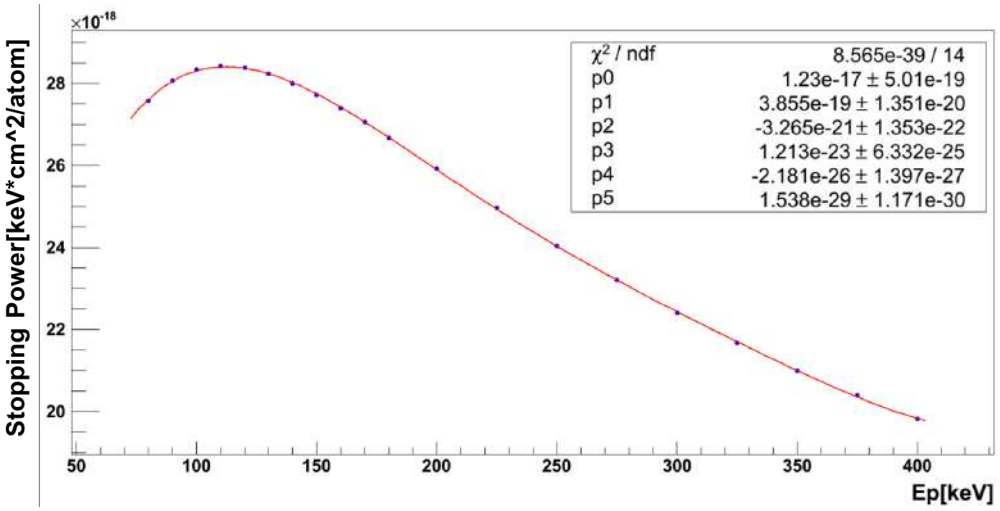

Figure 3.16: Effective stopping power for protons incident on a solid Ta_2O_5 target 99% enriched in ^{18}O (active nuclei).

in the energetic range 90-400 keV and interpolated with a polynomial function (Fig. 3.16). The assumed ϵ_{eff}:

$$\epsilon_{eff}(E) = 1.538 \cdot 10^{-29}E^5 - 2.181 \cdot 10^{-26}E^4 + 1.213 \cdot 10^{-23}E^3 - \\ -3.265 \cdot 10^{-21}E^2 + 3.855 \cdot 10^{-19}E + 1.23 \cdot 10^{-17} \tag{3.19}$$

allows to obtain the stopping power values at the energy of interest.

Eq.(4.2) is defined for a mono-energetic beam and does not account for energy straggling effects inside the target medium. Experimentally the Yield profile is parameterized with an Eq. similar to (4.2):

$$Y(E_0) = A[arctan(\frac{E_0 - E_R}{B}) - arctan(\frac{E_0 - E_R - \Delta E}{C})] \tag{3.20}$$

where the parameters A, B, C, E_R, Δ have been freely varied in a fit for a χ^2 minimization. In real conditions the ^{18}O target have not a step discontinuity on the interface oxygen-tantalum, but reasonably a transition region of thickness not negligible will be present, in which the active atoms density will move from a maximum value to zero.
The order of magnitude of the straggling effects and the beam energy dispersion are $\Delta_{stragg} < 1.5$ keV [68], [69], [70] and $\Delta_{enDisp} < 300$ eV at LUNA [10], respectively.
A complete scan of the target profile was measured at 151 keV resonance energy of $^{18}O(p,\gamma)^{19}F$ reaction in two different approaches during the two phases of measurement (Fig. 3.17). The energy scan is performed by measuring the yield of increasing energies starting from a value just below the resonance on it. The resonance energy, E_R, is the mid-point (half-maximum)

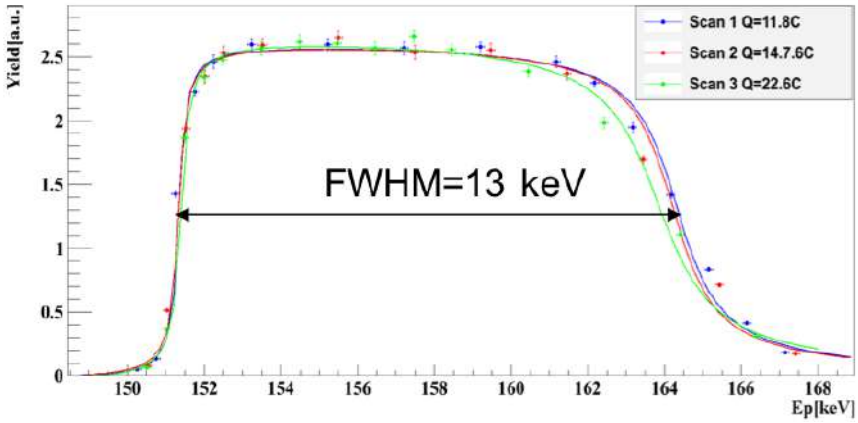

Figure 3.17: ^{18}O target scan around 151keV beam energy resonance.

of the rising edge of the yield curve. From the scan profile it is evident that in the scan 3 the thickness of the target decreases because it begins to be degraded. At this point it is necessary to replace the target in order to start the new data taking.
During the BGO phase, the target scan was measured, focusing the analysis on the sum spectra around the ROI approximately equal to the excited level at 8138 keV, while during the HPGe phase, on the γ line at 197 keV belonging to cascades of the 151 keV resonance.

Chapter 4

The ^{18}O(p, γ)^{19}F experiment: data reduction, analysis and results

In the present chapter, the data analysis procedure is detailed for data sets from both BGO and HPGe measurements. The objectives of the data analysis are the estimates of all resonance strengths and possible low-energy resonant behaviour of the cross section (with BGO) and the estimates of primary γ ray branching ratios values and resonance strengths (with HPGe). Results of the analysis will be illustrated along the discussion.

4.1 BGO data analysis

The BGO phase of measurements covered the proton energy range 89-400 keV. With reference to previous experimental [5] and theoretical [6] works, measurements were performed in order to explore a possible weak resonant strength at $E_{res} = 95 \pm 3$ keV in the low-energy region of the excitation function, thanks to the high efficiency of the BGO summing crystal detector [48]. In addition measurements on the 151 keV, 216 keV, 274 keV and 334 keV resonance strengths were performed to improve previously known values.
The data analysis focused the attention on two ranges of measurement, the low energy range 89-140 keV below the strong 151 keV resonance and the higher energy one 140-400 keV.
The six crystals 4π BGO detector presents a clear signal at the energy of the reaction Q-value plus the centre of mass energy of the entrance channel. Thanks to the integrating summing effects, this maximum energy peak corresponds to the total absorption of all γ ray cascades from the reaction. On the contrary, the signal coming from the single crystal at the same energy is weaker, because it covers only one sixth of the solid angle of the 4π BGO

detector around the target and resolves only the strong transitions. The analysis of the single spectrum may provide information about the identification of the single γ in a cascade, although the energy resolution of the detector is limited. The spectrum enhancement owing to the integration over the solid angle are shown for the example of a simple two γ cascade in Fig. 4.1 [48]. The advantage of a 4π geometry is especially evident in those reactions char-

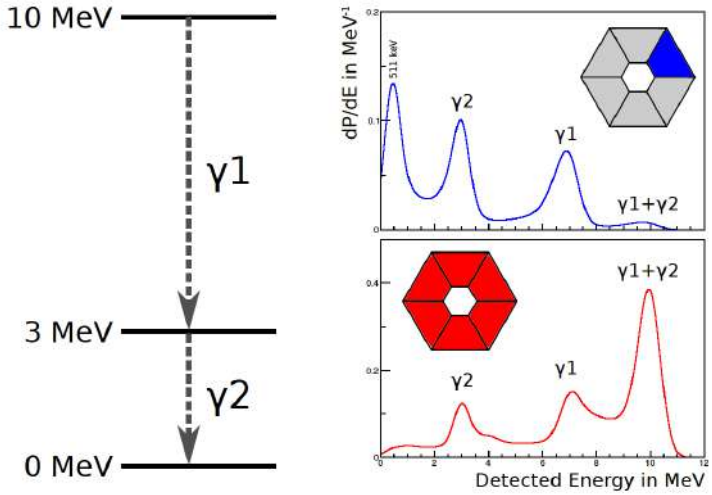

Figure 4.1: Single and sum spectra for a cascade of two γ rays, isotropically emitted without angular correlation [48].

acterized by large Q values, where the region of interest is located at energies higher than most environmental and beam induced backgrounds. The BGO data analysis is focused around the energy of the level of the compound nucleus excited by resonant or direct mechanism. In the case of the present studied reaction, the region of interest in the sum spectrum is the peak at an energy around 8 MeV, as illustrated in Fig. 4.2 for a measurement performed at a proton energy equal to 151 keV.
A gaussian fit including a linear background subtraction was implemented, (Fig. 4.3), and the peak counts were estimated from the area under the background subtracted gaussian curve. A statistical and fit uncertainty was associated to the counts in the peak, by propagating the uncertainties on fit parameters. The experimental reaction Yield was then estimated in arbitrary units from the ratio Eq. (4.1) between the peak area and the charge Q in μC accumulated in the Faraday cup during the run live time.

$$Y = \frac{Counts}{Q} \tag{4.1}$$

The excitation function, i.e. the collection of yield values at several energies, thus estimated in the energy range explored is illustrated in Fig. 4.4. The

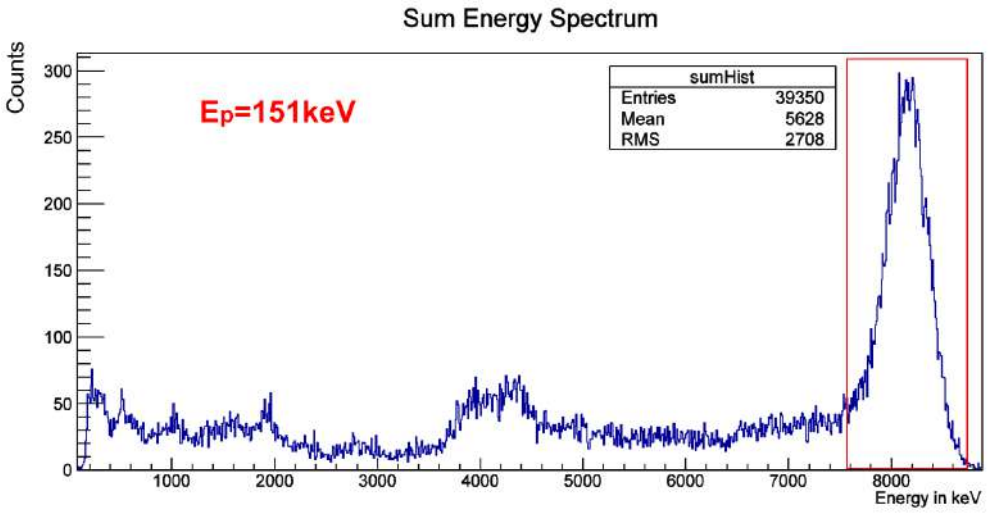

Figure 4.2: Experimental sum spectrum acquired at 151 keV. The peak at an energy around 8 MeV is the region of interest for the formation of the compound nucleus.

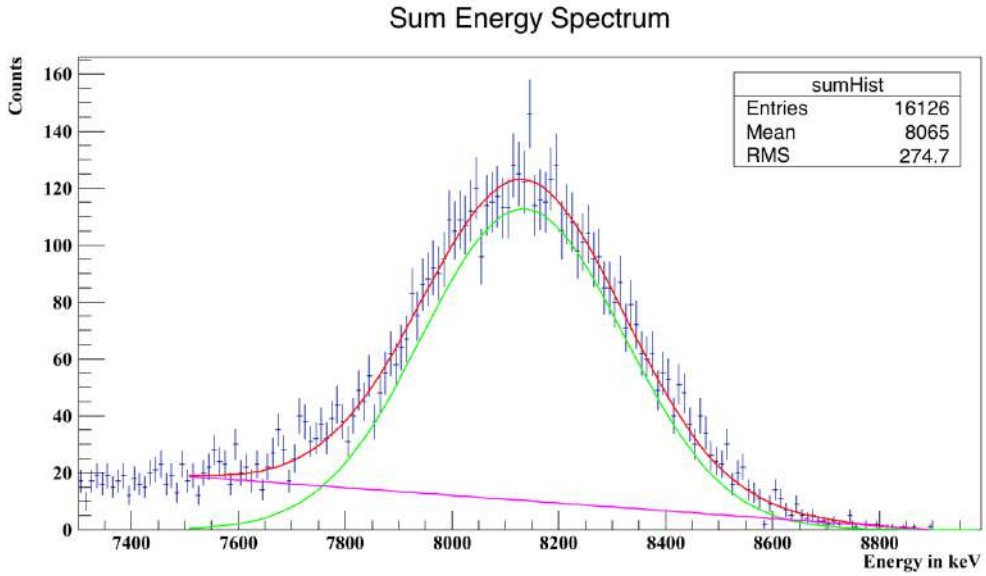

Figure 4.3: Example of gaussian fit including linear background subtraction.

statistical uncertainties associated to the Yield values were estimated applying the appropriate propagation law.
In the process of data analysis, due attention has been paid to some important sources of uncertainty. In the experimental sum spectrum, the peak at 8 MeV is not always isolated and well resolved in the high proton energy range, due to the presence of contaminants, coming from other thermonuclear reac-

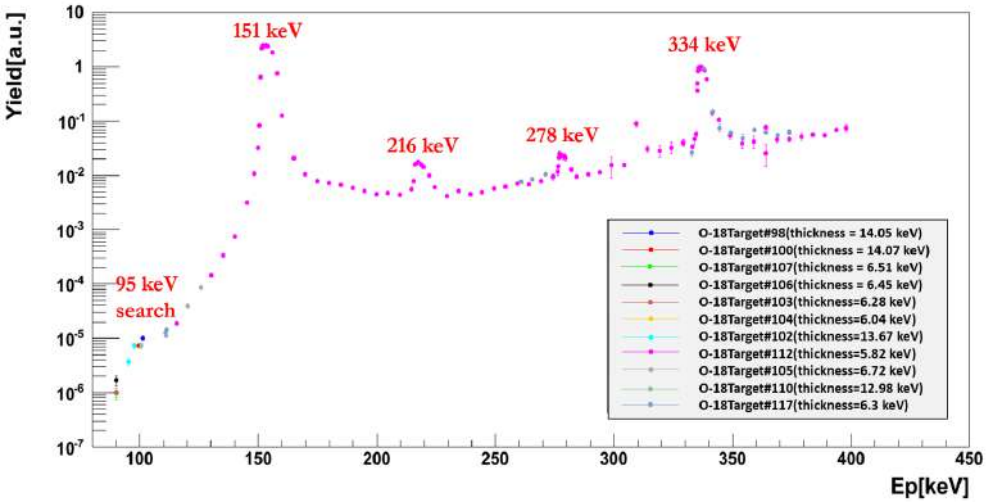

Figure 4.4: Excitation function for the BGO measurements. The Yield is in arbitrary units, i.e. $counts/\mu C$

tions that occur concurrently to the $^{18}O(p,\gamma)^{19}F$ reaction. Consequently, in such cases a deconvolution of two or more gaussians was needed in order to extract the counts coming from ^{19}F de-excitation. As an example, in Fig. 4.5 the influence of the 278 keV energy resonance of the $^{14}N(p,\gamma)^{15}O$ reaction, close to the 274 keV energy resonance of $^{18}O(p,\gamma)^{19}F$ reaction is illustrated . Other similar cases affect the 216 keV and the 334 keV resonance, which are very close to the $^{19}F(p,\alpha\gamma)$ resonance at 224 keV and 340 keV respectively, in which a consistent background overlaps with the signal at around 8 MeV. The energy around 310 keV was instead influenced by the 310 keV energy resonance of the $^{23}Na(p,\gamma)^{24}Mg$ reaction.
A further discussion on contaminants and beam-induced backgrounds will also be given for the HPGe case.
The low energy range does not result affected by contaminations, so the signal around 8 MeV could be very clear.

4.1.1 Direct capture cross section and low energy resonance

The non resonant (i.e. far from resonances) Yield data were used in order to estimate the direct capture cross section following two procedures. The results obtained are summarized in Fig. 4.7 and the agreement between the two approaches is fairly good.

The first procedure was based on the calculation of the direct astrophysical factor S(E) via numerical integration, starting from the experimental values of the excitation function and assuming the astrophysical factor approximately

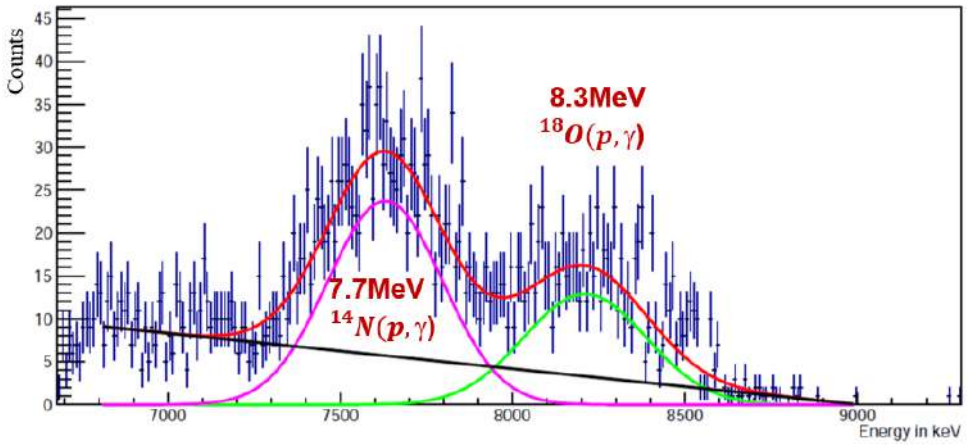

Figure 4.5: Gaussian deconvolution of two peaks with a linear background subtraction.

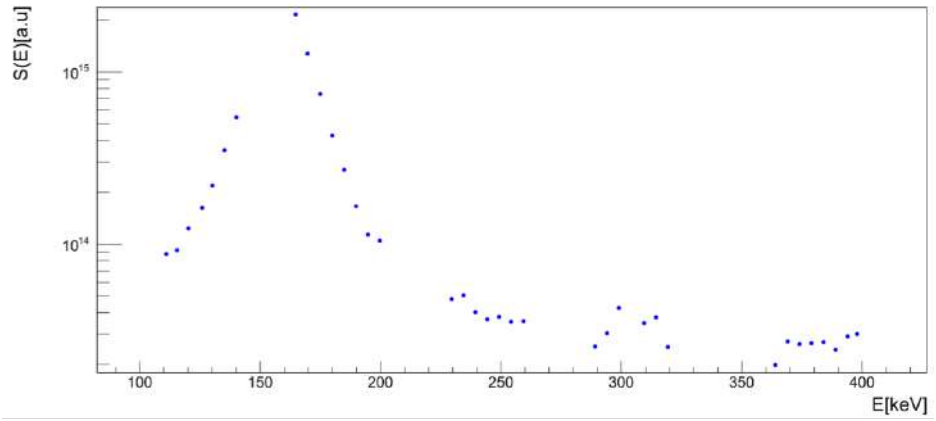

Figure 4.6: Non-resonant astrophysical factor

constant in the target thickness. The direct cross section values were calculated from the transmission through barrier model $\sigma_{DC} = \frac{S(E)}{E} \cdot e^{-2\pi\eta}$. Thus, the combination of Eq. (1.10) with Eq. (1.18), allows one to express [14] the S(E) as:

$$S(E) = \frac{Y}{\int_{E_p-\Delta}^{E_p} \frac{1}{\epsilon_{eff}} \frac{1}{E} e^{-2\pi\eta} dE} \tag{4.2}$$

This S(E) estimation results fairly rough, because the non-resonant component is strongly influenced by the tails of the 151, 216, 274 and 334 keV resonances.

The second one was based on the direct capture cross section calculation, performed at the effective energy, using Eq. (1.19).

If attention is paid at the low energy range in which the existence of the

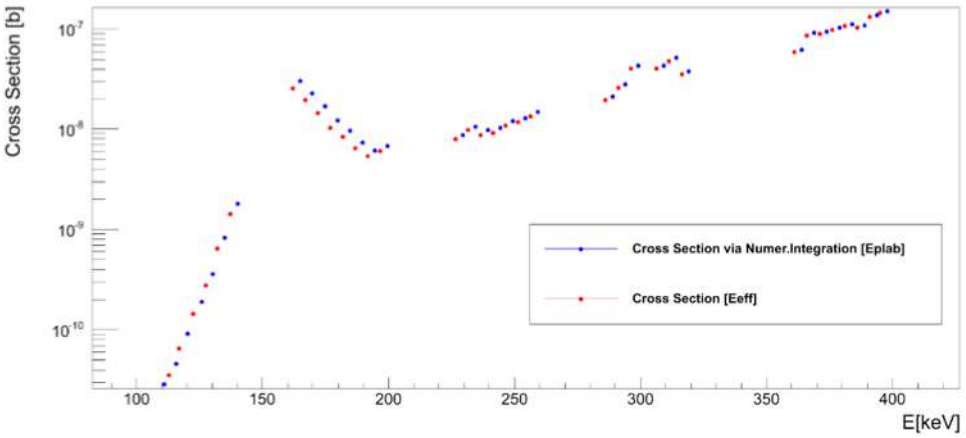

Figure 4.7: Direct capture cross section.

95 keV hypothetical resonance was guessed, this method leads to a value of 20 pb for the cross section, higher than the literature values [7] and [5], due to the influence of resonance tails, especially the nearby 151 keV. For this analysis the 4π coverage with the BGO was essential, because of the very weak signal at the energy of the excited level. Only through the integration it could be possible to detect any counts over the environmental background (Fig. 4.8), whereas the single BGO spectrum barely shows any signal (Fig. 4.8).

After such analysis the excitation function around 95 keV (Fig. 4.9) does not show any signature of a resonance as strong as predicted by H. T. Fortune et al. [6]. Therefore only an upper limit of the strength was estimated and reported in the summary (section 4.5) of the present work.

4.2 HPGe experimental spectra

The analysis of the HPGe spectra, characterized by high data quality, thanks to the high energy resolution, was based on the identification of all peaks coming from the reaction of interest, from contaminants, from environmental background, from escape peaks.
The main scope for each resonance spectrum is to identify all possible $\gamma-$ray primaries, and consequently all detectable $\gamma-$ray secondaries belonging to one or several cascades decaying to the compound nucleus ground state. Each resonance spectrum presents several $\gamma-$ray peaks not always well solved, due to the remarkable number of $\gamma-$rays. A list of all detected gammas was extracted for each resonance spectrum, and the net areas were calculated applying a procedure similar to the one for the BGO spectra. Only in a few cases, the HPGe high energy resolution was not enough to separate all

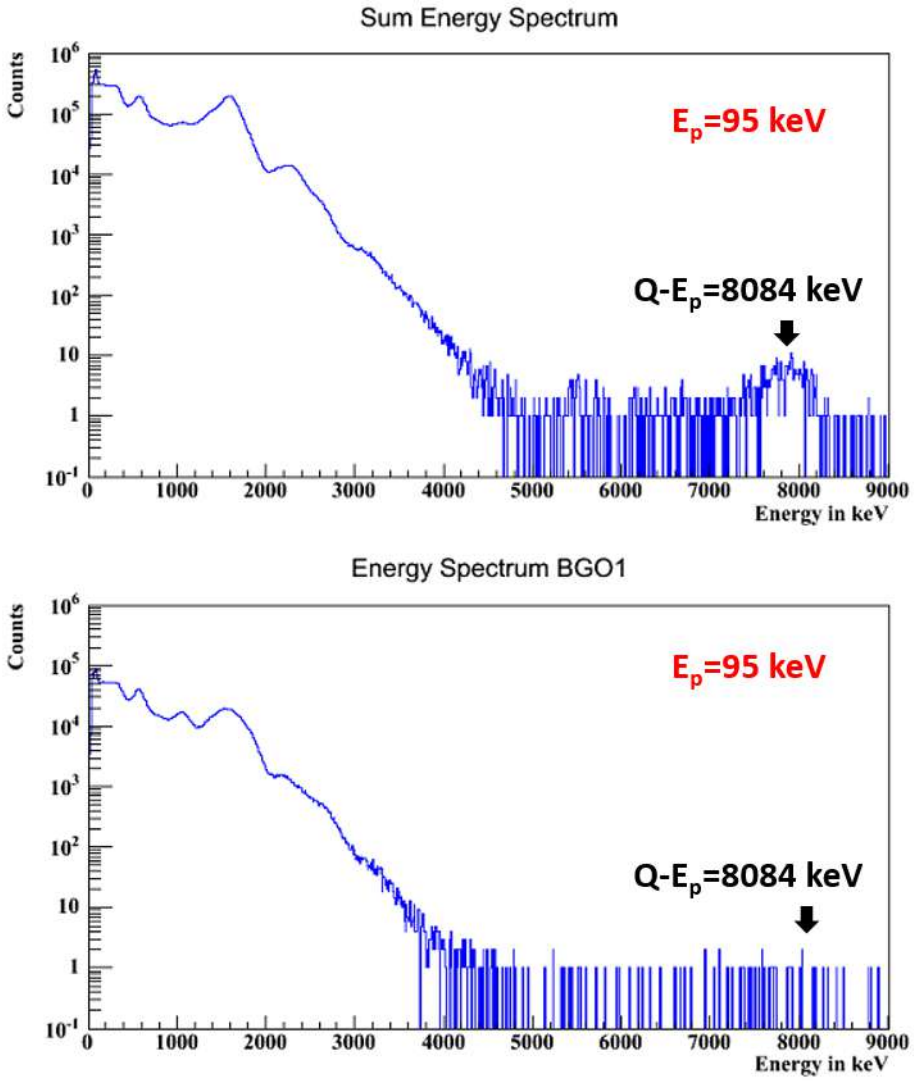

Figure 4.8: Up: BGO sum spectrum performed at 95 keV, down: BGO single spectrum performed at 95 keV.

peaks, when energy was very close to each other. For this reason the attempt to disentangle the overlapping peaks by the simple deconvolution of two or more gaussians had to be accompanied by a weighting procedure accounting for the different strengths of sligthly overlapping resonances.
As an example of such complication, we can consider (Fig. 4.10) the peaks in the experimental spectrum acquired at the on-resonance proton energy of 274 keV. These peaks result overlapped with the high energy tail of the strong 151 keV proton energy resonance. The peak E corresponding to the 8254 $\rightarrow$ 110 transition results broader than expected, since it is very close to another peak D coming from the 8138 $\rightarrow$ 0 transition.

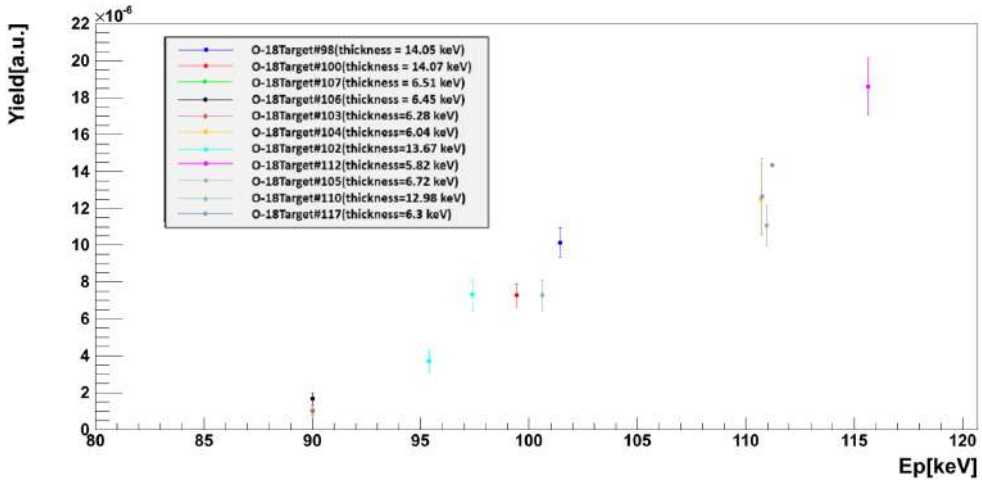

Figure 4.9: Excitation function around 95 keV.

The D contribution could estimated using the equality between the ratio of the peak contribution A (8138 $\rightarrow$ 110) and B (8138 $\rightarrow$ 0) coming from 151 keV resonance and of the correspondent transitions C (8138 $\rightarrow$ 110) and D coming from 274 keV resonance.
Generalizing, coincident or very close peaks can be put in proportion in order to obtain the net areas. This procedure was applied in all similar situations, in order to list for each resonance the correct net areas contributions.

4.3 Environmental and beam induced background

The beam induced background contributions could influence significantly the measurements of the reaction of interest. These backgrounds, that are part of the target or chemical contaminants, are caused by spurious reactions coming from different nuclides. Consequently spurious reactions occur concurrently with $^{18}O(p,\gamma)^{19}F$ reaction, causing contaminated regions in the experimental spectra. If spurious reactions are characterized by a Q-value comparable or larger than the Q-value of the reaction of interest, it could influence significantly the quality of the spectra, those in particular performed with summing detector.

For the search of possible resonant behaviour at very low energy, relevant spectra were acquired to measure BGO environmental and beam induced background, which could hinder the quest for such weak signal around 100 keV. The beam induced background spectra were obtained at an energy of 99 keV, using a blank solid Ta_2O_5 target prepared with inert water by anodiza-

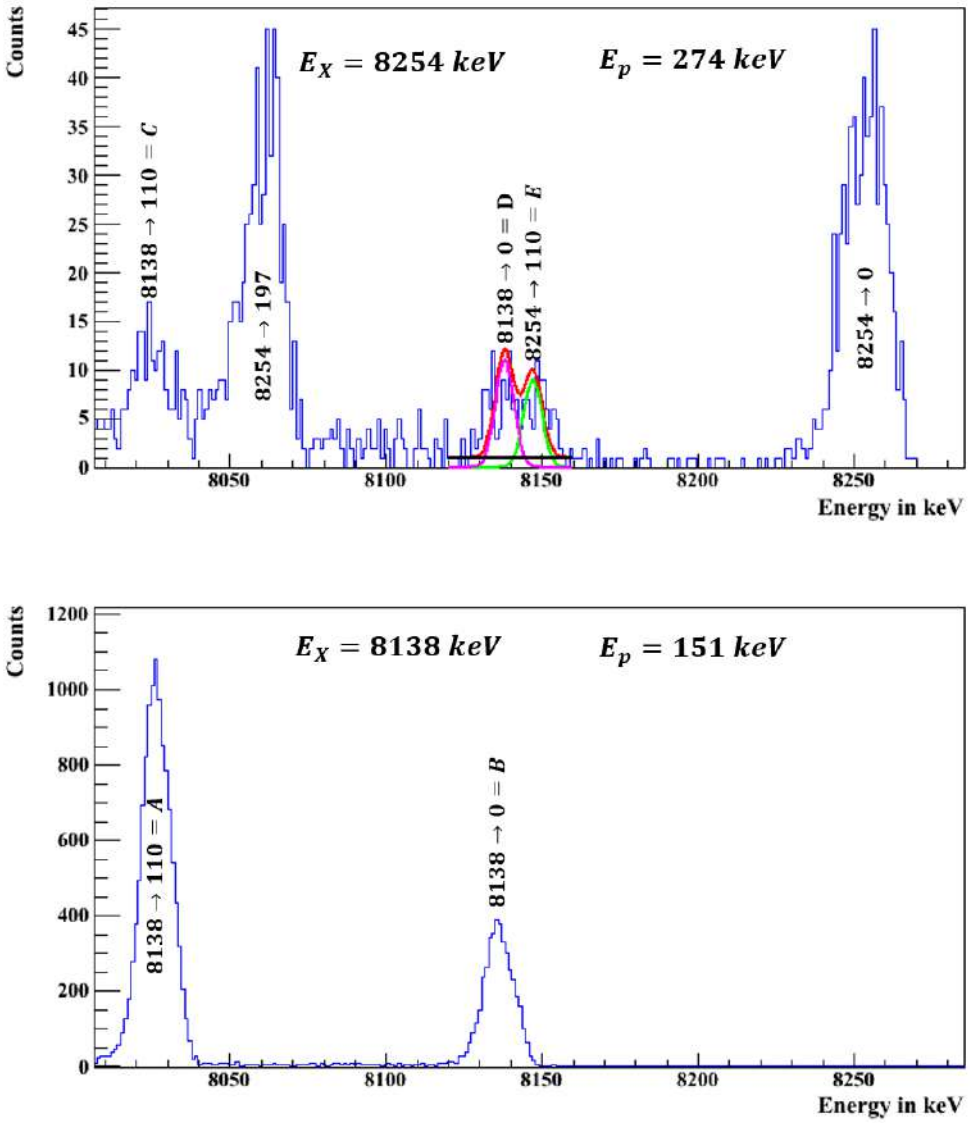

Figure 4.10: Top, a zoom of the experimental spectra acquired at 274 keV energy resonance, in which the tails effects coming from the 151 keV resonance are identified. Two peaks around 8140 keV are not solved because two close. Bottom, a zoom of the experimental spectrum acquired at 151 keV, in which two transitions are identified.

tion, in the same way of all other targets. For each spectrum the counts per second in the range around 8 MeV were calculated (Table. 4.1).

The counts per second for each measurement were plotted Fig. 4.11 in the respective poissonian 95% confidence interval [71, 72, 73, 74], in order to verify the consistence of all measurements.

Table 4.1: Background measurements compatibility.

Background type	Live time (s)	$\frac{Counts}{s}$	$\frac{Confidence\ intervals}{s}$
Environ.	244651.4	$8.17 \cdot 10^{-5}$	$4.99 \cdot 10^{-5} - 1.26 \cdot 10^{-4}$
Environ.	52446	$1.91 \cdot 10^{-5}$	$4.82 \cdot 10^{-7} - 1.06 \cdot 10^{-4}$
Environ.	231455.3	$4.32 \cdot 10^{-5}$	$2.05 \cdot 10^{-5} - 7.95 \cdot 10^{-4}$
Blank at 99 keV	81478	$7.36 \cdot 10^{-5}$	$2.70 \cdot 10^{-5} - 1.60 \cdot 10^{-4}$
Environ.	50105	$2.00 \cdot 10^{-5}$	$5.05 \cdot 10^{-7} - 1.11 \cdot 10^{-4}$
Environ.	55162	$1.09 \cdot 10^{-4}$	$3.99 \cdot 10^{-5} - 3.37 \cdot 10^{-4}$
Environ.	258258.4	$8.13 \cdot 10^{-5}$	$5.03 \cdot 10^{-5} - 1.17 \cdot 10^{-4}$

All measurements appear comparable within confidence intervals, therefore measurements around 100 keV do not seem to be affected by concurrent spurious reactions at 8 MeV.

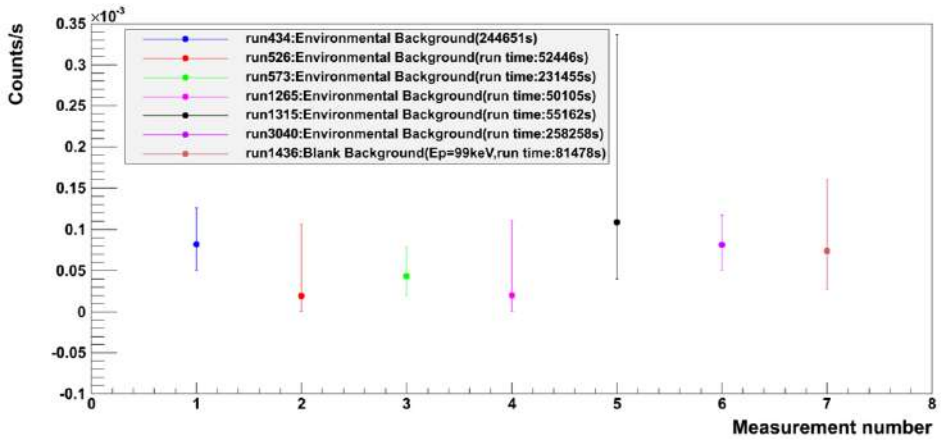

Figure 4.11: Counts per second at 8 MeV, measured with BGO setup for each environmental background spectrum and for a beam induced background spectrum, performed at 99 keV, using a blank.

Resonances in the cross sections of the spurious reactions act in the measurement range for the $^{18}O(p,\gamma)^{19}F$ reaction and cause a particular background contribution. Different background contributions have been observed during the BGO and HPGe phases.

The proton capture reaction $^{11}B(p,\gamma)$, with Q-value of 15956.85 keV is characterized by a broad resonance at 162 keV proton energy (Γ= 5.3 keV)[75]. This broad resonance is close to the 151 keV resonance of the studied reaction, but does not disturb the $^{18}O(p,\gamma)^{19}F$ reaction lines, as will be explained in 4.4.1.

$^{12}C(p,\gamma)$ reaction (Q = 1943.49 keV) has been observed in the HPGe spectra due to the non-resonant cross section, the contributions result negli-

gible.

$^{19}F(p,\alpha\gamma)^{16}O$ reaction (Q = 8113 keV) is characterized by two resonances at proton energy of 224 keV and 340.5 keV, which lead to the emission of three well solved gamma rays at 6.13, 6.92 and 7.12 MeV [76], [77]. The beam induced background contributions coming from $^{19}F(p,\alpha\gamma)^{16}O$ reaction could influence data quality of the resonance measurements performed at 216 keV and 334 keV of the $^{18}O(p,\gamma)^{19}F$ reaction. The fluorine contamination was reduced during the ^{18}O target preparation avoiding the use of hydrofluoric acid.

$^{23}Na(p,\gamma)^{24}Mg$ reaction (Q=11.69 MeV) is characterized by a strongest resonance at a proton energy of 310 keV, close to the 334 keV resonance of the studied reaction causing a critical background around 8 MeV. The data taking of the $^{23}Na(p,\gamma)^{24}Mg$ reaction was alternated with the $^{18}O(p,\gamma)^{19}F$ reaction one. Probably contaminations of this spurious reaction are due to the not perfect cleaning of the target chamber.

$^{14}N(p,\gamma)^{15}O$ reaction (Q=7556 keV) is characterized by a resonance at 278 keV, very close to the 274 keV resonance of the $^{18}O(p,\gamma)^{19}F$ reaction. The Q-value of this spurious reaction is very close to the reaction Q-value of the studied reaction, so it could disturb the BGO analysis around the 8 MeV peak (as seen in Fig. 4.5) at the resonance energy of 274 keV resonance and the HPGe analysis as explained in 4.4.3.

A preliminary qualitative identification of contaminant reactions was performed during the analysis of the $^{18}O(p,\gamma)^{19}F$ reaction.

The identification of the contaminants has been facilitated thanks to the comparison between the experimental spectra and the simulated ones in correspondence of the resonance energies regarding the involved reactions.

For example, the comparison between the experimental spectrum performed at 216 keV energy resonance and the simulated one, shows that there is no presence of contaminants (see Fig. 4.12). On the contrary at the 274 keV energy resonance, the experimental spectrum presents $^{23}Na(p,\gamma)^{24}Mg$ contaminant, as confirmed from the red simulated spectrum of the spurious reaction involved (see Fig. 4.13).

The $^{23}Na(p,\gamma)^{24}Mg$ contaminant reaction was checked comparing and subtracting the $^{18}O(p,\gamma)^{19}F$ experimental spectrum at 310 keV energy resonance of $^{23}Na(p,\gamma)^{24}Mg$ from the beam induced background spectrum performed at the same energy using a blank solid Ta_2O5 prepared with inert water by anodization. The peaks present in the resulting spectrum have its origin in the studied reaction, because the peaks coming from the $^{23}Na(p,\gamma)^{24}Mg$ reaction are removed in the subtraction (Fig. 4.14).

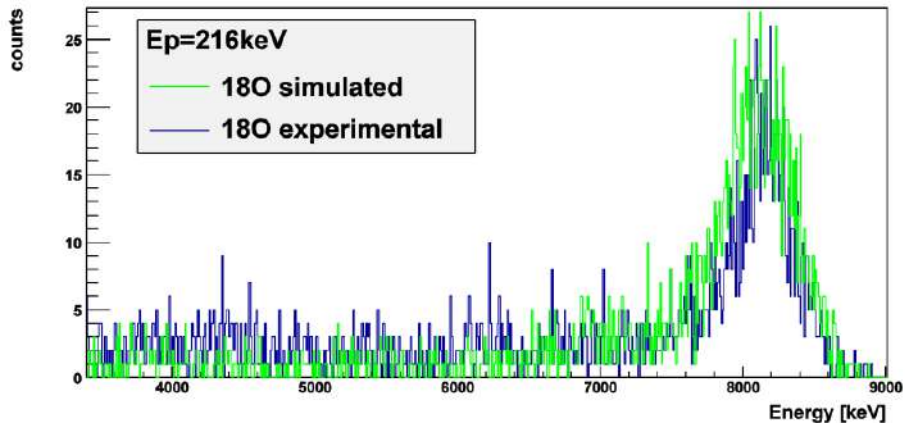

Figure 4.12: No evidence of contaminants at 216 keV from comparison between the experimental and simulated spectra.

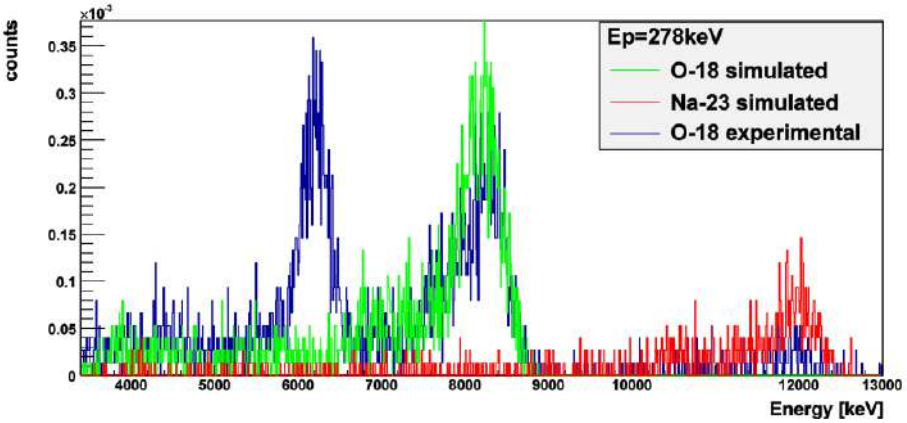

Figure 4.13: Evidence of $^{23}Na(p,\gamma)^{24}Mg$ contaminant, from comparison between experimental and simulated spectra.

4.4 HPGe data analysis

The data taking focused on scans and measurements of the 151 keV, 216 keV, 278 keV, 334 keV resonances. Other data points were acquired mostly at energies between the resonances in the range 140-400 keV, trying to measure the direct capture component.
All measurements were performed in a close-geometry configuration. The data analysis was devoted to identify all transitions from the compound nucleus excited level to the ground state, associate them into cascades, estimate the peak areas accounting for background sources, and estimate the branching ratios taking into account the energy and efficiency calibrations of the detector, and finally provide an estimate of the resonance strengths.
A summary of the integrated experimental run parameters for these measure-

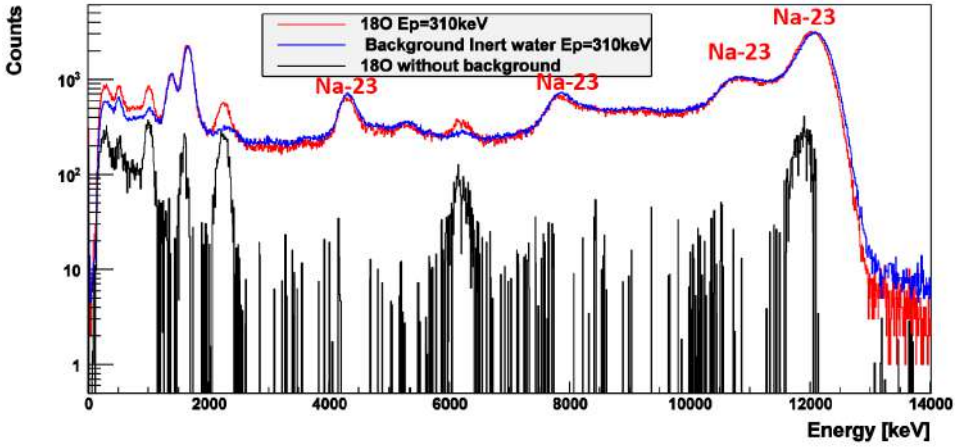

Figure 4.14: Comparison and subtraction between $^{18}O(p,\gamma)^{19}F$ experimental spectrum at 310 keV and beam-induced background spectrum at the same energy.

ments is reported in Table 4.2. In the present section, details on analysis and results for each resonance will be reported.

Table 4.2: Experimental run information regarding the data taking for the resonances measured in the present work.

Resonance(keV)	Accumulated charge(μC)	Real time(s)	Live time(s)
151	1271966	11979	11889
216	15738065	122206	122171
274	3760791	55889	55862
334	3492131	74887	74412

4.4.1 151 keV resonance

The 151 keV resonance, being the strongest and best known resonance of the ^{18}O(p, γ)^{19}F reaction, was used to check and monitor the target degradation during the long beam irradiation, as detailed in Chapter 3, and scanned several times with different targets. A total of 103 experimental spectra taken in the long data acquisition sessions were summed at a proton energy of 154 keV (on the yield plateau) in order to search with high statistics all possible primary transitions from the resonance excited state at $E_X = 8138$ keV.
Eight possible primary transitions could be identified, one of them new with respect to the literature [7]. In the summed spectrum (Fig. 4.15) the eight primary transitions and accompanying secondary transitions where detectable. Escape, double escape peaks and a contaminant peak coming from $^{11}B(p,\gamma)$

reaction were also detected, owing to the Germanium high resolution. Fortunately, the contaminant peak (4423 keV) from $^{11}B(p,\gamma)$ reaction is off energy with respect to any γ-ray of interest.

The primary peak at 2200 keV is instead coincident with the environmental background peak at 2200 keV coming from ^{214}Bi, so the latter contribution had to be subtracted by using the measured environmental background rate. All secondary transitions following the three primary transitions above 5 MeV are not visible. The five remaining primaries have clear signature (Fig. 4.16) from all secondaries [78], well visible in the spectrum. Examining the 5938 keV and 6255 keV excited states, one has to consider [79] that γ decay competes with α-particle emission with a final ^{15}N residual. For the 6255 keV state, α-particle emission is [4] the only decay channel, as also confirmed [80] by the lack of $\gamma\gamma$-coincidences when the level is fed from the 8138 keV $\rightarrow$ 6255 keV primary transition.
According to [81], instead, the α-particle channel is predominant in the decay of the 5938 keV excited state.

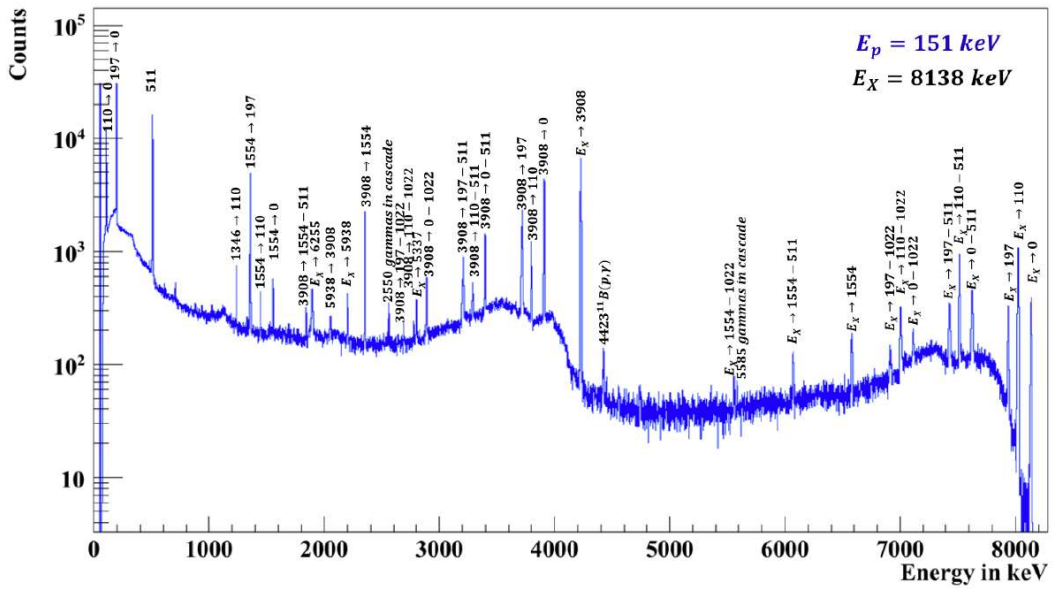

Figure 4.15: HPGe spectrum acquired on the 151 keV resonance, with all transitions indicated. All possible primary transitions according to the known level scheme of ^{19}F are observed.

The previously unknown 2800 keV γ primary (Table 4.10), due to the transition 8138 keV$\rightarrow$5337 keV needed some extra check, since no apparent associated secondaries are evident from the spectra. In fact, literature [81] reports a predominant α-particle decay for the 5337 keV level, that could justify the missing secondaries. However the γ decay channel is also admitted

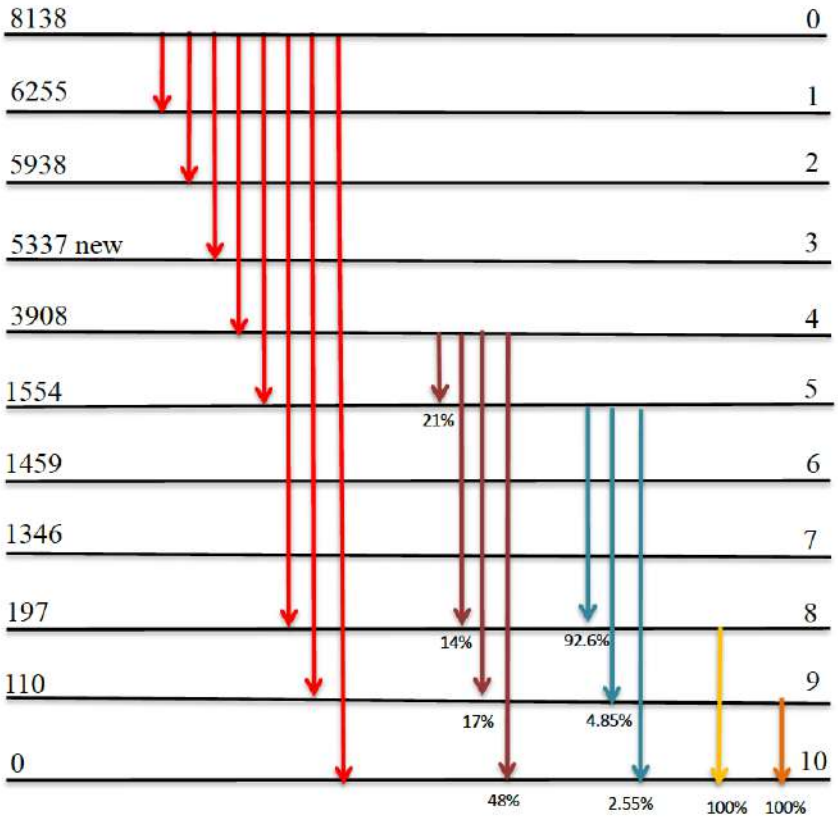

Figure 4.16: Level scheme of the 151 keV resonance. All transitions measured in the present experiment are displayed.

[78] (see Fig. 4.17).

Table 4.3: Experimental information regarding the peak at 2800 keV from the present measurement.

Counts	η_{exp}^{FEP}	Emitted gammas
1210	1.86E-02	65054

In order to qualify this assumption, we have examined a bump (Fig. 4.18) at 5227 keV in the experimental spectrum, to check if it could be a γ secondary (Table 4.4), which is reported to have branching ratio equal to 42%.

The number of emitted gammas for the would-be new primary at 2800 keV, a generic associated secondary and the number of expected gammas for generic secondary are expected to be determined by the proportions of Eqs. (4.3),(4.4) and (4.5), respectively.

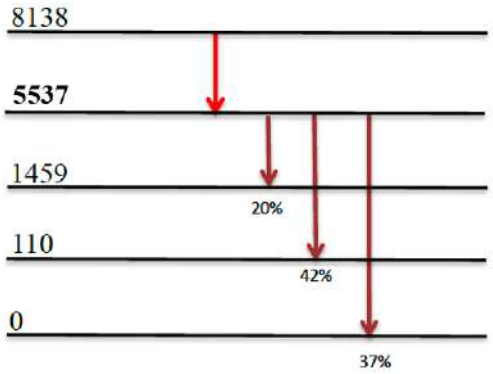

Figure 4.17: γ cascade of the level at 5337 keV.

$$N_{Em\gamma}(2800keV) = \frac{Counts(2800keV)}{\eta_{exp}^{FEP}(2800keV)} \tag{4.3}$$

$$N_{Em\gamma}(E_{secondary}) = N_{Em\gamma}(2800keV)B_{secondary} \tag{4.4}$$

$$N_{Ex\gamma}(E_{secondary}) = N_{Em\gamma}(E_{secondary})\eta_{exp}^{FEP}(E_{secondary}) \tag{4.5}$$

Table 4.4: Information regarding the secondaries of the 2800keV primary.

Eγ(keV)	Branchings [78]	emitted gammas	expected gammas	FEPE
3878	20%	12973	188	1.45E-02
5227	42%	27243	306	1.12E-02
5337	37%	24000	265	1.10E-02

From the comparison (see Fig. 4.18 and 4.19) of the estimated and experimental signals around 5227 keV there is no strong evidence of a peak. A similar situation is also found in another adjacent region of the spectrum (around 5244 keV), where a possible bump could be guessed. For this reason we can conclude that the 2800 keV gamma is a primary, followed by a nearly 100% α-particle decay of the 5337 keV level, according to [81].

4.4.2 216 keV resonance

The resonance at 216 keV is not among the ones already measured in literature. This is the first measurement in which the branching ratios of the associated primaries could be extracted. Two experimental spectra were summed on the plateau energy (224 keV) in order to increase the statistics and were

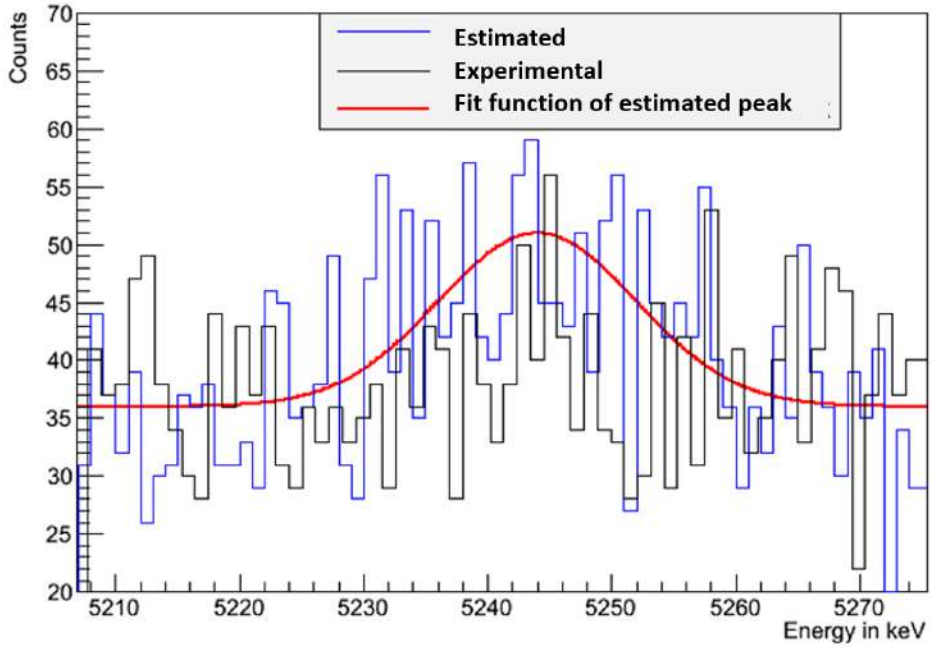

Figure 4.18: Signals comparison around 5244 keV.

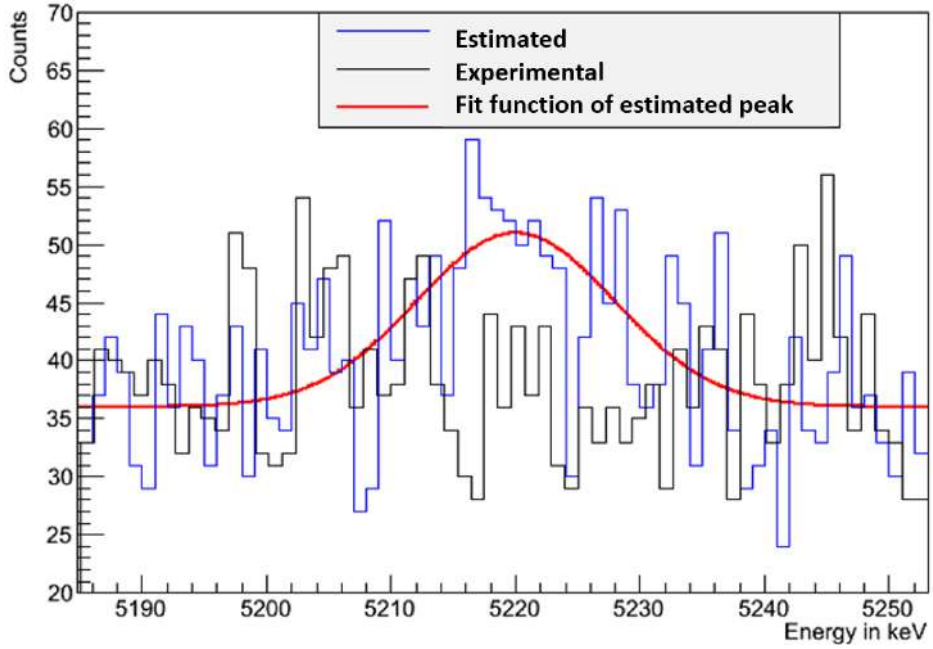

Figure 4.19: Signals comparison around 5220 keV.

analysed, searching for all possible primary transitions starting from the resonant state at $E_X = 8199$ keV.
Seven hypothetical primaries are identified and the corresponding secondary

transitions where visible (see Fig. 4.20). Escape, double escape peaks and

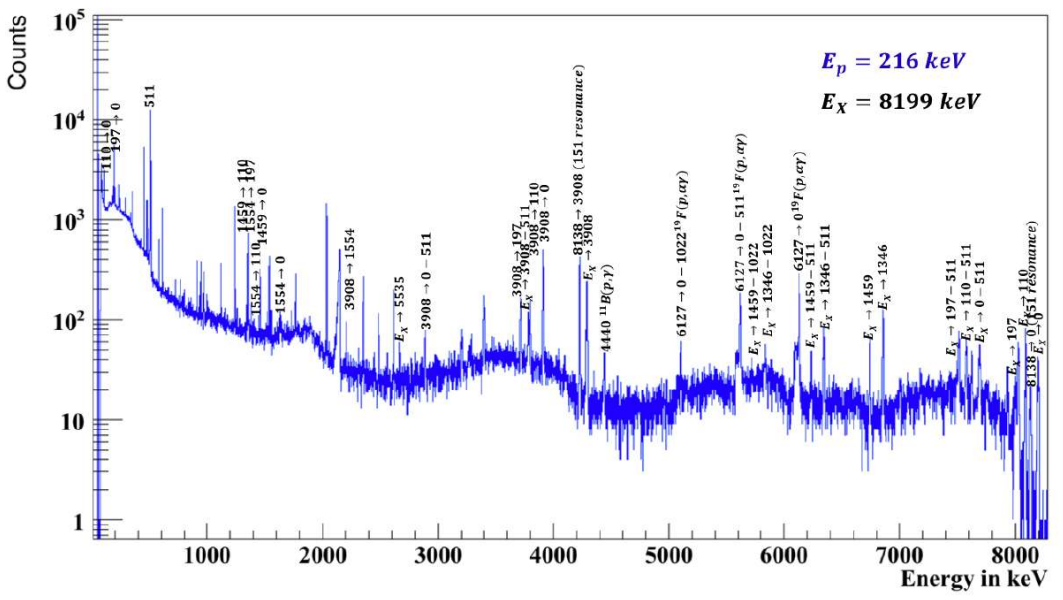

Figure 4.20: HPGe spectrum acquired on the 216 keV resonance, with all transitions indicated. All observed primary transitions are indicated.

contaminant peaks coming from $^{11}B(p,\gamma)$ and $^{19}F(p,\alpha\gamma)$ reactions are present (see Fig. 4.20), but the energies of contaminant and environmental background peaks are not coincident with the energies of the primaries.

Also here we have measured a transition to the 5535 keV level, where no secondaries are detected, similarly to what reported in one case of the 151 keV resonance. This is compatible with the work [81], where the α-particle channel is the main branch of decay of the 5535 keV level. The remaining states below 5 MeV are characterized by γ cascades [78] well visible (Fig. 4.20, 4.21) in the spectrum.

4.4.3 274 keV resonance

The resonance at 274 keV was studied analysing one experimental spectrum (see 4.22) characterized by a sufficient statistics such as to allow the identification of seven primary transitions, starting from the resonant state at E_X = 8254 keV.
All excited states that are involved have an energy below 5 MeV, so the γ channel predominates on the α channel and the secondary transitions are visible in the spectrum ([78]). The level scheme (4.23) illustrates the cascades involved. From the comparison with the literature data [7] emerges that the present measurement has detected three new primaries.

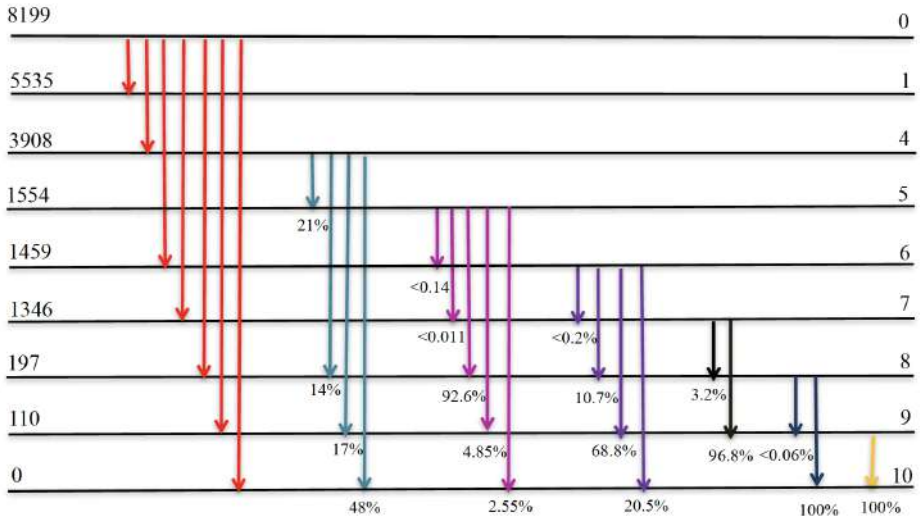

Figure 4.21: Level scheme of the 216 keV resonance. The transitions measured in the present experiment are displayed.

Escape, double escape, contaminant and environmental background peaks are identified. In particular, in this energy range, we detected contaminant peaks coming from the $^{14}N(p,\gamma)^{15}O$ reaction, that is characterized by a resonance at 278 keV [61], very close to the 274 keV resonance of $^{18}O(p,\gamma)^{19}F$ reaction. In fact, a possible primary at 6795 keV has an energy which overlaps with the contaminant peak at 6797 keV coming from $^{14}N(p,\gamma)^{15}O$ reaction. The contribution of this source of contamination was subtracted, using the information coming from a custom measurement on ^{14}N target, performed at the resonance energy, and the known count rates from the resonance strength.

4.4.4 334 keV resonance

The highest energy resonance (334 keV) measurable with the LUNA-400 accelerator was studied analysing one experimental spectrum (Fig. 4.24) characterized by a sufficient statistics such as to allow the identification of 21 primary transitions, starting from the resonant state at $E_X = 8310$ keV. The spectrum is divided into two parts, considering the large number of identified peaks. The level scheme (Fig. 4.25) clarifies the large number of cascades involved . Among the 21 primary transitions detected, 18 are new (Fig. 4.25) compared to the literature values [7]. The states below 5 MeV are characterized by γ cascades well visible [78] (Fig. 4.24 4.25). For the ones above 5 keV, the same consideration on the open α-channel applies [82], [81], [83], as in previous resonances. Escape, double escape, environmental, and contaminant peaks coming from $^{19}F(p,\alpha\gamma)$, $^{23}Na(p,\gamma)^{24}Mg$, $^{12}C(p,\gamma)$ reactions are iden-

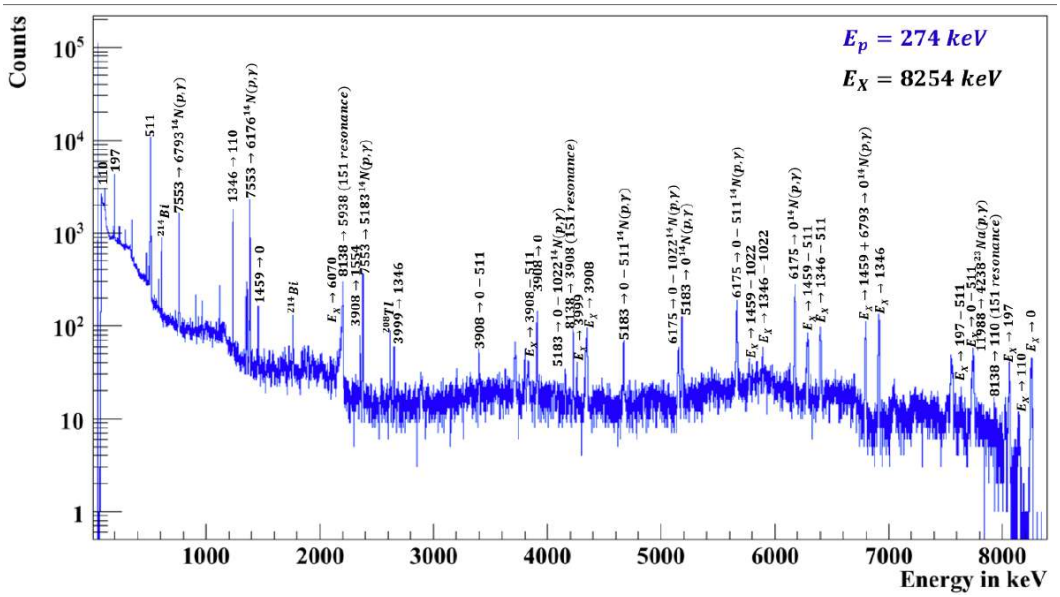

Figure 4.22: HPGe spectrum acquired on the 274 keV resonance, with all transitions indicated. All observed primary transitions are indicated in this plot.

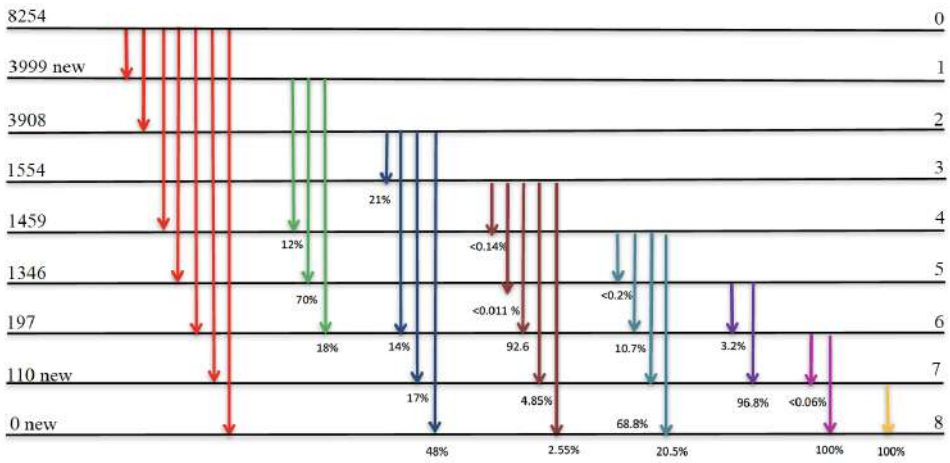

Figure 4.23: Level scheme of the 274 keV resonance. The transitions measured in the present experiment are displayed.

tified. As previously discussed 4.3, the $^{19}F(p, \alpha\gamma)$ reaction is characterized by a resonance at 340 keV, very close to the 334 keV resonance and creates a strong background in the spectrum. Also the $^{23}Na(p, \gamma)^{24}Mg$ reaction has a resonance at 310 keV, very close to the 334 keV resonance, but its lines do not disturb the studied reaction.

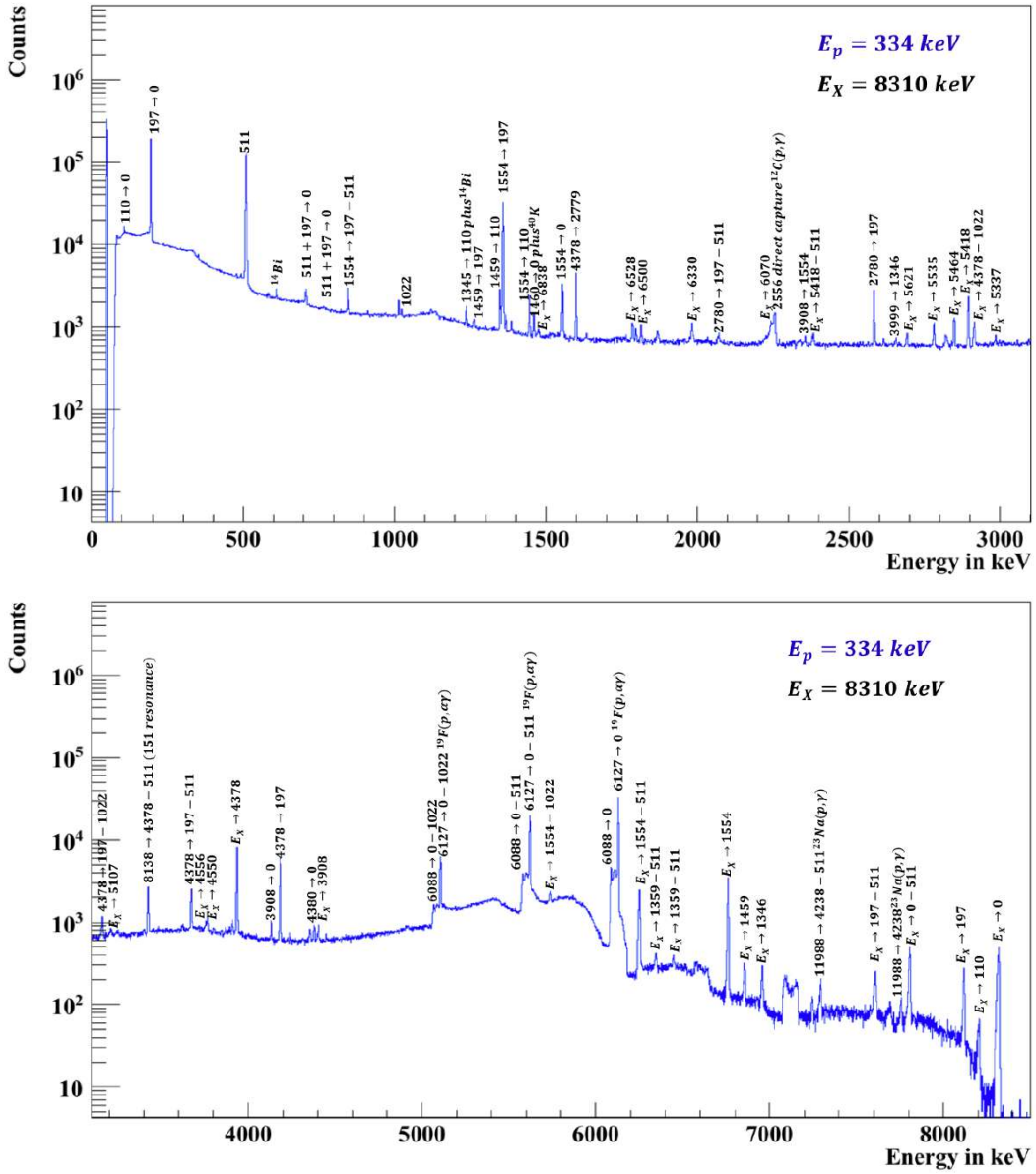

Figure 4.24: HPGe spectrum acquired on the 334 keV resonance, with all transitions indicated. All observed possible primary transitions are indicated in this plot.

The direct capture of $^{12}C(p,\gamma)$ reaction creates a peak at 2556 keV, very close to a possible primary of the 334 keV resonance, so a deconvolution was necessary to calculate the correct contribution of the associated primary transition. Finally, tail of the strongest 151 keV resonance influencing the spectrum, are also accounted for in the estimation of the true peak counts.

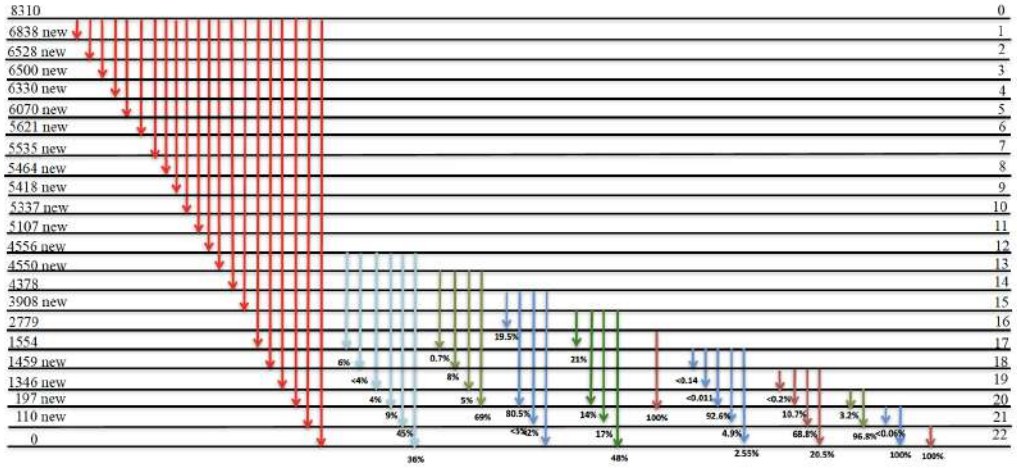

Figure 4.25: Level scheme of the 334 keV resonance. The transitions measured in the present experiment are displayed.

4.4.5 Branching ratios calculation and results

For each studied resonance, the number of counts for the gamma lines corresponding to the number of primary transitions were determined for all experimental spectra. Starting from these experimental quantities, the branching ratios were estimated, accounting for the energy dependent efficiency as from the calibration described in Chapter 3, and including summing in and summing out corrections.

The cascades following from each primary transition could be determined in those cases where all the possible secondary transitions are detected. The branchings corresponding to the secondary transitions are taken from literature [78].
Using the calibrated efficiencies η^{FEP} and η^{TOT}, the probability P_{ij} for each possible $j-$th primary transition which contributes to the full energy peak to its own or to other higher energy primaries (via summing in) could be estimated, in terms the branching ratios B_i. The number of counts N_i in each primary peak will be then related to the P_{ij} and the total number of reactions (rate times livetime) N_R by a linear matrix equation (Eq. (4.6)) with a normalization condition (Eq. (4.7)) on branching ratios:

$$\begin{pmatrix} N_1 \\ N_2 \\ . \\ . \\ N_n \end{pmatrix} = N_R \begin{pmatrix} P_{11} & \cdots & P_{1n} \\ P_{21} & \cdots & P_{2n} \\ \cdot & \cdots & \cdot \\ \cdot & \cdots & \cdot \\ P_{n1} & \cdots & P_{nn} \end{pmatrix} \begin{pmatrix} B_1 \\ B_2 \\ . \\ . \\ B_n \end{pmatrix} \tag{4.6}$$

$$\sum_i B_i = 100\% \tag{4.7}$$

The uncertainties on the derived branchings were calculated by propagating the errors in the peak counts, with and without summing corrections, to account for the uncertainty related to these latter contributions.

The primary branching ratios and the associated uncertainties thus estimated are reported for all resonances in Tables 4.5, 4.6, 4.7, 4.8 and compared to the literature values.
The Table 4.5 shows the primary branching ratios obtained for the 151 keV resonance. Since the newly detected primary γ-ray at 2800 keV has a branch-

Table 4.5: Primary branching ratios at 151 keV.

Eγ(keV)	State(keV)	Branchings (%) (LUNA)	Branchings(%) Wiescher *et al.* [7]	Branchings(%) J. R. Dermigny *et al.* [80]	
				singles	$\gamma\gamma$-coincidence
1883	6255	2.10 ± 0.08	3 ± 1	1.4 ± 2	
2200	5938	1.05 ± 0.07	1.0 ± 0.5	0.9 ± 2	<1.3
2800	5337	0.92 ± 0.19			
4230	3908	54.42 ± 1.11	54 ± 2	57.4 ± 5	58.0 ± 6
6583	1554	2.07 ± 0.41	2 ± 1	1.2 ± 2	1.0 ± 2
7941	197	7.18 ± 0.24	8 ± 1	7.1 ± 5	7.9 ± 9
8028	110	23.85 ± 0.05	24 ± 2	23.5 ± 6	24.7 ± 10
8138	0	8.40 ± 0.17	8 ± 2	8.5 ± 5	6.8 ± 8

ing smaller than 1%, all the other ones are in fair agreement with the literature values.

Table 4.6 shows the primary branching ratios obtained for the 216 keV resonance. This was measured at the LUNA experiment for the first time and there are no other values in literature.

Table 4.6: Primary branching ratios at 216 keV.

Eγ(keV)	State(keV)	Branchings (%) (LUNA)
2664	5535	1.6 ± 0.3
4291	3908	30.2 ± 1.1
6740	1459	10.5 ± 0.3
6853	1346	21.7 ± 2.9
8002	197	8.7 ± 1.1
8089	110	14.6 ± 1.1
8199	0	12.6 ± 1.6

Table 4.7 shows the primary branching ratios obtained for the 274 keV resonance. There are three new primary transitions compared to the literature values. The primary branching ratio regarding the 8254 $\rightarrow$ 1459 transition is quite smaller than the literature one, because (subsection 4.4.3), it was accurately corrected by subtracting the contamination from $^{14}N(p,\gamma)^{15}O$, which probably affected the literature value.

Table 4.7: Primary branching ratios at 274 keV.

Eγ(keV)	State(keV)	Branchings (%) (LUNA)	Brachings(%) Wiescher *et al.* [7]
4257	3999	3.0 $\pm$ 1.0	
4346	3908	13.4 $\pm$ 3.6	25 $\pm$ 8
6795	1459	5.1 $\pm$ 0.2	24 $\pm$ 8
6910	1346	37.3 $\pm$ 4.5	33 $\pm$ 10
8057	197	14.5 $\pm$ 2.4	18 $\pm$ 7
8144	110	3.6 $\pm$ 1.5	
8254	0	23.1 $\pm$ 2.8	

Table 4.8 shows the primary branching ratios obtained for the 334 keV resonance. There are 18 new primary branching ratios compared to the literature values. The intensity of these 18 primary transitions is low, in fact the majority is characterized by branching ratios lower than 1%. The three primary branching ratios that are in common with the literature values are consequently lower, because of the strength fragmentation detected in the present high resolution measurement.

4.5 Resonance strengths

The resonance strengths from the present experiment were evaluated both from BGO and HPGe data and are reported in Table 4.9. The experimental observable which allows the definition of the resonance strength is the yield measured on the resonance plateau energy. The value of the strength is then estimated as $\omega\gamma = 2\epsilon(E_{res})Y/\lambda^2$ expressed in meV, as reported in the discussion of Chapter 1.

The uncertainties associated to the strengths were estimated summing in quadrature the statistical and the systematic uncertainty. The statistical uncertainty was simply estimated propagating the statistical error on the Yield. The systematic uncertainty includes the error coming from the measurement of the accumulated charge, which is estimated to be 2.5% and the error coming from the Stopping Power calculated by SRIM [67]. The mean stopping power errors in the 89-400 keV range of energy for Tantalum and the Oxygen

Table 4.8: Primary branching ratios at 334 keV.

Eγ(keV)	State(keV)	Branchings (%)	Brachings (%)
		LUNA	Wiescher *et al.* [7]
1472	6838	0.3 ± 0.1	
1782	6528	0.7 ± 0.2	
1810	6500	0.7 ± 0.1	
1980	6330	1.0 ± 0.2	
2240	6070	1.0 ± 0.8	
2689	5621	0.4 ± 0.1	
2775	5535	1.0 ± 0.2	
2846	5464	1.5 ± 0.4	
2892	5418	3.6 ± 0.9	
2973	5337	0.4 ± 0.1	
3203	5107	0.4 ± 0.1	
3754	4556	0.8 ± 0.3	
3760	4550	1.1 ± 0.2	
3932	4378	32.7 ± 1.2	40 ± 2
4402	3908	1.0 ± 0.8	
6756	1554	39.7 ± 4.2	48 ± 2
6851	1459	2.3 ± 0.3	
6964	1346	2.0 ± 0.2	
8113	197	2.9 ± 0.6	
8200	110	0.6 ± 0.3	
8310	0	5.9 ± 1.4	12 ± 1

are 5.8% and 2.9%, respectively. They are then combined into the Tantalum oxyde composition.

The strengths thus quoted from the BGO and HPGe data result in general to be consistent with each other, and in fairly good agreement with literature values. In particular, the case of the low-lying resonance at 95 keV can only provide us with an upper limit, remarkably lower that what estimated by Buckner et al., and very much lower than the prediction of Fortune et al. The 216 keV resonance shows instead some discrepancy between the BGO and HPGe results, the latter being almost a factor 2 higher.

Table 4.9: Resonance strengths

	Present				Literature		
$E_{plab}(keV)$	$\omega\gamma$(meV)	$\omega\gamma$(meV)	$\omega\gamma$(meV)	$\omega\gamma$(meV)	$\omega\gamma$ (meV)	$\omega\gamma$(meV)	$\omega\gamma$(meV)
	BGO LUNA	HPGe LUNA	Buckner *et al.*[5]	Fortune *et al.*[6]	Wiescher *et al.* [7]	Vogelaar *et al.*[8]	Iliadis *et al.*[33]
95	$\leq 1.94 \cdot 10^{-6}$		$\leq 7.8 \cdot 10^{-6}$	$0.0007^{+0.0056}_{-0.0038}$		$\leq 4.0 \cdot 10^{-5}$	
151	0.99±0.06	0.91±0.03			1.0±0.1	0.92±0.06	
216	0.0043±0.0003	0.0070±0.0002			>0.008	0.005±0.001	0.005±0.001
278	0.029±0.002	0.027±0.001			0.037±0.005		0.0024±0.005
334	0.98±0.05	0.90±0.032			0.95±0.08		

Conclusions

In this thesis an experimental study of the $^{18}O(p,\gamma)^{19}F$ reaction is presented. The measurement aimed at performing a more accurate characterisation of one process which is believed to participate in the proton burning astrophysics, opening the way to higher mass nucleosyntesis. In particular, the experiment wanted also to explore, owing to the very low background underground environment of LNGS, the very low energy extrapolation of the excitation function. In this respect, the possibility of detecting a very weak resonance at 95 keV was also explored, which according to some authors [6] could have an impact on the $^{18}O(p,\gamma)^{19}F$ reaction rate in the AGB stars temperature range (40 MK). The experiment wanted also to characterise some relevant known (151 keV, 274 keV and 334 keV) and less known (216 keV) resonances, for which the primary branching ratios were estimated.

A direct measurement was performed in an energy window from 400 keV down to 89 keV in the laboratory system, covering the astrophysical relevant energy useful to reach the aims of the study. Measurements to probe the existence of the low-lying resonance at 95 keV were performed during the high efficiency BGO 4π integrating crystal phase. This was accomplished by examining the counts at around the reaction Q-value, taking advantage of the high efficiency of the detector and of the very low background. A signal of some overcounts around 8 MeV was observed in the experimental spectrum at 95 keV. However the scan of the adjacent energies did not allow the clear detection of a structure signature of a resonance. On the basis of this observation only an upper limit for the resonance strength at 95 keV was estimated, lowering the previous one quoted by Buckner *et al.* [5], but definitely confirming the exclusion of the hypothesis reported by of Fortune *et al.* [6].

The other higher resonances were studied in detail thanks to the high energy resolution of the HPGe detector.

Data from BGO and HPGe setups were analysed by accurately controlling the different spurious contaminant reactions, that in some cases disturb significantly the resonance measurement of the $^{18}O(p,\gamma)^{19}F$ reaction. Also an accurate subtraction of beam induced backgrounds was performed.
Special efforts were made to calibrate the efficiency curve of the Ge-detector,

very important especially considering the close-geometry configuration at which all measurements were performed. The reaction of interest involves several γ-cascades, consequently summing in and out effects occur and are significant in a close geometry configuration.
Owing to the high resolution performance of the HPGe detector and the low background environment, a very accurate handling of the complex coincidence summing corrections was possible, thus allowing to measure the branching ratios of the 216 keV resonance, not previously present in literature, and a refining quotation of all other branching ratios for the 151 keV, the 274 keV, and 334 keV resonances. The branching ratios results on the strong 151 keV resonance are in good agreement with literature and a new γ-ray primary at 2800 keV was observed, which is followed by a nearly 100% $\alpha-$decay. For the 274 keV resonance three new γ-ray primaries are observed, which were not reported in literature, and one branching ratio could be more accurately re-evaluated through the subtraction of contaminant contribution coming from $^{14}N(p,\gamma)^{15}O$ reaction.
Eighteen new γ-ray primaries were observed for the 334 keV resonance and those characterized by a high intensity are in good agreement with literature values.

In summary, the present work improves some experimental evidence concerning the reaction $^{18}O(p,\gamma)^{19}F$, in particular the primary branching ratios and strengths for resonances.
In the astrophysical scenario a negligible resonance strength was found with respect to what expected by Fortune *et al.* [6], indicating a weakened impact of the low-lying resonant cross section with respect to the direct compound mechanism in the AGB energy range. For the nuclear physics side, the knowledge of the ^{19}F compound nucleus was improved, with the observation of many new transitions in known resonances decay and the study of the poorly known resonance 216 keV.

Appendix A

Table 4.10: Efficiency curve parameters (600-12000 keV)

d_0	a_0	b_0	a	b	c	k_1	k_2	k_3
6.176	0	-0.005	-2.767	1.336	-0.130	13.533	-3.527	0.193

The efficiency was parametrized [61] as:

$$\eta^{FEP}(d, E_\gamma) = f(d, E_\gamma) \cdot \exp\left(a + b\ln(E_\gamma) + c\ln\left(E_\gamma\right)^2\right) \tag{4.8}$$

$$\eta^{TOT}(d, E_\gamma) = \frac{\eta^{FEP}(d, E_\gamma)}{\exp\left(k_1 + k_2\ln(E_\gamma) + k_3\ln\left(E_\gamma\right)^2\right)} \tag{4.9}$$

$$f(d, E_\gamma) = \frac{1 - \exp(\frac{d+d_0}{a_0+b_0\sqrt{E_\gamma}})}{(d+d_0)^2} \tag{4.10}$$

Appendix B

Experimental spectra of the 151, 216, 274, 334 keV resonances, as reported in section 4.4.

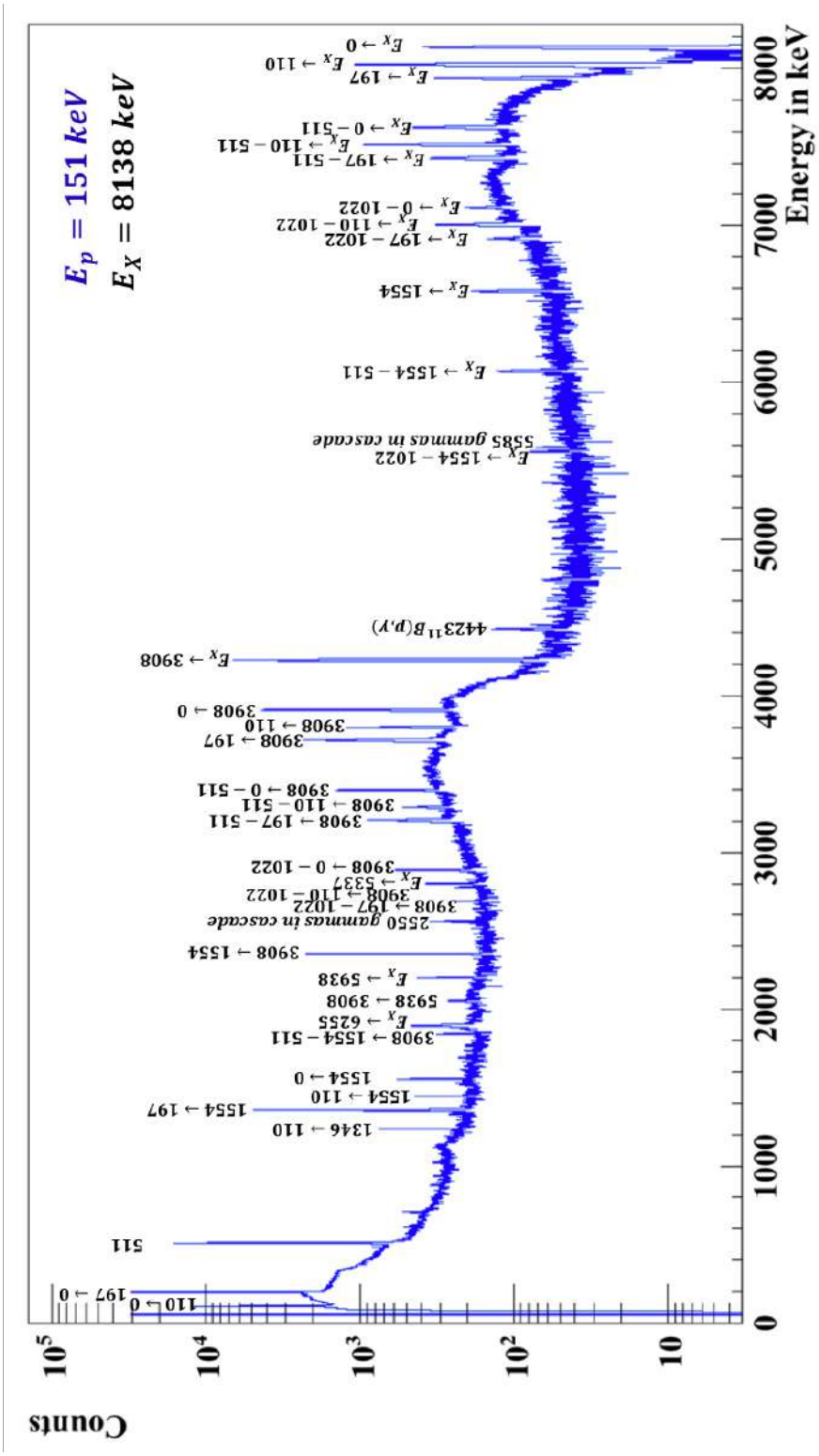

Figure 1: HPGe spectrum acquired on the 151 keV resonance, with all transitions indicated. Observed all possible primary transitions (and indicated in this plot).

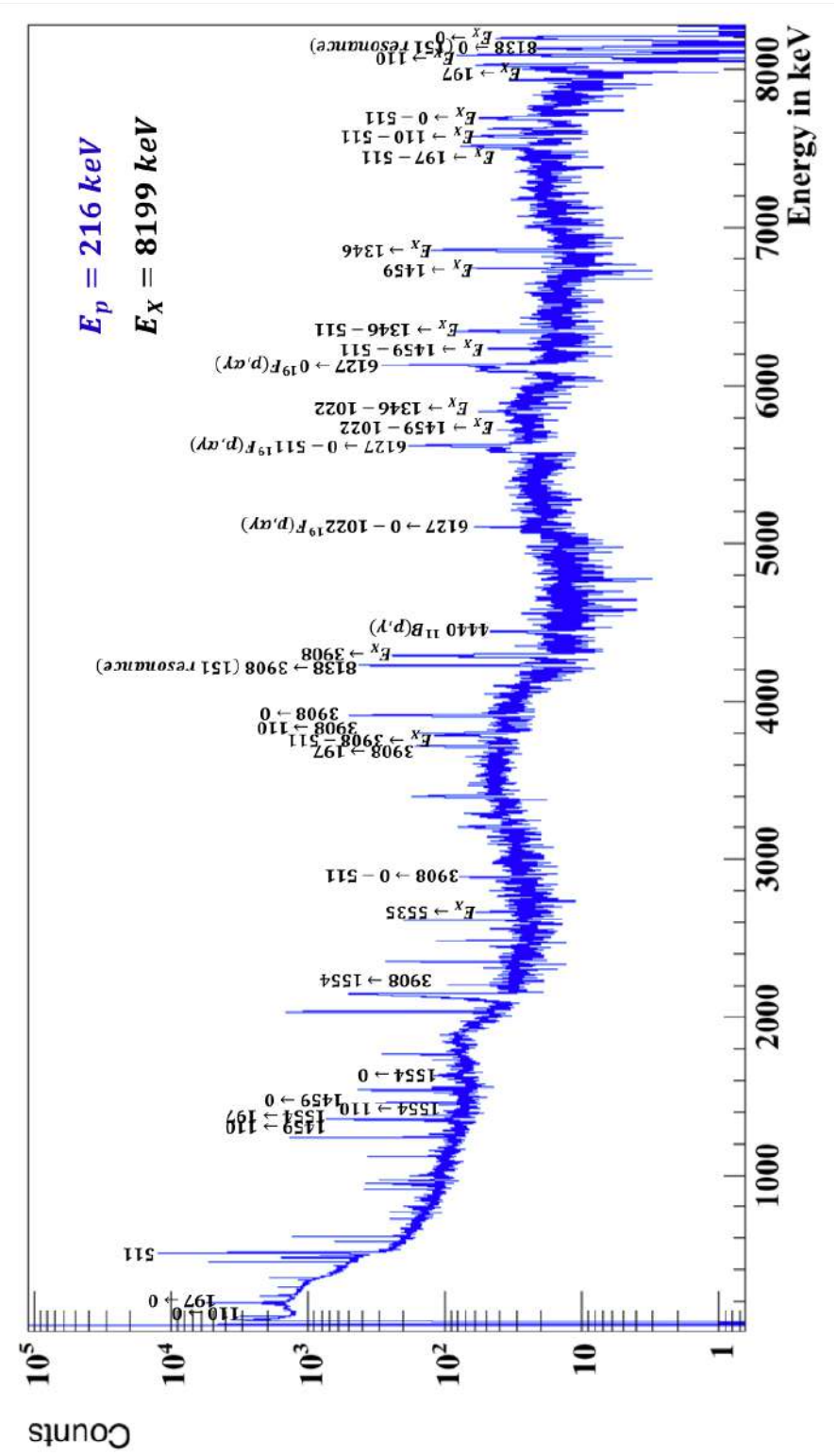

Figure 2: HPGe spectrum acquired on the 216 keV resonance, with all transitions indicated. Observed all possible primary transitions (and indicated in this plot).

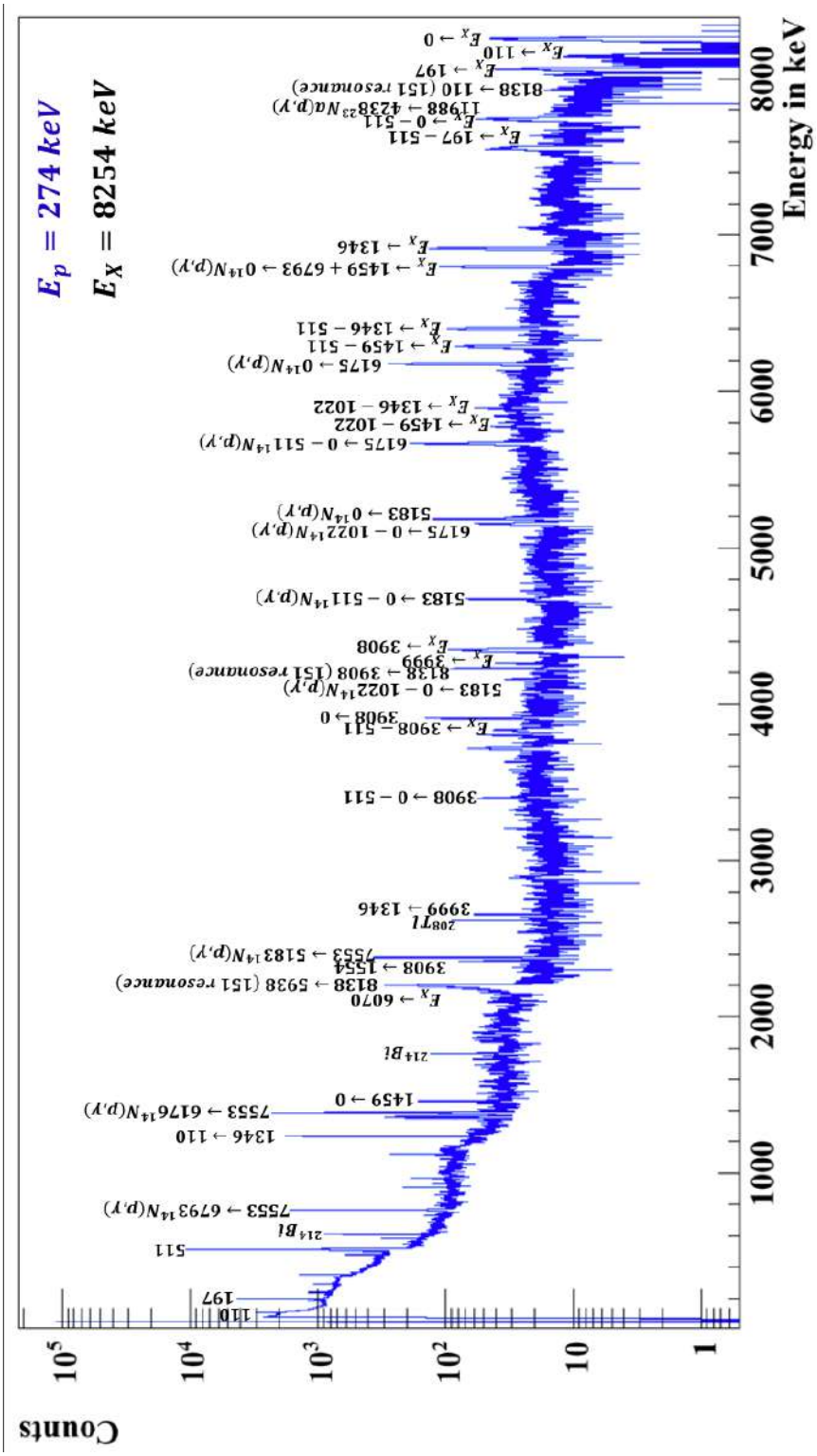

Figure 3: HPGe spectrum acquired on the 274 keV resonance, with all transitions indicated. Observed all possible primary transitions (and indicated in this plot).

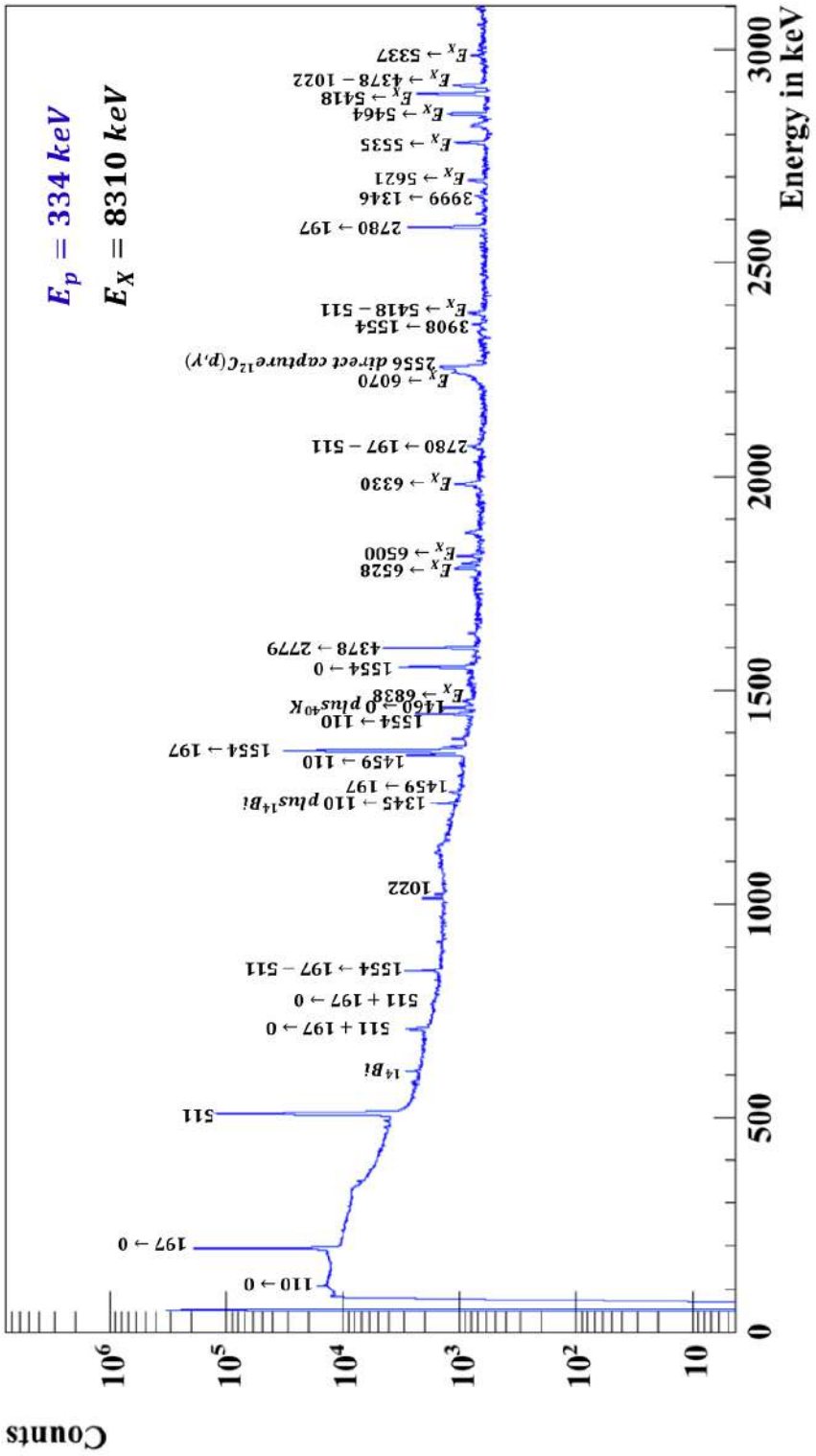

Figure 4: First zoom of HPGe spectrum acquired on the 334 keV resonance, with all transitions indicated. Observed all possible primary transitions (and indicated in this plot).

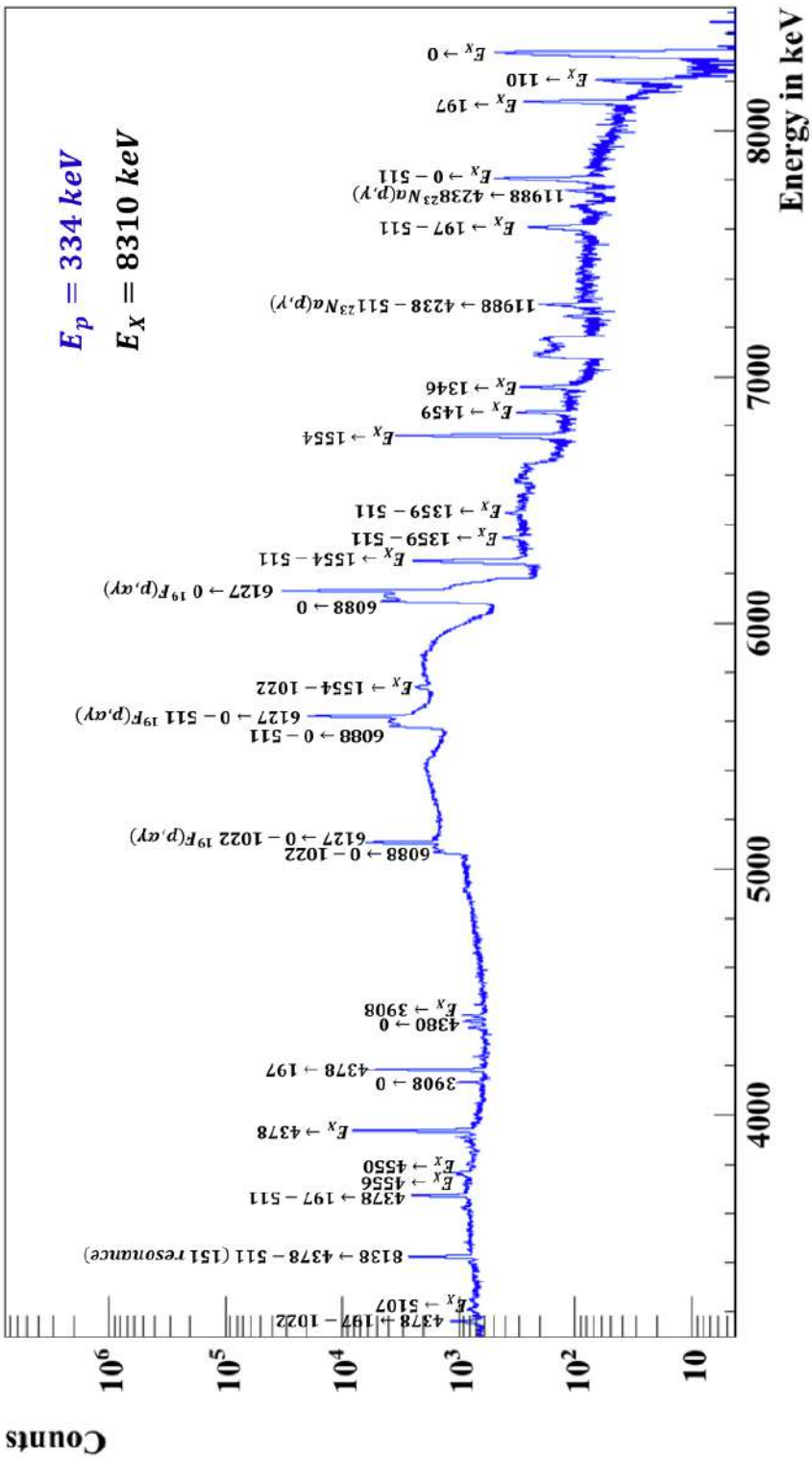

Figure 5: Second zoom of HPGe spectrum acquired on the 334 keV resonance, with all transitions indicated. Observed all possible primary transitions (and indicated in this plot).

Bibliography

[1] P. C. Scott, M. Asplund, N. Grevesse, and A. J. Sauval, Astron. Astrophys. **456**, 675 (2006). .

[2] S. Palmerini, M. La Cognata, S. Cristallo, and M. Busso. Deep Mixing in Evolved Stars. I. *The Effect of Reaction Rate Revisions from C to Al.* ApJ, 729:3, 2011. .

[3] L. R. Nittler, C. M. O. Alexander, R. Gallino, P. Hoppe, A. N. Nguyen, F. J. Stadermann, and E. K. Zinner. Aluminum-, Calcium- and Titanium-rich Oxide Stardust in Ordinary Chondrite Meteorites. ApJ, 682:1450, 2008.

[4] D. Tilley, H. Weller, C. Cheves, R. Chasteler, Nucl. Phys. A 595 (1995) 1. .

[5] M. Q. Buckner et al., Phys. Rev. C 86, 065804 (2012). .

[6] H.T. Fortune et al., Phys. Rev. C 015801 (2013). .

[7] M. Wiescher et al., Nuclear Physics A 349 (1980) 165-216.

[8] R. B. Vogelaar et al. Physical Review C 841 (2010) 753. .

[9] C. Iliadis et al, Nucl. Phys. A **841**, 323 (2010) .

[10] A. Formicola et al, Nucl. Instrum. Methods A 507, 609-616 (2003). .

[11] A. Caciolli, et al., *Preparation and characterization of isotopically enriched Ta2O5 targets for nuclear astrophysics studies* Eur. Phys. J. A (2012). .

[12] R. A. Alpher, R. Herman, and G. A. Gamow. Physical Review, 74:11981199, Nov. 1948.

[13] B. Pagel. *Nucleosynthesis and Chemical Evolution of Galaxies*, 2nd ed. Cambridge University Press, Cambridge, UK, 2009.

[14] C.Iliadis, *Nuclear Physics of Stars* (Wiley-VCH, 2007).

[15] Robert Hollow, Commonwealth Science and Industrial Research Organisation (CSIRO), Australia, adapted by Carin Cain.

[16] http://www.atnf.csiro.au/outreach/education/senior/cosmicengine/stars_hrdiagram.html.

[17] F. Herwig. *"Evolution of Asymptotic Giant Branch Stars"*. In: Annual Review of Astronomy and Astrophysics 43.1 (Sept. 2005), pp. 435-479. doi: 10.1146/annurev.astro.43.072103.150600.

[18] B. Povh et al, *Particles and Nuclei*, Springer ,Seventh edition .

[19] C. Rolfs, *Cauldrons in the Cosmos* (The University of Chicago Press, 1988).

[20] C. Bertulani, *Frontiers in Nuclear Astrophysics*. In: Progress in Particle and Nuclear Physics (April 2016).

[21] S. Ahlen et al. *"Study of penetrating cosmic ray muons and search for large scale anisotropies at the Gran Sasso Laboratory"*. In: Physics Letters B 249.1 (Oct. 1990), pp. 149-156. doi: 10.1016/0370-2693(90)90541-D. .

[22] A. Lemut, Eur. Phys J. A 36 (2008) 233. .

[23] M. Lugaro. *Stardust from meteorites: an introduction to presolar grains*, volume 9. World Scientific, 2005.

[24] P. Hoppe. *Stardust in primitive solar system materials. In Fifth European Summer School on Experimental Nuclear Astrophysics*, volume 1213, page 84, 2010. .

[25] G. J. Wasserburg, A. I. Boothroyd, and I.-J. Sackmann, Astrophys. J. Lett. 447, L37 (1995). .

[26] M. Busso, S. Palmerini, E. Maiorca, S. Cristallo, O. Straniero, C. Abia, R. Gallino, andM. La Cognata, Astrophys. J. Lett. 717, L47 (2010). .

[27] P. A. Denissenkov and C. A. Tout, Mon. Not. R. Astron. Soc. 340, 722 (2003). .

[28] J.-P. Zahn, Astron. Astrophys. 265, 115 (1992). .

[29] A. Maeder and J.-P. Zahn, Astron. Astrophys. 334, 1000 (1998). .

[30] A. V. Sweigart and J. G. Mengel, Astrophys. J. 229, 624 (1979). .

[31] F. Herwig, T. Bloecker, D. Schoenberner, and M. El Eid, Astron. Astrophys. 324, L81 (1997). .

[32] M. La Cognata et al., Astrophys. J. 708, 796 (2010). .

[33] C. Iliadis et al. Nuclear Physics A 841 (2010) 251. .

[34] U. Greife et al., NIM A 350, 327 (1994) .

[35] R. Bonetti et al., PRL 82, 5202 (1999) .

[36] C. Casella et al. *measurement of the $d(p,\gamma)^3He$ cross section down to the solar Gamow peak.* In: Nuclear Physics A 706.1-2 (July 2002), pp.203-216. doi:10.1016/S0375-9474(02)00749-2. .

[37] H. Costantini et al., PLB 482, 43 (2000) .

[38] A. Boeltzig, *Cross Section Measurements for the $^{23}Na(p,\gamma)^{24}Mg$ Reaction at LUNA.*In Journal of Physics: Conference Series 689 (Feb.216),p. 012014 DOI: 10.1088/1742-6596/689/1/012014. .

[39] D. A. Vermilyea., *The kinetics of formation and structure of anodic oxide films on tantalum, Acta Metallurgica*, VOL. 1, May 1953. .

[40] Glenn F. Knoll,*Radiation detection and measurement*, John Wiley & Sons. .

[41] A. Boeltzig and A. Best. *Hands on LUNA: Detector Simulations with Geant4.*In: Proceedings of Science Gran Sasso Summer Institute 2014 Hands-On Experimental Underground Physics at LNGS (2015). .

[42] D. Bemmerer et al. *Low energy measurement of the $^{14}N(p,)^{15}O$ total cross section at the LUNA underground facility.* In: Nuclear Physics A 779 (Nov. 2006),pp. 297-317. doi: 10.1016/j.nuclphysa.2006.09.001. .

[43] F. Strieder et al. *The $^{25}Mg(p,\gamma)^{25}Al$ reaction at low astrophysical energies.* In:Physics Letters B 707.1 (Jan. 2012), pp. 60-65. doi: 10.1016/j.physletb.2011.12.029. .

[44] C. Casella et al. *A new setup for the underground study of capture reactions.*In: Nuclear Instruments and Methods in Physics Research Section A: Accelerators,Spectrometers, Detectors and Associated Equipment 489.1-3 (Aug. 2002), pp. 160-169. doi: 10.1016/S0168-9002(02)00577-6. .

[45] V. T. Jordanov and G. F. Knoll. *"Digital synthesis of pulse shapes in real time for high resolution radiation spectroscopy".* In: Nuclear Instruments and Methods in Physics Research Section A: Accelerators, Spectrometers, Detectors and Associated Equipment. 345.2 (June 1994), pp. 337-345. doi 10.1016/0168-9002(94)91011-1. .

[46] CAEN. *Application Note AN2508: Digital Pulse Height Analyser - a digital approach to Radiation Spectroscopy. Sept. 2011.* .

[47] A. Boeltzig Thesis, *Direct Measurements of the* $^{23}Na(p,\gamma)^{24}Mg$ *Cross Section at Stellar Energies.* .

[48] A. Boeltzig et al. J. Phys G: Nucl. Part. Phys (2017) Submitted. .

[49] D. Bemmerer et al. Eur. Phys. J. A 24, 313-319 (2005). .

[50] K. Fukuda and T. Asano. *Radioisotopic Impurity of 207Bi in BGO Scintillators.* In: RADIOISOTOPES 46.3 (1997), pp. 161-164. DOI: 10.3769/radioisotopes.46.161. .

[51] D. Bemmerer. *Experimental study of the* $^{14}N(p,\gamma)^{15}O$ *reaction at energies far below the Coulomb barrier.* PhD. Berlin: Technische Universitat Berlin, Aug. 2004. .

[52] ORTEC. *Quality Assurance Data Sheet.* Dec. 2001. .

[53] A. M. T. ORTEC. *Quality Assurance Data Sheet.* July 2016. .

[54] G. Gilmore, *Practical Gamma-ray Spectrometry-2nd Edition*, 2008 John Wiley & Sons, Ltd. ISBN: 978-0-470-86196-7. .

[55] A. Best, A. Boeltzig, Private Comunications .

[56] A. Formicola et al., 2003, *A new study of t,he* $^{14}N(p,\gamma)^{15}O$ *reaction at low energy*, Nuclear Physics A719 94c-98c. .

[57] P. M. Endt, *Energy levels of A = 2144 nuclei*, Nuclear Physics A, Volume 521, 31 December 1990, Pages 1-400. .

[58] J. W. Maas, et al. *Investigation of* ^{28}Si *levels with the* (α,γ) *and* (p,γ) *reactions.*, Nuclear Physics A301 (1978) 213-236. .

[59] S. Harissopulos et al. *The* $^{27}Al(p,\gamma)^{28}Si$ *reaction: direct capture cross-section and resonance strengths at* $E_p = 0.2 - 1.12MeV$, Eur. Phys. J. A 9, 479-489 (2000). .

[60] K. Debertin, R. G. Helmer, *Gamma- and x-ray spectrometry with semiconductor detectors*, North-Holland, 1988. .

[61] G. Imbriani et al. *S-factor of* $^{14}N(p,\gamma)^{15}O$ *at astrophysical energies.* In: The European Physical Journal A 25.3 (Sept. 2005), pp. 455-466. DOI: 10.1140/epja/i2005-10138-7. .

[62] Gelsema, S. J., *Advanced g-ray Spectrometry Dealing with Coincidence and Attenuation Effects, 2001.* University of Technology Delft, Delft University Press, Delft, Ph.D.Thesis. .

[63] Blauuw, M.,Gelsema, S. J., 2003. Cascade summing in gamma-ray spectrometry in marinelli-beaker geometries: the third efficiency curve. Nucl. Instrum. Methods A505, 311-315. .

[64] https://www.pp.rhul.ac.uk/ cowan/stat/notes/efferr.pdf .

[65] A. Boeltzig, Private Comunications .

[66] C. Fox, C. Iliadis, A. E. Champagne, R. P. Fitzgerald, R. Longland, J. Newton, J. Pollanen, and R. Runkle, Phys. Rev. C 71, 055801 (2005). .

[67] J. F. Ziegler and J. P. Biersack. SRIM 2013. http://srim.org/, accessed: October 3, 2016.

[68] H. Andersen and J. F. Ziegler, The Stopping and Ranges of Ions in Matter (Pergamon, New York, 1977). .

[69] J. F.Ziegler, Nucl. Instrum. Methods B 219, 1027 (2004). .

[70] SRIM (updated version 2008) http://www.srim.org (accessed 6 March 2012). .

[71] Gerald van Belle, Lloyd Fisher, Patrick J. Heagerty, Thomas Lumley, Biostatistics: *A Methodology for the Health Sciences* (2nd Edition). .

[72] http://faculty.washington.edu/heagerty/Books/Biostatistics/TABLES/Poisson/index.html. .

[73] http://statpages.org/confint.html .

[74] F. Garwood, *Fiducial Limits for Poisson Distribution, Biometrica* 28:437-442, 1936. .

[75] F. Ajzenberg-Selove. *Energy levels of light nuclei A = 11-12".* In: Nuclear Physics A 506.1 (Jan. 1990), pp 1-158. DOI:10.1016/0375-9474(92)90236-D. .

[76] S. Croft. *The absolute yield, angular distribution and resonance widths of the 6.13, 6.92 and 7.12MeV photons from the 340.5 keV resonance of the* $^{19}F(p,\alpha,\gamma)^{16}O$ *reaction*. In: Nuclear Instruments and Methods in Physics Research Section A: Accelerators, Spectrometers, Detectors and Associated Equipment 307.2-3 (Oct. 1991), pp. 353-358. doi: 10.1016/0168-9002(91)90204-4. .

[77] K. Spyrou et al. *Cross section and resonance strength measurements of* $^{19}F(p,\alpha,\gamma)^{16}O$ *at* E_p *= 200-800 keV*, Eur. Phys. J. A 7, 79-85 (2000). .

[78] https://www.nndc.bnl.gov/ .

[79] W. Wang, et al., Chin. Phys. C 36 (2012) 1603. .

[80] J. R. Dermigny et al. *γ-Ray spectroscopy using a binned like lihood approach*, Nuclear Instruments and Methods in Physics Research A 830(2016)427437 .

[81] S. Wilmes et al., *The* $^{15}N(\alpha,\gamma)^{19F}$ *reaction and nucleosynthesis of* ^{19}F, Phys. Rev. C 66, 065802 (2002). .

[82] C. D. Nesaraja et al., *Nuclear structure properties of astrophysical importance for* ^{19}Ne *above the proton threshold energy*, Phys. Rev. C **75**, 055809 (2002). .

[83] A. Di Leva et al., *Measurement of 1323 and 1487 keV resonances in* $^{15}N(\alpha,\gamma)^{19F}$ *with the recoil separator ERNA*, Phys. Rev. C **95**, 045803 (2017). .